Modulating the Structure of Plant-Based Protein Dispersions

Kurnia Ramadhan

A thesis submitted in fulfilment of the requirements for the degree of

Doctor of Philosophy in Food Science

University of Nottingham

School of Biosciences

2019

Abstract

The aim of the work presented in this thesis is to understand the formation of protein solidified gel network with controlled structures prepared from commercially established plant-based protein materials. Different types of soy protein isolates were characterised at various structural length scale. At molecular scale, results obtained from gel electrophoresis, scanning calorimetry, and infrared spectroscopy showed that variations in polypeptide constituents and protein conformations led to a different protein solubility in water. At mesoscopic length scale, soy protein isolates insoluble fraction was characterised as protein particles with diverse range of shapes and size distributions. At macroscale, viscoelastic behaviour of protein particles with the largest mean diameter size required the lowest isolate concentration due to their high dispersed phase volume.

Heat-induced protein gel was prepared from soy protein isolate with limited solubility. The presence of either calcium chloride or microbial transglutaminase enzyme is required to achieve a solidified structure. The addition of calcium chloride altered protein spatial structure leading to formation of denser gel matrices. In contrast, the presence of microbial transglutaminase enzyme increased the dynamic moduli without losing the water retaining ability of initial spatial structure as favoured by newly formed covalent linkages.

The usability of low purity protein material derived from oat bran was also investigated. Structural properties of oat bran protein-rich material indicated the aggregated protein conformation and the presence of carbohydrate and

lipid in complex form. Ball milling treatment not only reduced the particle size of protein material, but also altered the conformation of the chemical constituents. A high solid concentration, i.e. 30%, is required to achieve a stable oat bran protein dispersion. Dynamic moduli of dispersion increased as a result of heat-induced structure formation.

Mechanical properties of protein gels containing mixtures of soy protein isolate and oat bran protein-rich material were evaluated. Gel structure was mainly built from soy protein, whereas oat bran protein was used as filler particles. Increasing filler concentrations to the gel matrix led to a more stiff and brittle protein gel structure. Addition of filler particles at higher concentration to the enzymatically crosslinked gel matrix increased both stiffness and elasticity of the gel structure. The provided insight from this work will be beneficial to the development of plant-based novel protein-rich foods.

Acknowledgments

I would like to express my gratitude to my supervisor, Professor Tim Foster, for his valuable advices, insights, and support throughout my PhD journey.

I would also like to acknowledge the full financial support from the Ministry of Research, Technology, and Higher Education of the Republic of Indonesia to complete the PhD studies.

I am very grateful to all academics and colleagues within the Food Structure research group, and the Division of Food Sciences in general for their cooperation upon completion of this research work.

Lastly, I dedicate this thesis to my family, especially my beloved wife and my parents.

Table of Contents

List of Figures

List of Tables

List of Publications

Published articles:

- Ramadhan, K., & Foster, T. J. (2018). Effects of ball milling on the structural, thermal, and rheological properties of oat bran protein flour. Journal of Food Engineering, 229, 50-56.

Manuscript submitted to European Food Research and Technology:

- Understanding structural differences of soy protein isolate dispersions at multiple length scales that contribute to viscoelastic behaviour

Manuscript under preparation:

- Modulating the structure of gels containing protein mixtures of soy and oat bran

Conference presentations:

- The 2nd Congress on Food Structure Design, 26th – 28th October 2016, Antalya, Turkey: Effects of Ball Milling on the Selected Properties of High Protein Oat Bran Powder and Slurry (oral presentation)
- The 19th Gums and Stabilisers for the Food Industry Conference, 27th – 30th June 2017, Berlin, Germany: Effects of Oat Bran Protein Particles on the Rheological Properties of Soy Protein Gel (poster presentation)
- The 17th Food Colloids Conference, 8th – 11th April 2018, University of Leeds: Rheological properties of particle-filled transglutaminase-induced soy protein isolate gels (poster presentation)

Glossary of Abbreviations

Abbreviation	Definition
APDO	Alkaline-washed polar solvent-defatted OBP
ATR-FTIR	Attenuated total reflectance Fourier transform infrared spectroscopy
ESEM	Environmental scanning electron microscopy
HSST	High speed short time ball milling
Lab SPI	Laboratory-prepared SPI sample
LSLT	Low speed long time ball milling
Micro-DSC	Micro-differential scanning calorimetry
MTGase	Microbial transglutaminase
NPDO	Non-polar solvent-defatted OBP
OBP	Oat bran protein concentrate
PDO	Polar solvent-defatted OBP
SDS-PAGE	Sodium dodecyl sulfate polyacrylamide gel electrophoresis
SPI	Soy protein isolate

1 General Introduction

1.1 Research background

Food protein is a vital part of human diet that plays important role in maintaining body functions. Proteins are available from various plant and animal sources. Increasing global human population will face a challenge in securing food protein needs. Food production from animal origin is considered less efficient in fulfilling the needs of growing population and adversely affects the environment, whereas plant-based protein gains positive reputation as a more sustainable source (Day, 2013; Nadathur et al., 2016; Raphaely and Marinova, 2014). In response to this issue, there has been a growing research interest in finding alternative sustainable protein sources harvested from various plants and agricultural side-products (Don, 2017; Fabian and Ju, 2011; Moure et al., 2006; Pihlanto et al., 2017; Schutyser and van der Goot, 2011; Sozer et al., 2017; Wanasundara, 2011).

The idea to increase plant-based protein consumption has been promoted to secure a more sustainable protein supply (Aiking, 2011; Day, 2013; Hartmann and Siegrist, 2017). Among the promising method to increase plant-based protein intake is by partial or full replacement of animal protein in foods and development of innovative plant-based protein foods with high consumer acceptance (Brückner-Gühmann et al., 2019; Grabowska et al., 2014). One of the key factors affecting consumer acceptance is textural attributes. Since textural perception is strongly related to food structure, appropriate design and modification on food structure is essential.

One consideration in designing plant-based protein foods is there are some drawbacks on nutritional quality of plant-based proteins due to the fact that they lack some of essential amino acids, compared to animal-based proteins, affecting their nutritional quality; specifically leucine, lysine, and/or methionine. Consumption of combined plant proteins from different sources has been suggested to provide a better balance of amino acids profile (Gorissen et al., 2018). From the food structure perspective, mixed protein system will result in a different structural formation (Krintiras et al., 2015). Accordingly, study on the structure of mixed plant protein system could be a great importance toward an increased plant protein consumption.

Protein-rich foods have become essential part of healthy lifestyle due to its benefits in maintaining skeletal mass and function, and body weight control. The former benefit is related to the nutritional value of amino acids, whereas the latter is favoured by satiety effect of dietary protein (Campbell et al., 2017; Deutz et al., 2014; Westerterp-Plantenga et al., 2017). Furthermore, foods in solid form provide stronger satiety effects than liquid foods (Chambers et al., 2015). Based on this context, development of solid protein-rich foods is more relevant to the innovation of plant-based protein foods.

Protein acts as the predominant building block in creating the structure of protein-rich foods. The ability of proteins to aggregate and to form elastic gel network is a great importance in creating desirable texture. Protein gelation properties are affected by various factors that generally categorised into intrinsic and extrinsic factors. The former consists of protein molecular weight, hydrophobicity, electrostatic interactions, and amino acid compositions, whereas the latter includes pH, temperature, ionic strength,

and pressure (Totosaus et al., 2002). A more comprehensive approach recently proposed by Foegeding (2015) defining protein functionality, including gelation ability, based on the critical structural scale, namely molecular scale, mesoscale, and macroscale. This approach provides a better understanding in designing the structure of protein-rich foods.

Research on protein-rich foods require a proper selection of materials used in the study. Commercial protein products, such as soy protein isolates, are readily available and convenient to use for development of plant-based protein foods. It is important to note that food proteins are prone to irreversible structural changes that commonly occurred in the manufacturing of commercial protein products. Therefore, appropriate characterisation is essential to avoid misunderstanding on material properties and further structural modification.

1.2 Objectives

The main objective of the work presented in this thesis is to understand the formation of protein solidified gel network with controlled structures prepared from commercially established plant-based protein materials, in which will be beneficial for the development of plant-based solid protein-rich foods. Based on this objective, the experimental works reported in this thesis were aiming: (1) to study the effects of structural differences at various length scales on the rheological properties of protein dispersions; (2) to investigate the effects of salt and protein crosslinking enzyme upon heat-induced structure formation of protein gel; (3) to evaluate the effects of physical modification by

milling on structural and physicochemical properties of low purity protein concentrate; (4) to elaborate the structure of protein gel prepared from mixture of plant proteins with different degree of purity. This study offers new insight that is important in development of plant-based high protein foods.

1.3 Outline of Thesis

This thesis consists of eight chapters, including four chapters of experimental work. The first chapter provides a brief explanation on research background and objectives of this thesis. Summary of the existing studies and previous literatures related to plant-based food proteins and food structure are written in the second chapter. The third chapter compiles description of all the main materials and methods that is used in various experimental works. In chapter 4, characterisation of various commercially available soy protein isolates was conducted to reveal difference in structural properties. Chapter 5 demonstrates the use of protein with limited solubility in creating solidified gel structure. Chapter 6 elaborates the potential use of low purity protein materials derived from oat bran for the application of solid protein-rich foods. In chapter 7, gels containing mixtures of plant proteins were evaluated by means of dynamic rheology. At last, the conclusions and future work are presented in chapter 8.

2 Literature Review

2.1 Food proteins from plants

Many edible plants have been utilised as sources of dietary protein providing moderate to high amounts of protein relative to other macronutrients, i.e. lipid and carbohydrate (Belitz et al., 2009a, 2009b; Orona-Tamayo and Paredes-López, 2017; Scanlin and Lewis, 2017). Table 2.1 shows the average protein, lipid, and carbohydrate contents of several major food crops that can be classified into legumes, cereals, and pseudo-cereals. Legumes generally exhibit higher protein content than other crops that can be attributed to the capability of leguminous plants in nitrogen fixation (Maphosa and Jideani, 2017). Soybean and peanut are among the most important leguminous crops that contain very high amount of protein and lipid. Global production of soybean reaches more than 300 million tonnes annually, whereas peanut production is estimated to exceed 40 million tonnes (United States Department of Agriculture, 2019). Both crops are also popular as oilseeds due to large amount of extractable oils. Soybean oil extraction process produces soymeal as side product which can be processed into various high protein ingredients (Singh et al., 2008). Similarly, the protein-rich peanut flour can be obtained from the side product of peanut oil extraction (Sandefur et al., 2016). Alternative legumes such as lentils, peas, garden beans, and chickpeas are generally rich in carbohydrate and protein, and very low in lipid. The crops are either processed into flour or retained as seed used for various food applications (Boye et al., 2010). However, the annual worldwide

production of these crops is far lower than soybean and peanuts (Food and Agriculture Organization of the United Nations, 2019).

Cereals are known as a primary source of carbohydrate and mainly consumed as staple foods. Although cereals show lower protein content than legumes, cereals are produced and consumed in large quantities, i.e. as staple food, providing significant contribution to fulfil the protein needs. As shown in Table 2.1, oat exhibits the highest protein content among the cereals, i.e. 14.8%, followed by wheat, corn, and rice. Global production of cereals ranks the top among other food crops. Total production of corn exceeds 1 billion tonnes annually, whereas wheat and rice production reaches 700 million tonnes. However, oat production is far smaller than other cereals at about 20 million tonnes per annum (Food and Agriculture Organization of the United Nations, 2019). The amount of cereal protein tends to decrease after undergoing processing due to removal of protein-rich cereal bran fraction. The underutilised bran fraction have been considered as potential alternative protein sources (Sozer et al., 2017).

Some other crops are utilised as cereal-substitutes despite having taxonomical differences, hence called as pseudo-cereals. Amaranth (*Amaranthus spp.*) and quinoa (*Chenopodium spp.*) are the examples of high protein pseudo-cereals with slightly lower carbohydrate content. The crops are commonly utilised as alternative gluten-free ingredients in many food products. Amaranth and quinoa are gaining popularity as novel protein sources that may provide viable options for the future, in the requirement to feed growing global population. However, their low quantity in current

production may limit a wider utilisation of these crops (Food and Agriculture Organization of the United Nations, 2019; Janssen et al., 2017).

Table 2.1 Comparison on the average protein, lipid, and carbohydrate contents of several food crops calculated on dry basis.

Classification	Food crops	Protein (%)	Lipid (%)	Carbohydrate (%)
Legumes	Soybean	41.0	19.6	7.6
	Peanut	31.4	50.7	7.9
	Lentils	28.6	1.6	57.6
	Peas	25.7	1.4	53.7
	Garden beans	24.1	1.8	54.1
	Chickpeas	22.7	5.0	54.6
Cereals	Wheat	13.5	2.5	68.7
	Rice	8.6	2.8	86.1
	Corn	10.6	4.4	73.9
	Oat	14.8	8.3	65.5
Pseudo-cereals	Amaranth	17.9	7.7	57.0
	Quinoa	16.0	7.0	66.0

References: Belitz et al. (2009a, 2009b); Orona-Tamayo and Paredes-López (2017); Scanlin and Lewis (2017).

Nutritional quality of dietary protein is often determined by essential amino acid profiles. Plant-based proteins generally provide sub-optimal balances on essential amino acid compared to animal-based proteins. Cereals are lacking in lysine, cysteine, methionine, and tryptophan, whereas legumes and pseudo-cereals exhibit higher levels of lysine. Therefore, blending of different plant protein sources are commonly suggested for daily consumption to fulfil a well-balanced essential amino acids (Day, 2013; Scanlin and Lewis, 2017).

2.2 Protein concentrates and isolates

Protein-rich food crops can be processed into protein-rich materials, i.e. concentrates and isolates, through various separation processes. Protein-rich materials are versatile food ingredients providing both nutritional benefits and technical functionalities for various food applications. The ingredients are nutritionally beneficial by increasing the protein content of final food products with a well-balanced amino acid profile (Singh et al., 2008). High intake of dietary protein helps to maintain the skeletal muscle mass and function, and induces the satiety effects (Westerterp-Plantenga et al., 2017). Technical functionalities provided by protein-rich materials include their ability to enhance stability, structure and texture of foods (Foegeding, 2015).

Among the protein-rich food crops, soybean is the most widely processed into protein-rich materials and used for food application. Hulls are firstly removed, and soybeans are crushed into flakes. Subsequently, soy flakes undergo oil extraction using food grade solvents, typically hexane, resulting

in soybean oil and defatted soybean flakes. The defatted flakes contain about 50% protein and can be milled into different particle sizes to obtain soy flour or grits. Removal of soluble carbohydrates from defatted flakes are required to obtain soy protein concentrate. The flakes are washed in acidic conditions resulting in protein precipitation and carbohydrate solubilisation. The carbohydrates are then discarded hence the protein content increases to about 65% on a dry basis. A highly purified protein ingredient derived from defatted soybean flakes is called soy protein isolate containing about 90% protein. Defatted flakes are washed in alkaline conditions to solubilise the protein and separate from fibre-rich insoluble fractions. The solubilised protein is then precipitated at isoelectric point around pH 4.5. The precipitated curd is subsequently washed to remove non-protein components, neutralised, and spray dried into powder form (Preece et al., 2017; Thrane et al., 2017).

Similar wet extraction techniques are also used to produce protein concentrates and isolates from different sources (Boye et al., 2010; Wu et al., 2009). However, protein extraction from some plant materials require process modification due to their morphological differences, such as in cereal bran. Extraction of oat bran protein is challenging due to its thick cell walls and the thickening effects of soluble fibres. Conventional wet extraction from oat bran in alkaline condition requires higher pH that adversely affect nutritional quality of the extracted protein by facilitating the formation of toxic compound known as lysinoalanine. Enzymatic pre-treatment of oat bran using carbohydrase enzyme is reported to be effective in assisting protein extraction by degrading and loosening the cell wall structures. The enzyme-

assisted protein extraction is applicable to obtain either protein concentrates or isolates (Guan and Yao, 2008; Jodayree et al., 2012; Liu et al., 2008).

Wet extraction techniques are effective methods to obtain highly purified protein products, i.e. protein isolates. However, this technique is inefficient due to large consumption of water and energy. Dry fractionation has been introduced as an alternative method to wet extraction in producing plant-based protein-rich materials, particularly for pulses and cereals. Protein products obtained from dry fractionation exhibits lower degrees of purity, i.e. protein concentrate, and retained functionality of native protein structure. Therefore, increasing utilisation of protein concentrates in food application is considered as more relevant to enable a more sustainable direction (Pelgrom et al., 2013; Schutyser and van der Goot, 2011).

2.3 Protein contribution to food structure

Protein is the important structural building block in protein-rich foods favoured by the ability to form physical networks. During food processing, proteins undergo structural alterations particularly due to thermal processing. When proteins are heated above their denaturation temperature, the native structure typically unfolds leading to exposure of hydrophobic groups which is followed by protein aggregation. In aqueous systems, rearrangement of aggregated protein turns the low viscosity protein dispersion into high viscosity protein gel. Protein gel networks are achieved when the protein concentration is above its critical gelling concentration (Nishinari et al., 2014).

Denaturation temperature and aggregation behaviour of different proteins are varied. Glycinin and β-conglycinin, for example, are the major protein constituents of soybean which belong to the 11S and 7S globulin proteins, respectively. This classification of globulins refers to the protein sedimentation coefficient that reflects their respective molecular weight. The former protein is fully denatured at higher temperature than the latter, as favoured by a more thermally stable disulphide linkages and its hexameric protein structure. Varying the ratio between glycinin and β-conglycinin will result in different characteristics of soy protein gels (Guo et al., 2012; Nishinari et al., 2014; Renkema et al., 2001).

Protein gels from globular proteins, such as those found in many plants, share a characteristic of a ‘particle gel’ due to interactions of interconnected particles that contribute to viscoelasticity and creating the gel matrix (Berghout et al., 2015). Particle gels are constituted of interconnected particles, stabilised by different chemical and physical interactions, such as disulphide and hydrogen bonds, and electrostatic and hydrophobic interactions. Characteristics of protein particle gels can be modulated by varying pH, ionic strength, and addition of different type of salts. The modulated characteristics at mesoscopic scale, such as size distribution and surface properties, have been of interest in novel food product development (Grygorczyk and Corredig, 2013; Renkema, 2004; Sağlam et al., 2013; Urbonaite et al., 2014).

Novel protein-rich food structure can also be achieved by using combination of plant proteins. Mixtures of different plant proteins may contribute differently to the physical structure. Recent studies of soy protein-wheat

gluten blends showed compatibility of the mixture in forming meat-like fibrous structures (Grabowska et al., 2014; Krintiras et al., 2015).

3 Materials and Methods

3.1 Materials

3.1.1 Soy protein isolates

Different commercial soy protein isolates (SPI) with minimum 90% (dry weight) protein content were obtained from Solae Belgium N.V (Ieper). These commercial products were originally manufactured for different purposes of application. The SUPRO® 548 IP was for the application in meat products, whereas the SUPRO® 670 IP and SUPRO® 760 IP were for the application in emulsions with low and high viscosity, respectively.

The laboratory-prepared SPI was extracted from whole soybean flour (Fudco, London). The product was purchased from a local distributor. Each 100 g of product was labelled to contain 38.3 g protein, 23.5 g carbohydrate, and 18.8 g fat.

3.1.2 Oat bran protein concentrate

Oat bran protein concentrate (OBP) was supplied by Tate & Lyle Oat Ingredients (Kimstad, Sweden) as a brand of PrOatein®. The flour was declared to have ca. 94% dry matter containing 54% protein, 17% fat, 18% carbohydrate, and 2% fibre on a dry basis. This material was prepared from oat bran that has gone through enzymatic, thermal, and physical separation processes (personal communication with the manufacturer).

3.1.3 Chemicals

All chemicals used in the experiment were analytical grade and purchased from various suppliers, such as calcium chloride, hydrochloric acid, sodium hydroxide, hexane, and deuterium oxide.

3.1.4 Enzymes

Microbial tranglutaminase enzyme (Activa® WM) was kindly donated by Ajinomoto Foods Europe SAS (France). The enzyme preparation was in a form of powder that has been diluted in maltodextrin. The enzyme activity was 100 U in each gram of powder.

3.2 Methods of analysis

3.2.1 Sodium dodecyl sulfate polyacrylamide gel electrophoresis (SDS-PAGE)

SDS PAGE was performed to compare the constituting protein of samples according to the procedure described by Bio-Rad (2011). Sample dispersions of 0.2% (w/w) concentration were mixed with Laemli sample buffer (Sigma-Aldrich Co, MO, USA), at ratio 1:1 then boiled for 5 min and cooled back to ambient temperature. A precast 4–15% polyacrylamide gel (Bio-Rad Laboratories, CA, USA) was used and placed into Mini Trans-Blot® Cell (Bio-rad Laboratories Srl, Milan, Italy) filled with Tris Glycine SDS running buffer (Thermoscientific, IL, USA). Precision Plus Protein™ Standards All Blue (Bio-Rad Laboratories, CA, USA) was used as protein standard marker. An aliquot of 5 µl of samples and protein marker were

pipetted into the gel and run at 100 V for 60 min. The gel was stained with a solution containing Coomassie Brilliant Blue R-250 Dye (Fisher Scientific UK, Loughborough, UK) for 1 h and subsequently destained for 3 h. Electrophoresis was repeated three times to obtain consistent results. A gel image was captured using a Bio-Rad Gel Doc XR System. Identification of protein bands were allocated with reference to Sirison et al. (2017).

3.2.2 Micro-differential scanning calorimetry (Micro-DSC)

Thermal properties of sample dispersions were evaluated in a Micro-Differential Scanning Calorimeter III (Setaram Instrumentation, France). About 800 mg of dispersions was transferred into hermetically sealed sample vial made from hastelloy, while similar weight of deionized water was used as reference. Heating-cooling processes were performed in two cycles from 20 to 120 ^{o}C at a rate of 1 ^{o}C min^{-1}. Each measurement was run in duplicate.

3.2.3 Attenuated total reflectance – Fourier transform infrared (ATR-FTIR) spectroscopy

The procedure on conducting ATR-FTIR spectroscopy measurement was taken from Ottenhof et al. (2003). The FTIR spectra acquisition was conducted using a Bruker Tensor 27 System (Bruker Optik GmbH, Ettlingen, Germany) equipped with diamond crystal as ATR material and temperature controller (Graseby Specac Ltd., UK) and run on OPUS software version 7.2.139.1294. An open-air background test was run prior to the measurement of powder samples. Subsequently, a few mg of powder

sample was placed into contact with the diamond ATR crystal and sample holder. All sample measurements were run under 128 scans with 4 cm^{-1} resolutions. For the measurement of dispersion samples, deuterium oxide (D_2O) was used as continuous phase of dispersion samples instead of water, to avoid band overlapping between protein and water. A single pipette drop of D_2O was run as background. A few drops of SPI dispersions were applied directly onto the diamond ATR crystal and sealed with a rubber gasket. Each measurement was run in duplicate.

The acquired spectra were further processed, i.e. normalisation, baseline correction, derivatisation, and integration using Spectragryph optical spectroscopy software version 1.0.2 (https://www.effemm2.de/spectragryph/). Second derivative spectra were used to predict relative abundance of protein secondary structure, by taking the ratio of integration of each structure-assigned band to total corresponding secondary structures. Band assignment on protein conformation referred to a work by Bock and Damodaran with some modifications (2013), i.e. β-sheets at ~1600-1640 cm^{-1}, β-turns at ~1660-1690 cm^{-1}, and combination of α-helix and random coil structures, due to overlapping of both structure-assigned bands at ~1640-1660 cm^{-1}.

3.2.4 Measurement of protein solubility

Sample dispersions at a concentration of 0.1% (w/w) were used for soluble protein measurements. The dispersions were transferred to 2 ml microtubes, then subsequently centrifuged at 10000 g and 5 ^{o}C for 15 min. The

supernatant was then collected and filtered through a 0.45 µm nylon syringe filter. The filtered supernatant was used for protein measurement using bicinchoninic acid protein assay (Pierce Biotechnology, Rockford, Illinois, USA) as described in the protocol provided by Thermo Scientific (2011). Protein solubility was calculated from the amount of soluble protein within the supernatant and expressed in g per 100 g sample. Bovine serum albumin was used as standard. Each measurement was run in duplicate.

3.2.5 Light microscopy

Sample dispersions were visualised using an EVOS f1 microscope (AMG, Washington, USA) based on a method described by Kasprzak et al. (2018). An aliquot of 0.1% (w/w) sample dispersion was dropped onto the well of microscope slide (Marienfeld, Lauda-Königshofen, Germany) onto which the cover slip was carefully placed. Micrograph images were acquired using transmitted light at the magnification of 40x.

3.2.6 Environmental scanning electron microscopy

SPI gels were analysed using an Environmental Scanning Electron Microscopy unit of FEI Quanta 650 ESEM microscope at The Nanoscale and Microscale Research Centre (nmRC) facility. The gels were cut into slices about 2 mm thickness and carefully placed onto the sample holder without any sample preparations. The images were captured at a working distance of about 7.5 mm with acceleration voltage of 10 kV based on the working procedure set by nmRC. Sample dehydration was performed *in situ* by

adjusting humidity, temperature, and air pressure of the sample chamber accordingly throughout the observation to obtain clear images.

3.2.7 Particle size distribution

Sample dispersions at the concentration of 1% (w/w) were used to measure particle size distribution. The dispersions were kept stirred prior to measurement to prevent sedimentation. The measurement was based on the principles of light scattering using LS13320 Laser Diffraction Particle Size Analyzer (Beckman Coulter, High Wycombe, UK) as described by Dubey and Windhab (2013) with modifications. The measurement was run for 60 s. Fraunhofer theory was used as optical model treating particles as a spherical approximation. The value of dispersant (water) refractive index was set to 1.33. Each measurement was run in duplicate.

3.2.8 Dispersion stability by multiple light scattering

Sedimentation of sample dispersions were evaluated by using Turbiscan LAB (Formulaction, L'Union, France) as described by Celia et al. (2009) with modifications. This instrument works by measuring both light transmission and backscattering with respect to the sample incident radiation at an angle of 180^{o} and 45^{o}, respectively. The 880 nm pulsed near-infrared light was used as the source of photon. Sample dispersions were transferred into a ~40 mm height flat bottom cylinder glass vial. The vial was placed into the measuring chamber and the temperature was set to approximately 25 ^{o}C.

Light backscattering intensity was recorded across the height of vial. Each measurement was run in duplicate.

3.2.9 Measurement of dispersed phase volume

Dispersed phase volume of sample dispersions at concentration at various concentrations were measured in a centrifuge tube following the work described by Amani et al. (2004) with some modifications. Sample dispersions were centrifuged at 1500 g for 5 min. Phase volumes were calculated by dividing volume of sediment by total volume of dispersion. Each measurement was run in duplicate. Linear regression was used to obtain projected phase volume at higher concentration.

3.2.10 Rheology

Viscosity of sample dispersions at various concentration were measured on a rheometer (Physica MCR 301, Anton Paar, Austria) using concentric cylinder (CC27) geometry. The applied rotational shear rate was ramped-up from 0.1 to 100 s^{-1}. To compare concentration dependence of viscosity, the data are plotted as specific viscosity (η_{sp}) that given by:

$$\eta_{sp} = (\eta - \eta_s)/\eta_s \qquad \text{(Equation 3.1)}$$

where η is viscosity of dispersion at Newtonian plateau and η_s is viscosity of solvent (i.e. water). Where Newtonian plateau is not apparent, the smallest measurable viscosity data points at low shear was used as described by Shewan (Shewan, 2015).

Viscoelastic behaviour of sample dispersions was measured using the same apparatus. The serrated parallel plate (PP50/P2) was used as measuring system at 1 mm gap. To obtain a correct measurement of stable dispersions, a fixed dispersed phase volume was used instead of concentration. The amplitude strain sweep tests were conducted at a fixed angular frequency of 10 rad s^{-1}. The angular frequency sweep tests were performed at a constant amplitude strain of 0.1%. The temperature sweep tests were run at a constant angular frequency of 10 rad s^{-1} and an amplitude strain of 0.1% with various heating and cooling rates. Evaporation and large temperature gradients were prevented by using low-viscosity mineral oil and a peltier-controlled hood. Each test was run in duplicate.

4 Understanding the differences in structural and rheological properties of commercial soy protein isolate dispersions

4.1 Introduction

Soy protein isolate (SPI) is a highly purified soybean protein ingredient containing about 90% of protein. It has been introduced into foods over the past century providing advantages on nutritional and functional properties. A wide range of SPI are commercially manufactured with tailored functionalities to fulfil various food applications. Commercial SPI tends to lose their native conformation at molecular level due to harsh processing conditions that leads to them displaying limited solubility when suspended in water, and form protein particle dispersion rather than protein solution (Keerati-u-rai et al., 2011; Singh et al., 2008). Therefore, it is important to encompass evaluation on structural properties in understanding protein functionalities. The structural properties are not limited to molecular level, but also include the larger length scales, namely mesoscopic, and macroscopic scales (Foegeding, 2015).

Among the greatest importance of soy protein functional properties is the ability to form viscoelastic gel network. Soy protein gel can be achieved by various means of gelation process as similar to other globular proteins, which generally require unfolding of native protein structure to expose hydrophobic groups followed by different routes of protein aggregation (Nishinari et al., 2014). Soy protein gels are reported to have shared characteristics of

particle gel (Berghout et al., 2015). Similarly, gel formation from particle dispersions can be achieved by increasing inter-particle interactions through particle jamming (Van Der Sman, 2012). The elastic network of particle dispersion is predominantly governed by mesoscopic structure rather than direct effect of the molecular nature (van Riemsdijk et al., 2010).

Having limited solubility, mechanical properties of commercial SPI dispersions are mainly determined by physical characteristics of the insoluble fraction (Añón et al., 2001). Increasing SPI concentration leads to a viscoelastic gel behaviour due to particle jamming, yet the minimum concentration required for this varied from source to source (Ahmed et al., 2006; Berghout et al., 2015; Tang et al., 2009). Particle jamming within dispersions occurs when the phase volume of particles is above their random close packing (Berghout et al., 2015; Shewan and Stokes, 2015).

In food application, preserving native conformations of SPI is difficult hence the use of commercial SPI is more practical. Although many studies have reported on the rheological properties of soy protein gels using commercial SPI, there are limited explanations on structural differences at various length scales. Therefore, this study aims to provide insight on how structural differences at molecular, mesoscopic, and macroscopic scales contribute to rheological properties of commercial SPI dispersions. The provided insight would enhance utilisation and appropriate selection of commercial SPI for the purpose of research towards application in designing high protein foods.

4.2 Experimental

Comparative study between laboratory-prepared soy protein isolate (Lab SPI) and three different commercial samples, i.e. Supro 548, 670, and 760, were performed. Prior to protein isolation, whole soybean flour was defatted according to a method by Bainy et al. (2008) with modifications. The flour was suspended into hexane in a sealed container and stirred for 1 hour at room temperature. The suspension was then settled for 2 hours to let the flour sediment. The hexane was carefully decanted, and the defatted soybean flour was left to dry overnight in the fume hood. Soy protein isolate (SPI) was prepared using a method described by Molina et al. (2001) with modifications. Defatted soy flour was suspended in deionised water at 1:6 ratio and continuously stirred. While stirring, the pH of the suspension was adjusted to 9 by addition of 1 M NaOH solution. After 1 hour stirring, the suspension was centrifuged at 5000 g and 4 ^{o}C for 20 minutes. The supernatant containing alkaline soluble protein was collected. The sediment was resuspended in deionised water and the steps were repeated for two times. The collected supernatant was acidified using 1 M HCl solution to the isoelectric point at pH 4.5 and appeared as turbid dispersion. The dispersion was then centrifuged at 5000 g and 4 ^{o}C for 20 minutes. The supernatant was discarded, and the protein pellet was collected. The pellet was washed by resuspending in deionised water then followed by centrifugation. The washed pellet was neutralised by resuspending in water and having pH adjustment to 7 using 1 M NaOH solution, followed by centrifugation, and the neutralised pellet was collected. Finally, the pellet was freeze-dried to obtain Lab SPI powder.

A procedure to prepare SPI dispersions is described as follows: SPI powder was dispersed in deionised water at 14% (w/w) concentration. The dispersions were magnetically stirred at 5 ^{o}C for at least 60 min until fully hydrated in a sealed vial at low speed to avoid foaming. The dispersions were then diluted with deionised water to achieve the required final concentrations, i.e. 0.1, 1, 5, or 10% (w/w), that were subjected to various measurements and analyses. Where the use of solid-rich concentrated dispersions is required, vigorous hand mixing with a spatula was applied prior to magnetic stirring to achieve homogeneity. The diluted SPI dispersions were kept at 5 ^{o}C prior to analysis and analysed within 24 hours after preparation. All SPI sample dispersions at 5% (w/w) concentration were within the neutral pH range at 7.08-7.36, hence the effect of pH was minimised.

Characterisation of SPI samples at molecular scale was conducted by resolving protein molecular weight distribution using SDS-PAGE, evaluating conformational differences using micro-DSC FTIR spectroscopy. Protein solubility of dilute sample dispersions were measured. Insoluble fraction of SPI dispersions was characterised by using light microscopy, particle size distribution analysis, and multiple light scattering. Dispersed phase volume of insoluble particles was also quantified. Rheological properties of sample dispersions were evaluated using rotational and oscillatory rheology. All measurements and analyses were conducted according to relevant methods that have been described in the Chapter 3.

4.3 Results and discussions

4.3.1 Polypeptide constituents and predicted conformation

The resolved SDS PAGE bands represent various constituting polypeptides within SPI samples (Figure 4.1). Lab SPI, Supro 548, and 760 showed a typical SDS PAGE patterns of individual subunits that belong to major soybean proteins, i.e. β-conglycinin and glycinin. Ratios between the two seems to be varied as indicated by band intensity differences, e.g. less intense β-conglycinin band from the Lab SPI and strong intensities of glycinin subunits on all three samples, which might be attributed to varieties of soybean cultivars and methods of protein extraction (Sirison et al., 2017; Wu et al., 2000). In contrast, Supro 670 exhibited polypeptide constituents with lower molecular weight and the absence of typical β-conglycinin and glycinin subunits. The most possible reason for this is that the manufacturing of this sample involved hydrolysis of proteins, particularly glycinin, that led to a reduced molecular weight, as previously reported (Rutherfurd et al., 2011).

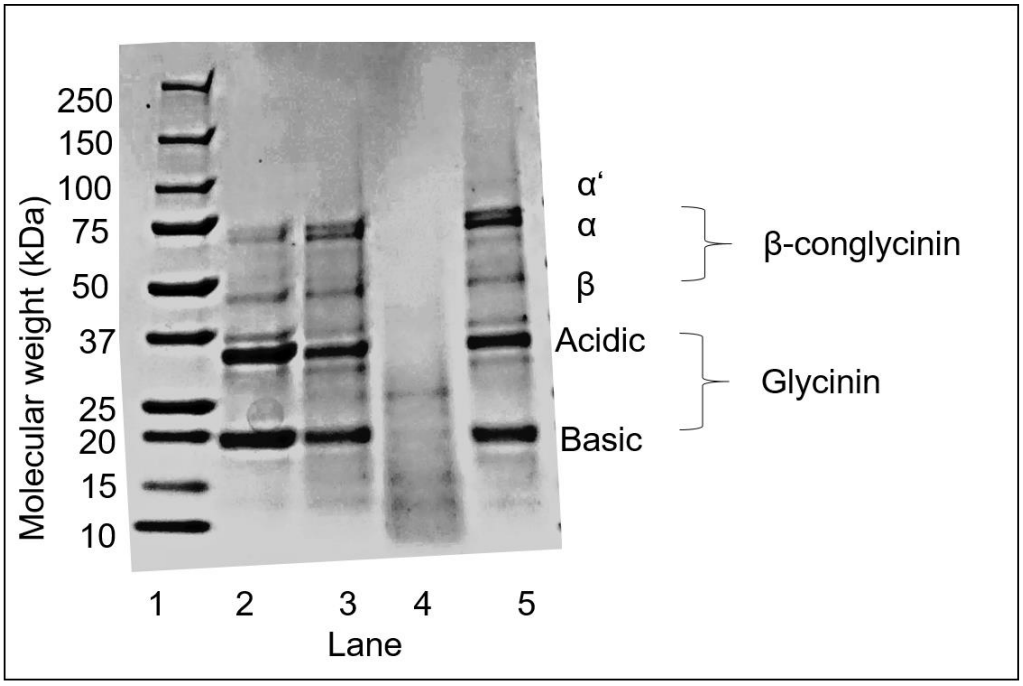

Figure 4.1 SDS PAGE of soy protein isolate samples. Lane number 1: standard protein marker; 2: Lab SPI; 3: Supro 548; 4: Supro 670; 5 Supro 760. The results are representative of duplicate experiments.

Conformational differences of SPI samples are first identified by micro-DSC. Despite sharing similar SDS PAGE profiles, commercial SPI samples showed different thermal properties from the Lab SPI (Figure 4.2). The absence of thermal events within commercial SPI thermograms indicated the proteins are already in a denatured and aggregated form. This is unsurprising since manufacturing of commercial SPI commonly involves high temperature drying (Singh et al., 2008). On the other hand, the thermogram of Lab SPI showed an endothermic peak at about 90 ^{o}C suggesting a structural transition taking place. The transition can be attributed to unfolding of already denatured proteins due to alkaline exposure upon preparation of Lab SPI. Denaturation temperature of SPI containing β-conglycinin and

glycinin have been reported as two endothermic events in which glycinin is higher than β-conglycinin (Lakemond et al., 2000; Renkema et al., 2000, 2002).

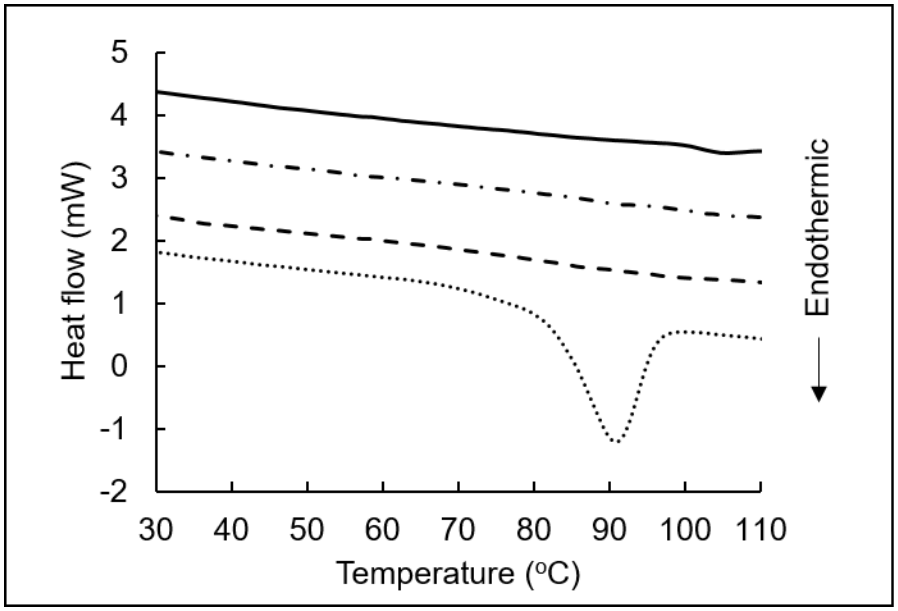

Figure 4.2 Micro-DSC thermogram of SPI dispersions at 10% (w/w) concentration and heating rate at 1 ^{o}C min^{-1}. The results are representative of duplicate experiments. Lab SPI (dotted line); Supro 548 (dashed line); Supro 670 (dashed and dotted line); Supro 760 (solid line).

Conformational differences of SPI samples were also evaluated using FTIR spectroscopy. FTIR spectra of dry SPI samples exhibited indistinguishable band positions and patterns between samples (Figure 4.3). However, the spectra can be useful as reference for absorption bands of interest in resolving protein secondary structure, i.e. amide I and II. Sharp peaks of amide I bands appeared at ~1633-1636 cm^{-1} that predominantly arise from

C=O stretching vibrations of the protein backbone. Less intense peak of amide II bands located at ~1520-1524 cm^{-1} results from C-N stretching and N-H bending vibrations (Barth, 2007).

FTIR spectra of SPI dispersions showed different peak positions compared to the spectra of dry sample (Figure 4.3). It is important to note that the use of D_2O in FTIR spectroscopy study of protein will cause hydrogen-deuterium (H-D) exchanges between D_2O and protein, leading to conversions from N-H to N-D due to replacement of hydrogen by deuterium atom (Barth, 2007). Structural differences between native and denatured SPI were observed in the amide II' peak at 1400-1500 cm^{-1}. The same peak position for amide II' were observed for all samples at ~1443 cm^{-1} with the least intensity on Lab SPI spectra and showing residual peak of amide II at ~1561 cm^{-1} as a result of incomplete H-D exchanges. This clarified that H-D exchanges were prevented to take place inside the protein core due to native folded structure, whereas the other denatured SPI samples exhibit larger amount of N-deuteration due to an unfolded structure (Kong and Yu, 2007).

Differences in secondary structure composition between SPI samples were observed through Amide I peak position and can be further resolved using second derivative spectra (Figure 4.3). The peak of Lab SPI located at the highest wavenumber among all samples, i.e. ~1635 cm^{-1}, whereas Supro 548, 670, and 760 were at ~1629, ~1624, and ~1632 cm^{-1} respectively. These peak positions may sufficiently indicate the predominant secondary structure of soy protein was β-sheet in agreement with other studies (Guerrero et al., 2014; Hu et al., 2013; Tang and Ma, 2009; Zhang et al., 2012). Further examination using second derivative spectra clearly

separated major band position of Lab SPI to ~1634 cm^{-1} corresponding to intramolecular β-sheets structure, whereas the commercial SPIs' major band positions at ~1622-1624 cm^{-1} are responsible for intermolecular β-sheets of protein aggregates (Schmitt et al., 2009; Shivu et al., 2013).

As expected from the amide I band position, β-sheet appeared as major secondary structure in all SPI samples including intramolecular parallel and intermolecular antiparallel β-sheet structures that mainly found in native and denatured protein respectively. Interestingly, proportion of β-turn was larger in commercial SPI samples, which has been reported as contributing structure to the insoluble aggregates (Tang and Ma, 2009).

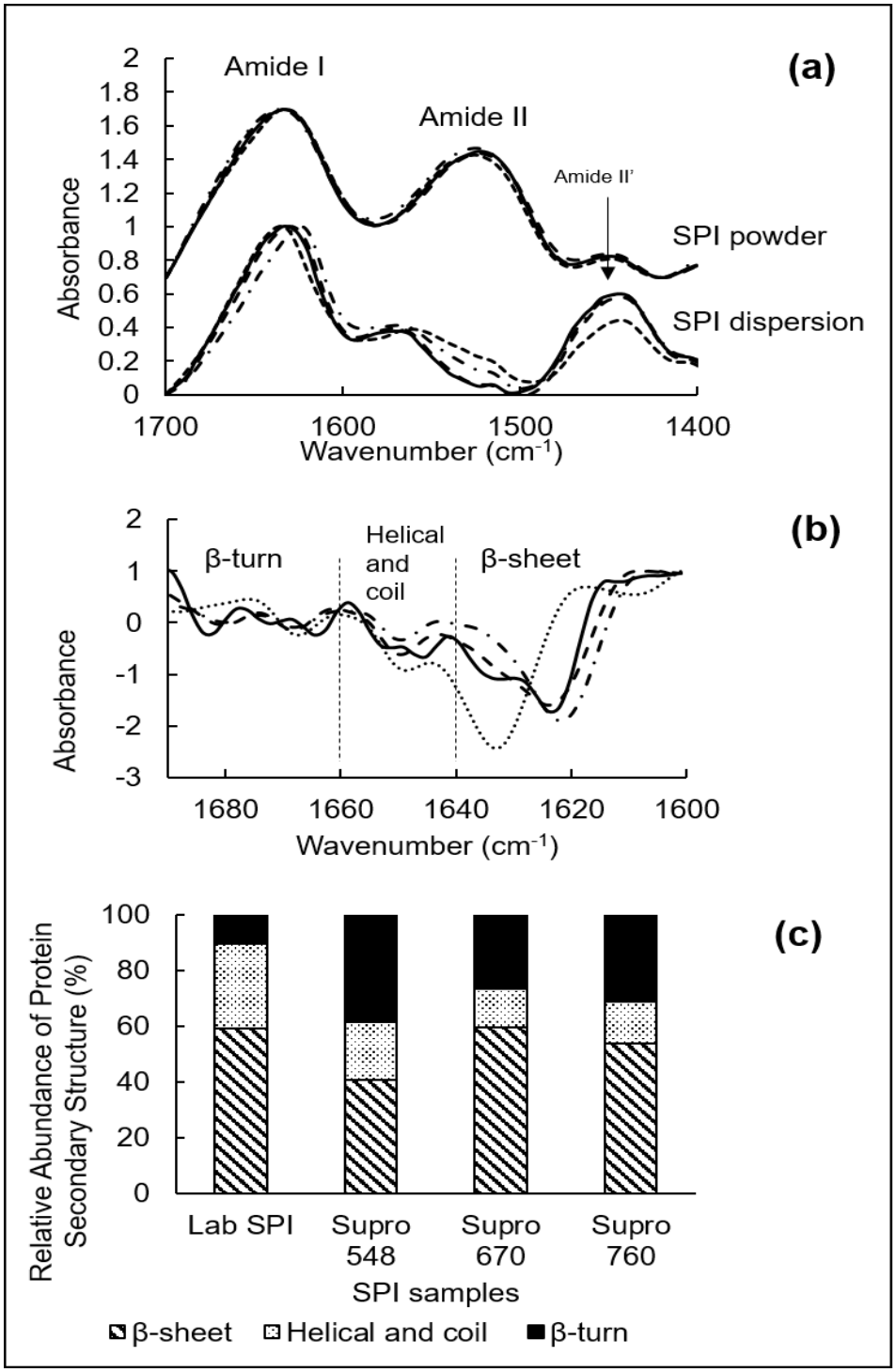

Figure 4.3 FTIR spectra of SPI samples in dry powder and dispersion forms (a); second derivative spectra of SPI dispersions at amide I band (b); and relative abundance of protein secondary structure within SPI samples (c). Lab SPI (dotted line); Supro 548 (dashed line); Supro 670 (dashed and

dotted line); Supro 760 (solid line). The results are the average of duplicate experiments.

4.3.2 Protein solubility and physical properties of insoluble SPI fraction

It is expected that soy protein in its native structure exhibits high solubility (Tang et al., 2006b). As shown in the

Table 4.1, Lab SPI exhibited the highest protein solubility due to its preserved native conformation. Commercial samples with the least protein solubility were Supro 760 and 548 showing 18.94 and 28.34 g/ 100 g SPI, respectively. Higher degrees of denaturation are known to increase hydrophobicity of SPI and resulting in lower solubility (Wagner et al., 2000). Considering similar protein compositions and conformations between the two, slight differences in protein solubility might be due to different processing conditions. In contrast, protein solubility of Supro 670 were as high as 54.97 g/ 100 g SPI that is most likely associated with soluble aggregates of low molecular weight proteins, confirming the results from SDS-PAGE presented earlier.

Table 4.1 Soluble protein concentration and insoluble particle mean diameter of different SPI samples

SPI samples	Soluble protein concentration (g/ 100 g SPI)	Insoluble particle mean diameter (μm)
Lab SPI	76.26 ± 0.54	3.89 ± 0.10
Supro 548	28.34 ± 2.35	68.95 ± 2.20
Supro 670	54.97 ± 2.02	36.80 ± 2.10
Supro 760	18.94 ± 1.00	71.37 ± 4.33

Characterisation on SPI insoluble fractions were performed at dilute concentrations, hence considering swelling-ability of samples, the observed particles were in the swollen state. Microscopy images of insoluble particles within SPI dispersions showed variations in morphology and size (Figure 4.4). Due to the lack of useful observation of specific patterns at available maximum magnification, the Lab SPI microscopy image is not displayed. Supro 548 and 760 appeared as transparent particles due to water penetration. The former was an irregular granular shape, while the latter was more spherical and larger in size due to swelling. Considering similar protein compositions and low solubility of both samples, a relatively high protein concentration occurs within the structure of insoluble particle. However, differences in water retention is attributed to morphological microstructure of SPI particles as suggested by Urbonaite et al. (Urbonaite et al., 2014). Conversely, Supro 670 was distinguished as spherical dark particles with a wide size range. The dark colour suggests a characteristic of densely packed small aggregates into spherical shape. This can be explained as

manufacturing of SPI from low molecular weight proteins were unable to build morphological structures with water-retaining ability.

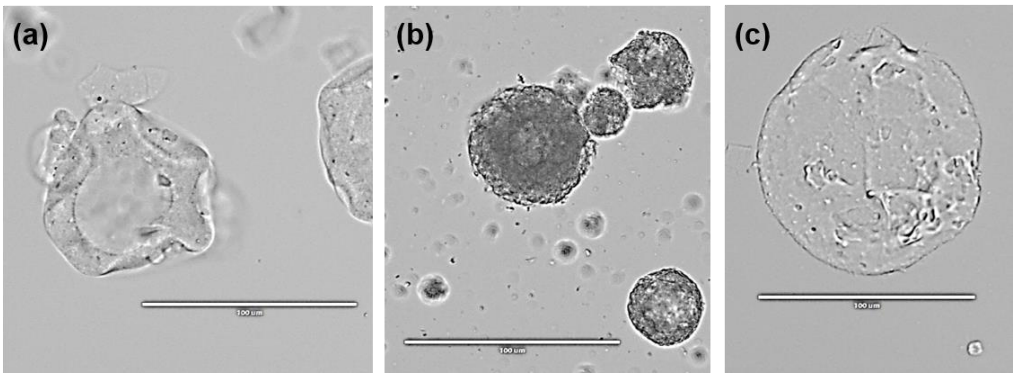

Figure 4.4 Light micrograph of insoluble particles of SPI dispersions at 0.1% (w/w) concentration from Supro 548 (a), 670 (b), and 760 (c). Scale bar shows 100 µm.

The size distribution of insoluble particles showed noticeable differences between Lab SPI and commercial samples (Figure 4.5). Despite its preserved native conformation and high protein solubility, the Lab SPI dispersion contained small particles mainly distributed between 0.1-10 µm that might be attributed to the aggregates of denatured β-conglycinin. As confirmed from microscopy observation, Supro 548 and 760 mostly contained large insoluble particles distributed between 10-200 µm. Although morphological features between the two were clearly different, their mean diameter particle size were only slightly different due to sphericity assumption of laser diffraction particle sizing. This means the actual mean diameter size of irregular wrinkled-shape Supro 548 might be smaller than

the calculated result. Supro 670 dispersion showed major distribution of large particles between between 10-100 µm with apparent distribution of small particles below 10 µm. Considering the commercial samples have a largely denatured protein conformation, differences in size distribution can be associated with the different molecular weight of proteins involved within insoluble fraction.

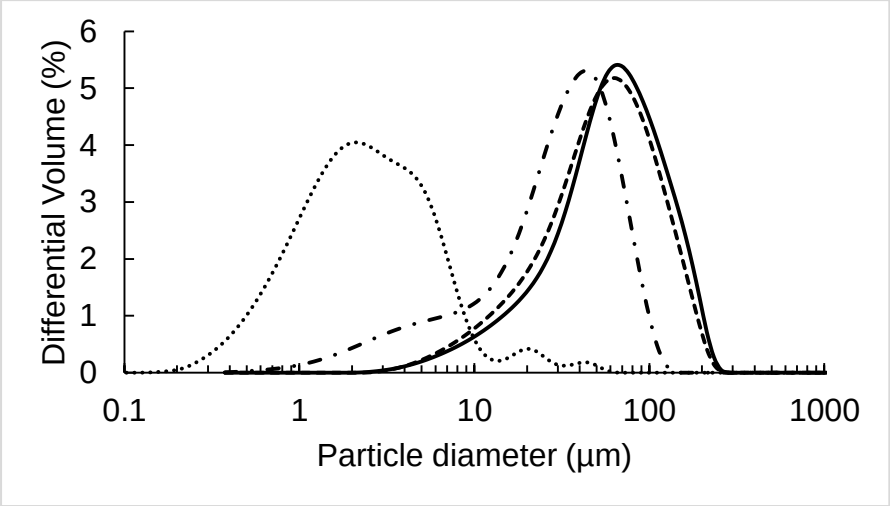

Figure 4.5 Particle size distribution of SPI dispersions at 1% (w/w) concentration. Lab SPI (dotted line); Supro 548 (dashed line); Supro 670 (dashed and dotted line); Supro 760 (solid line). The results are the average of duplicate experiments.

Sedimentation of insoluble fraction were observed from SPI dispersions at 1 and 10% (w/w) concentration after 30 min settling under normal gravity. All commercial samples showed sedimentation with different height of beds at 1% concentration (Figure 4.6a). The lowest sediment bed was observed on Supro 670 dispersion due to relatively high amounts of soluble fractions and

smaller insoluble particle diameter size, followed by SPIs with larger particle size creating higher sediment bed. In contrast, Lab SPI did not show any sedimentation at the bottom of the vial due to high protein solubility. Light backscattering intensity of dispersion is dependent to the particle diameter size and their volume fraction, with decreasing particle size lead to an increase of backscattering intensity specifically when particles are larger than wavelength of incident light at 880 nm, and increasing volume fraction lead to an increase of backscattering intensity within the range of 0.1-10% volume fraction (Formulaction SAS, 2007). Variations in light backscattering intensity of sediment bed were also observed and can be attributed to the particle mean diameter size (

Table 4.1 Soluble protein concentration and insoluble particle mean diameter of different SPI samples). Supro 670 had nearly triple the backscattering intensity of its corresponding commercial SPIs, followed by 548 and 760, respectively.

Increasing SPI concentration to 10% led to higher sediment beds of Supro 670 and nearly stable Supro 548 showing slightly separated phase at the top of the vial (Figure 4.6b). However, phase separation was no longer observed on 10% Supro 760 dispersion due to full volume occupancy of highly packed particles. Supro 760 particles were restricted to swell as indicated by higher light backscattering intensity compared to Supro 548, meaning that particle size of Supro 760 is smaller than Supro 548 due to volume packing at 10% concentration. Lab SPI showed a stable dispersion without sedimentation with high intensity of light backscattering due to very low volume fraction of small insoluble particles.

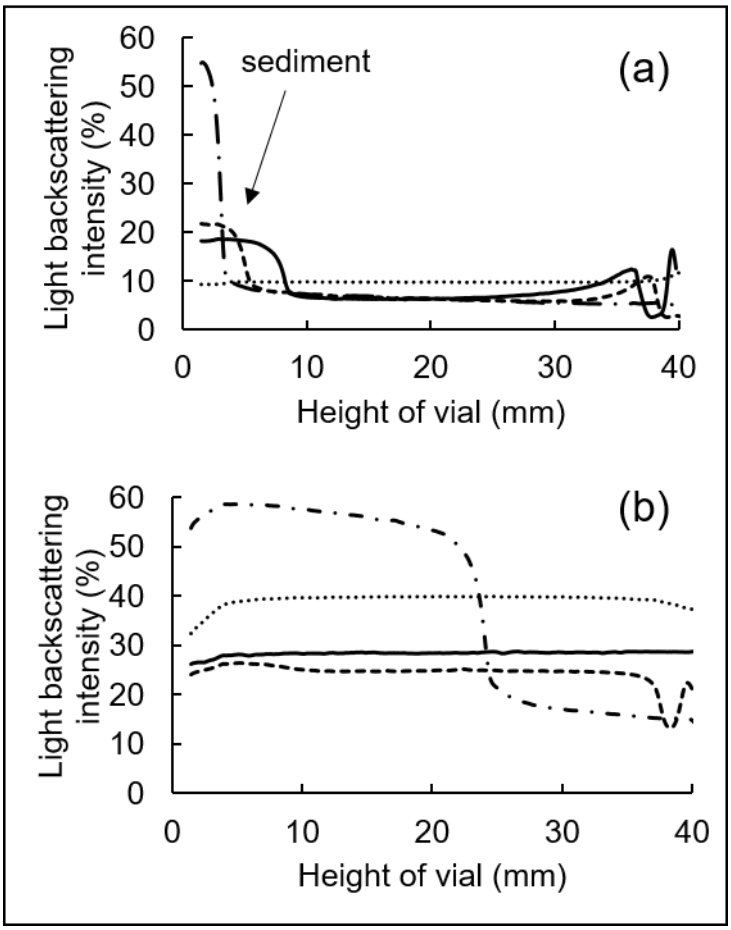

Figure 4.6 Light backscattering intensity of SPI dispersions across the height of vial measured after 30 min sedimentation at 1% (a) and 10% (b) concentration. Lab SPI (dotted line); Supro 548 (dashed line); Supro 670 (dashed and dotted line); Supro 760 (solid line). The results are representative of duplicate experiments.

The measured height of the sediment bed also provides information on dispersed phase volume fraction of insoluble particles under normal gravity. However, estimation on phase volume fraction in this study were using centrifugal forces at 1500 times of normal gravity to minimise the differences in swelling-ability and hence considered as deformable particles. At the same

concentration and considering particle de-swelling due to centrifugal forces, SPI particles with larger size resulted in a higher phase volume (Figure 4.7). Phase volume of soft particle dispersions is known to highly affects their rheological properties which behave differently at below and above random close packing, which is often referred to as 64% phase volume of monodisperse hard sphere particles (Shewan and Stokes, 2012). Discussion on phase volume will be further used to explain rheological properties of dispersions.

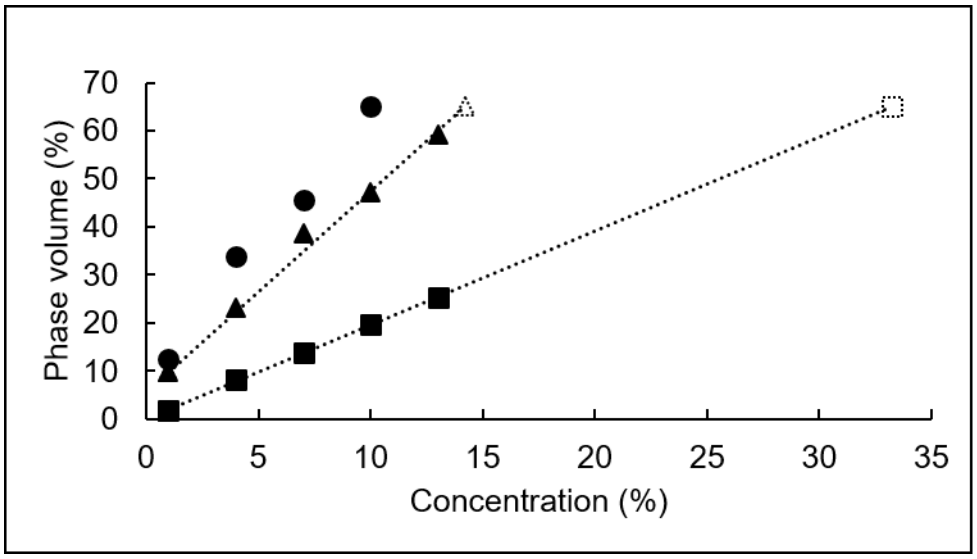

Figure 4.7 Dispersed phase volume of commercial SPI dispersions at various concentrations. Supro 548: measured (filled triangle) and extrapolated (open triangle); Supro 670: measured (filled square) and extrapolated (open square); Supro 760: measured (filled circle). The results are the average of duplicate experiments.

4.3.3 Rheological properties of SPI dispersions

As shown in Figure 4.8, increasing concentration of different SPI samples led to changes in specific viscosity and flow behaviour of dispersions to varying extents. At 10% concentration, Lab SPI and Supro 670 dispersions exhibited the lowest viscosity increases and remained showing Newtonian behaviour as shown by their Power Law indices around 1 (Vercet et al., 2002). Low viscosity of Lab SPI dispersion is mainly due to high solubility of high molecular weight globular proteins in native structure with unexposed hydrophobic groups, hence attribution to phase volume of particles may not be relevant. However, low viscosity of Supro 670 dispersion is attributed to highly soluble protein aggregates and small size insoluble particles made up of low molecular weight proteins occupying low phase volume even at 10% (w/w) concentration. This is in agreement with other's research on non-colloidal soft particle dispersions in water following monodisperse hard sphere model behaviour as being Newtonian at low phase volume (Shewan and Stokes, 2015). It is expected that dispersions containing larger insoluble particle size exhibited higher viscosity due to higher dispersed phase volume fraction. Increasing concentration of Supro 548 and 760 within dispersions tremendously increased their specific viscosity. At 10% (w/w) concentration, insoluble particles within Supro 548 dispersion occupied about 47% phase volume hence showing high viscosity and slightly shear thinning behaviour indicated by decreasing Power Law index. Supro 760 dispersions began to exhibit shear thinning behaviour as low as 4% (w/w) concentration due to large particle size. Shear thinning behaviour of dispersions can be explained as spatial rearrangement of dispersed particles and anisotropic deformation

(Utrilla-Coello et al., 2014). Shear thinning behaviour of SPI dispersions at above 10% concentration were also confirmed in other studies (Hu et al., 2013; Jambrak et al., 2009).

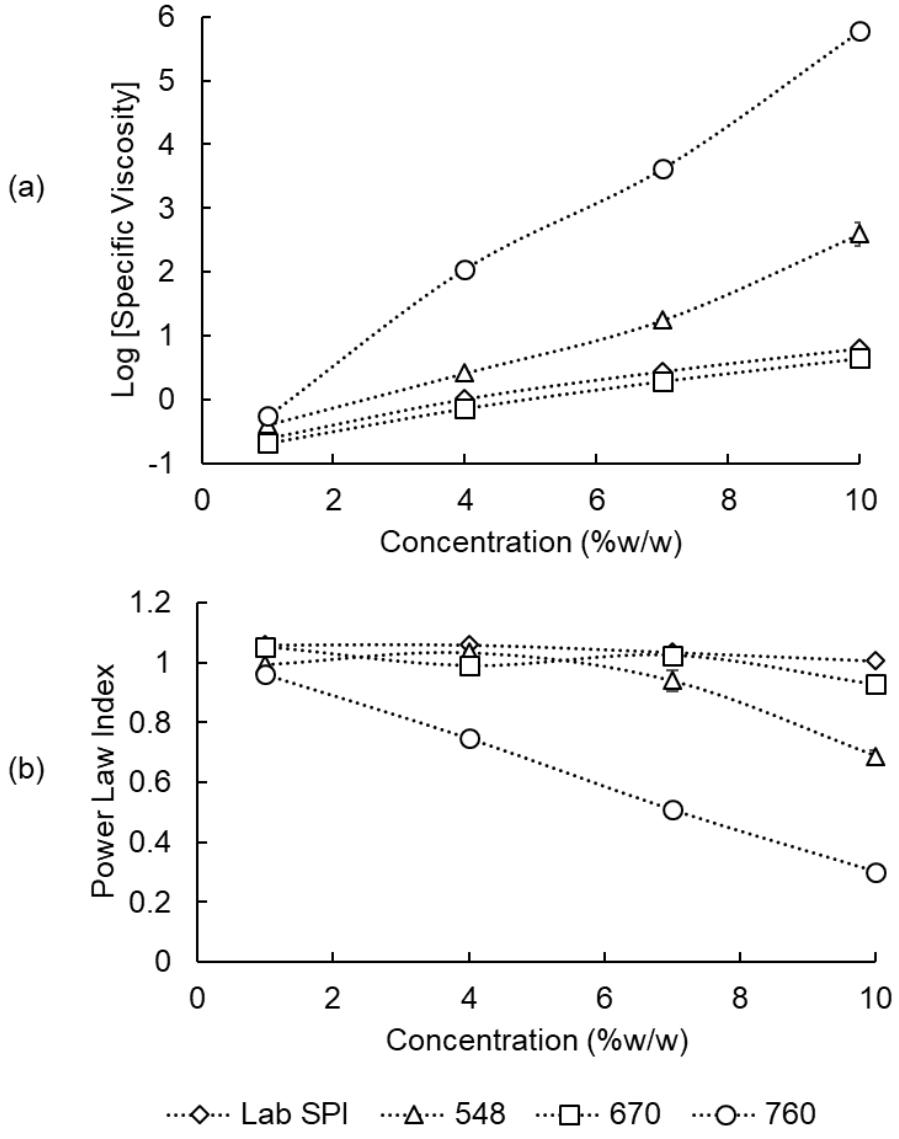

Figure 4.8 Logarithmic plot of viscosity of SPI dispersion at 10% (w/w) concentration as a function of shear rate (a); and specific viscosity at various concentration. Lab SPI (diamond); Supro 548 (triangle); Supro 670 (square); Supro 760 (circle). The results are the average of duplicate experiments.

Evaluation on the viscoelastic properties of dispersions were conducted on commercial SPI samples emphasising the contribution of insoluble particles at a fixed estimated phase volume. A 65% phase volume was selected assuming SPI particles above random close packing based on the observation of Supro 760. Calculation of SPI concentration was extrapolated from linear regression of concentration-phase volume curve (Figure 4.7), therefore at the same phase volume, Supro 670 contained the highest solid concentration while Supro 760 was the lowest. All concentrated SPI dispersions exhibited viscoelastic behaviour as expected from high phase volume (Figure 4.9). The highest modulus of Supro 670 dispersions was attributed to higher surface area of smaller rigid particles that deeply jammed and created the longest linear viscoelastic region (LVER). Their non-LVER showed strain-thinning behaviour as the strain increased, and which continuously breaks the structure of jammed particles at high amplitude strain. Slightly different behaviour was observed on Supro 548 and 760 showing the shorter LVER, then continued by weak and strong strain overshoots respectively at non-LVER prior to crossover point when amplitude strain closer to 100%. The strain overshoots within non-linear viscoelastic region were attributed to large size and deformability of both SPI particles that led to some extent of structural rearrangement at high amplitude strain prior to breakage, i.e. increasing modulus as the strain increase then continuously decreasing.

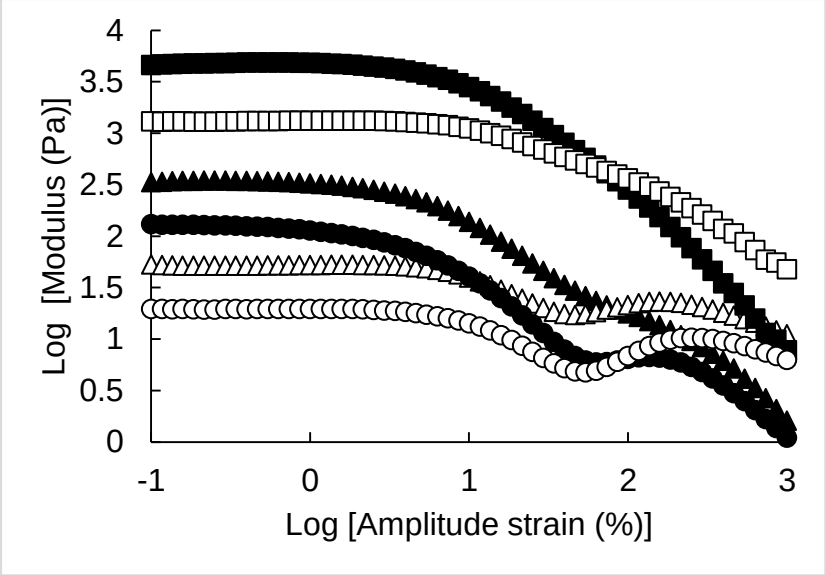

Figure 4.9 Storage (filled symbols) and loss modulus (open symbols) of SPI dispersions at approximately 64% volume fraction as a function of amplitude strain. Supro 548 (triangle); Supro 670 (square); Supro 760 (circle). The results are representative of duplicate experiments.

Viscoelastic gel behaviour of concentrated SPI dispersions were confirmed by predominant elastic component throughout the frequency ranges up to 200 rad.s^{-1} without appearance of crossover point due to high interparticle physical interactions of a jammed system (Figure 4.10). Frequency dependence of storage and loss moduli appeared at varying degrees demonstrating higher modulus with increasing frequency. Supro 670 showed the most frequency-dependence of storage modulus indicating weaker structure with a slope of 0.14±0.01 that is attributed to smaller particle radius, whereas concentrated dispersion containing larger particles of Supro 548 and 760 showed less dependency with the slope of 0.10 and 0.07, respectively.

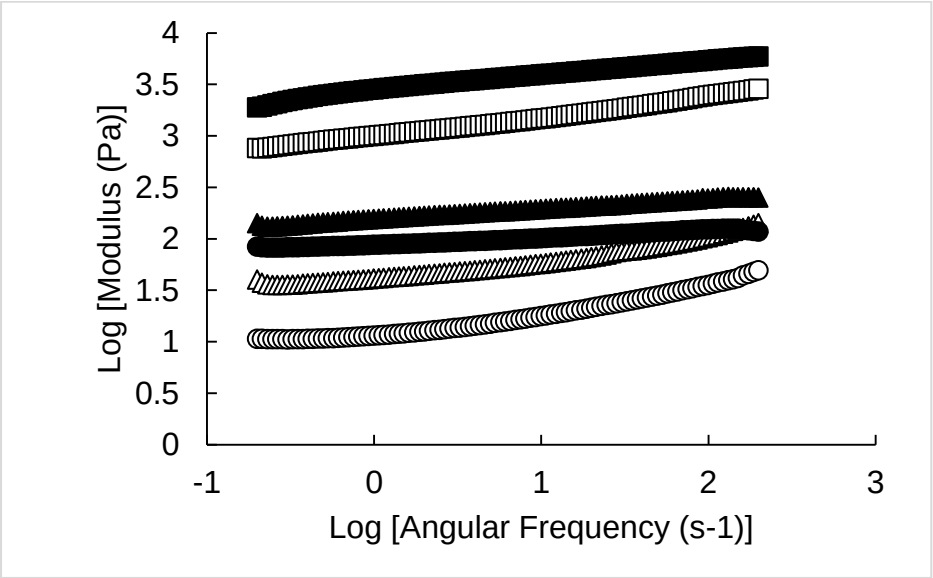

Figure 4.10 Frequency dependence of storage (filled symbols) and loss modulus (open symbols) of commercial SPI dispersions at estimated volume fraction above random close packing. Supro 548 (triangle); Supro 670 (square); Supro 760 (circle). The results are representative of duplicate experiments.

4.4 Conclusions

This study confirms structural differences of several commercial SPIs at multiple length scales. The evaluation on polypeptide constituents reveals that low viscosity commercial SPI consisted of only low molecular weight proteins, whereas the rest of SPIs indicated the presence of glycinin β-conglycinin as major protein constituents. All commercial SPIs showed a fully denatured structure, in contrast to the highly soluble laboratory-prepared SPI. Viscosity of dispersions at the same SPI concentration were highly influenced by physical factors, such as insoluble particle shape and size

distribution. Furthermore, the use of estimated insoluble particle phase volume, instead of concentration, was able to explain the differences in viscosity and viscoelastic behaviour. The provided insight is expected to contribute on the utilisation of commercial protein materials for development of high protein foods.

5 Heat-induced structural changes of soy protein isolate dispersion with limited solubility

5.1 Introduction

High intake of dietary protein is often associated with health beneficial effects. Among the key benefits is to help body weight maintenance by providing satiety sensations (Halton and Hu, 2013). In addition to protein-stimulated physiological aspects, the generated satiety effects are more favourable with consumption of foods in the solid form (Chambers et al., 2015; Larsen et al., 2016; Morell and Fiszman, 2017; Tang et al., 2016). Therefore, structure formation and solidification of high protein foods is of interest in providing satiety.

Tofu is an example of solidified food protein with shared characteristics of food gels that provide satiating properties (Williamson et al., 2006). Gelation during production of tofu involves protein coagulation from soymilk that traditionally induced by salts or acids. Heat treatment on soymilk causes protein denaturation followed by formation of soluble aggregates. The presence of coagulants reduces the net charge of protein aggregates, either by increasing ionic strength or lowering pH close to the isoelectric point, that leads to less repulsive forces between proteins and formation of insoluble protein aggregates (Saowapark et al., 2008). Later development on tofu gelation involves protein crosslinking by using transglutaminase enzyme with some advantages of stability against high temperature and pressure (Kwan and Easa, 2003; Tang et al., 2007). The presence of insoluble protein

contributes to the building of three-dimensional structure and hence highly determine textural properties of tofu. The resulting tofu displays characteristic of self-supporting gel with various degree of firmness.

The use of soy protein isolate (SPI) have been reported in many studies related to tofu properties, rather than using traditional soymilk (Campbell et al., 2009; Hu et al., 2013; Hui et al., 2000; Wang et al., 2018). However, since many commercially available SPI are at least partially denatured and showing limited solubility, there are lack of explanation on the contribution of SPI insoluble fraction to SPI tofu-type gel structure. Therefore, this study aims to demonstrate heat-induced structural changes of commercial SPI dispersions with limited solubility as affected by calcium chloride salt ($CaCl_2$) and microbial transglutaminase enzyme (MTGase). $CaCl_2$ is commonly used as coagulant in production of firm tofu, whereas MTGase is an effective crosslinking enzyme for many proteins, including soybean (Hsiao et al., 2015; Yang et al., 2013). Findings from this study would provide insight into utilisation of commercial SPI for development of high protein food in a solid form similar to tofu.

5.2 Experimental

This work utilised the commercial Supro 760 SPI sample that has been discussed in Chapter 4. The SPI is of interest due to it exhibiting relatively high dispersed phase volume at lower concentration compared to other samples. The study was preceded by comparing heat-induced viscoelastic and structural changes of Supro 760 SPI against the highly soluble sample,

denoted as Lab-SPI. Oscillatory rheology with temperature sweep tests were performed with two cycles of ramp up and down scenarios at the rate of 2 ^{o}C min^{-1}. Fourier transform infrared (FTIR) spectroscopy analysis was also performed to resolve heat-induced changes on relative abundance of protein secondary structures.

Heat-induced structural changes of SPI dispersions as affected either by $CaCl_2$ or MTGase which were evaluated by means of oscillatory rheology, scanning electron microscopy, and FTIR spectroscopy. $CaCl_2$ solution was added upon dilution of SPI dispersion from 14% (w/w) to the required final concentration, i.e. 0.1, 1, or 10% (w/w) SPI concentration in the presence of $CaCl_2$ at 0, 5, 10, or 20 mM. SPI dispersions containing $CaCl_2$ were left stirred and analysed within 2 hours. MTGase-containing SPI dispersions were prepared by adding the enzyme solution at the last step of dilution to the final concentration, i.e. 10% or 13% (w/w) SPI concentration with enzyme addition up to 20 U g^{-1} SPI. The dispersions were constantly stirred and were analysed within 5 min after preparation to avoid excessive crosslinking that instantaneously taking place.

Solidified gels were prepared from thermally treated SPI dispersions with final concentration of 13% (w/w) that contains $CaCl_2$ or MTGase. Where the samples were subjected to rheological amplitude sweep tests, *in situ* heat-induced solidification were applied using a rheometer (Physica MCR 301, Anton Paar, Austria) with serrated parallel plate geometry as described by Avanza et al. (2005), with modifications. The temperature was increased to 40 ^{o}C and held for 30 min, then increased to 95 ^{o}C and held for for 5 min,

then cooled back to 20 ^{o}C without applying any mechanical shear or strain. Another preparation method involved heating SPI dispersions inside a cellulose tube with the same heating-cooling scenario. The solidified SPI gels were stored at 5 ^{o}C and subjected to scanning electron microscopy observation within 24 hours.

5.3 Results and discussion

5.3.1 Heat-induced structural changes of SPI dispersions with different conformations

Comparison of storage and loss moduli of both SPI dispersions as affected by temperature changes are presented in Figure 5.1. Prior to heating, Supro 760 SPI dispersion at 10% (w/w) concentration exhibited elastic-dominant behaviour. Domination of storage modulus over loss modulus is due to strongly interacting insoluble protein particles at high dispersed phase volume above random close packing that create network and entrap major amount of the water as continuous phase as discussed in the previous chapter. During the temperature sweep, the storage and loss modulus decreased with increasing temperature, and vice versa. Thermo-reversibility of modulus is most likely due to temperature-dependency of non-covalent interactions involved within the protein particle network. At the end of the temperature sweep, both moduli seem to be similar to the initial values. In contrast, the same concentration of Lab-SPI dispersion showed liquid-like properties with loss modulus higher than storage modulus. Viscous-dominant behaviour remains unchanged during the first heating until the temperature

reached ~80 ^{o}C, at which gelation temperature took place, as shown by cross-over point of both moduli. Drastically increasing storage modulus is attributed to protein denaturation with concomitant aggregation and gel network formation. Development of storage and loss modulus was continued proportionally at reduced slope upon first cooling. Increasing temperature upon the second heating reduced both moduli of Lab-SPI it reached until ~75 ^{o}C, where another increase in both moduli is seen, indicating incomplete denaturation and aggregation in the first heating ramp. The observed plateau of both moduli within isothermal region at 20 ^{o}C and thermo-reversibility upon the second temperature ramp indicated contribution of non-covalent bonds similar to the Supro 760 SPI dispersion.

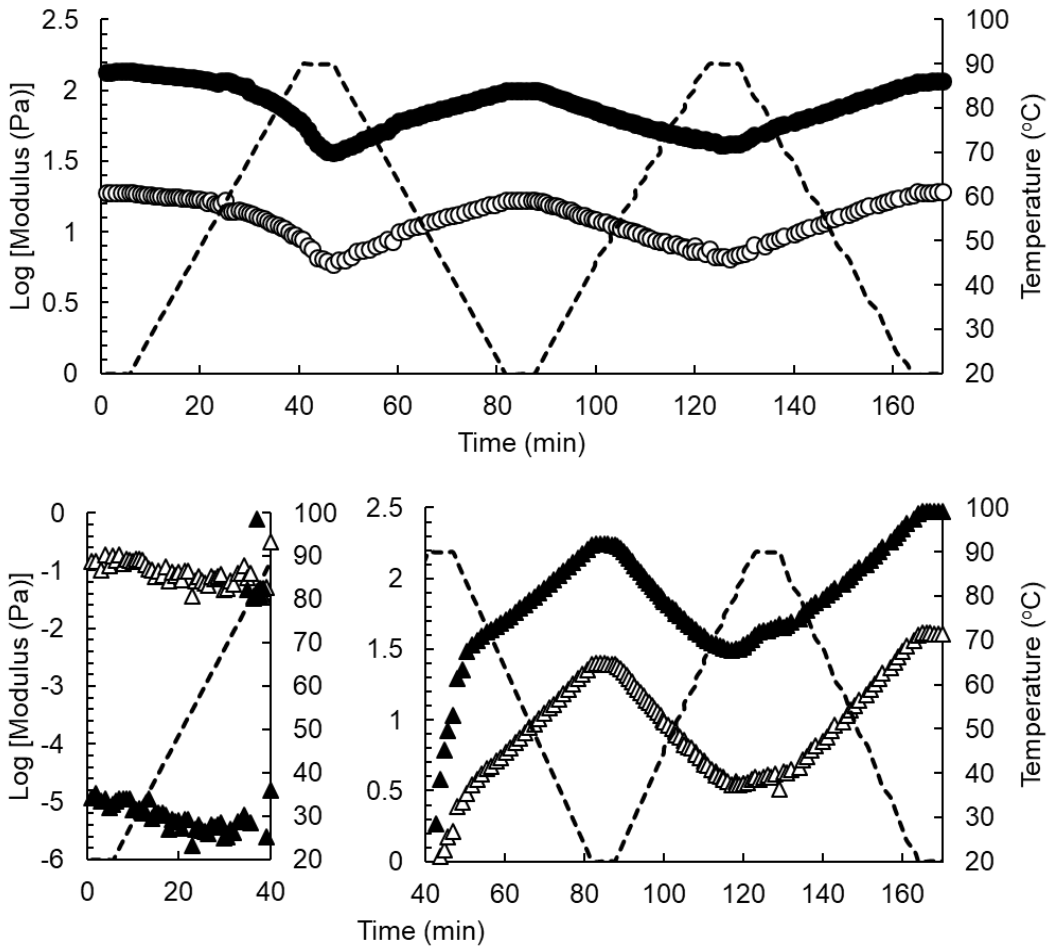

Figure 5.1 Heat-induced changes on storage (filled symbols) and loss modulus (open symbols) of Supro 760 (circles) and Lab SPI (triangles) dispersions at 10% (w/w) concentration. Temperature (dashed line). The results are representative of duplicate experiments.

Heat-induced changes of SPI dispersions were also evaluated on the smaller structural length scale, particularly on protein secondary structures. Relative abundance of different protein secondary structures was calculated from second derivative FTIR spectra within amide I region, i.e. 1600-1700 cm^{-1}. Supro 760 SPI dispersion did not show any considerable changes upon

temperature ramp-up and down (Figure 5.2). This indicated temperature-dependency of the dispersion moduli did not involve any alterations on their secondary structure at the molecular scale. The thermally stable secondary structure is most likely due to heat-induced aggregation during SPI manufacturing process that led to a formation of intermolecular β-sheet structure. In contrast, Lab-SPI showed alterations on relative abundance of protein secondary structures. Increasing temperature up to 80 ^{o}C led to a decrease of intramolecular β-sheet structure which indicated denaturation process. Interestingly, conformational changes were observed at temperatures as low as 60 ^{o}C which is lower than onset denaturation temperature obtained from micro-DSC at 80 ^{o}C (Chapter 4). This can be explained as reversible unfolding-refolding of protein that taking place below denaturation temperature (Miriani et al., 2011). The loss of intramolecular β-sheet structure upon heating proportionally increased the helical, coil, and β-turn structures that also have been observed in previous studies (Clara Sze et al., 2007; Guo et al., 2012). Further heating to 90 ^{o}C led to a formation of intermolecular β-sheet structure due to protein aggregation. Subsequent cooling of Lab SPI showed relatively stable secondary structure of aggregated protein.

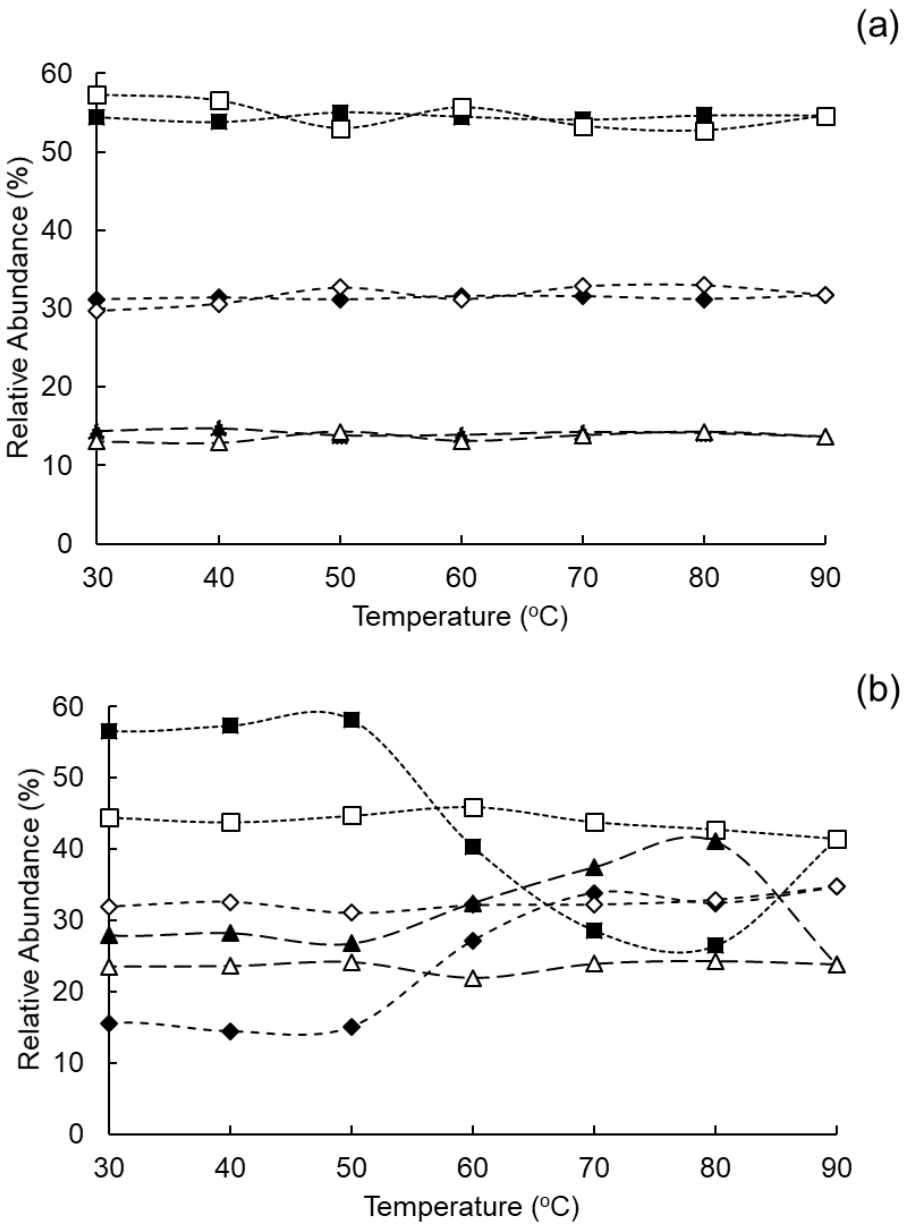

Figure 5.2 Heat-induced changes upon heating (filled symbols) and cooling (open symbols) on protein secondary structure of Supro 760 (a) and Lab-SPI (b) dispersed in D_2O at 10% (w/w) concentration. β-sheet (square); β- turn (diamond); helical and coil (triangle). The results are the average of duplicate experiments.

5.3.2 Effects of $CaCl_2$ addition on SPI dispersion

Effects of $CaCl_2$ addition to the properties of Supro 760 SPI dispersion is discussed in this section. It is known that protein solubility is expected to decrease with the presence of calcium ions. The results presented in Table 5.1 shows decreasing trend on protein solubility with increasing $CaCl_2$ concentration up to 20 mM. A steep decrease, leaving less than half of initial solubility, was observed with the presence of 10 mM $CaCl_2$, whereas higher concentration reduced solubility with lower magnitude. Protein solubility decrease due to calcium ion binding at the negatively charged sites of protein molecules, creating divalent ionic bridge, forming insoluble protein aggregates, and leading to precipitation as favoured by van der Waals attraction particularly between glycinin networks (Achouri et al., 2010; Scilingo and Añón, 2004; Yuan et al., 2002).

Table 5.1 Protein solubility and insoluble particle diameter size of 1% (w/w) Supro 760 SPI dispersion as affected by $CaCl_2$ addition

$CaCl_2$ concentration (mM)	Protein solubility (g/ 100 g SPI)	Insoluble particle diameter size (μm)	
		Mean	Median
0	18.94 ± 1.00	39.45 ± 0.73	30.36 + 2.76
5	12.59 ± 0.03	14.17 ± 0.23	9.43 ± 0.62
10	8.05 ± 1.20	17.51 ± 0.11	4.13 ± 0.05
15	9.14 ± 0.34	16.08 ± 0.34	5.17 ± 0.17
20	6.57 ± 0.06	11.60 ± 0.63	2.10 ± 0.03

Decrease in protein solubility also means higher concentration of protein involved within the insoluble particulate fraction. Microscopy observation was conducted to evaluate morphological changes within the insoluble fraction prior to and after $CaCl_2$ addition. Figure 5.3 shows two-dimensional images of insoluble particles obtained from dilute Supro 760 SPI dispersions at 0.1% concentration. In the absence of $CaCl_2$, the particles appeared to be varied in shape and size with some distinctive larger spherical shapes. The transparent greyish colour of particles indicated their water-retaining ability. However, the presence of $CaCl_2$ altered particle shapes to be more irregular and decreased particle size. In addition, the appearance of small insoluble aggregates scattered around the particles was also pronounced, as a result

of calcium-induced aggregation of soluble proteins to become small size insoluble particles.

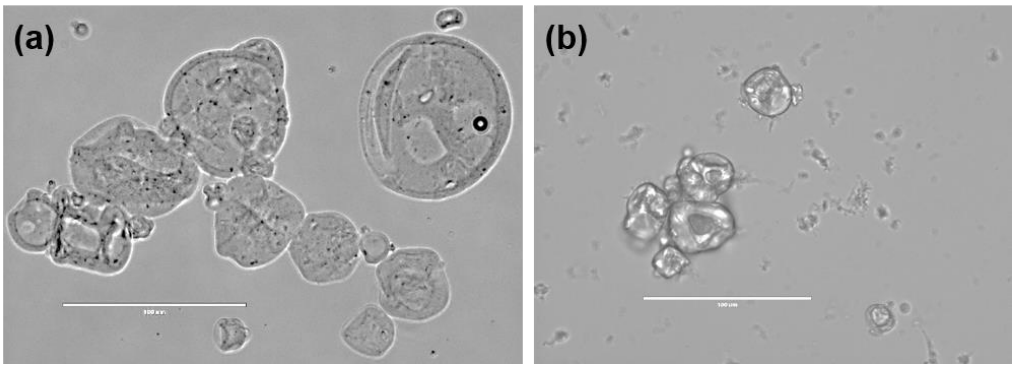

Figure 5.3 Light micrograph of Supro 760 SPI insoluble particles prior to (a) and after (b) $CaCl_2$ addition. Scale bar shows 100 µm.

Diameter size distribution of SPI insoluble particles are presented as percentage of surface area in Figure 5.4, and mean and median diameter sizes changes are listed in Table 5.1. Initially, the particles showed a monomodal size distribution with mean and median diameter sizes at around 40 and 30 µm, respectively. Addition of $CaCl_2$ up to 20 mM shifted the size distribution curve into two separated particle size populations with a sharp decline of larger particles and highly pronounced increase of smaller particles. This led to a dramatically decreasing mean and median diameter sizes to about a quarter and less than one-tenth of their initial sizes respectively. This size reduction of insoluble particles can be attributed to two different phenomena. Firstly, the shrinking of larger particles due to inability to swell. It is noteworthy that SPI ability to perform water uptake at around neutral pH is attributed to the electrostatic repulsion of negatively

charged proteins that relates to protein chain relaxation and water diffusion (Gunasekaran et al., 2006). In this study, the calcium ions weakened the electrostatic repulsions by shielding the negatively charged proteins, hence increasing net charge, and then disrupted the particle's physical structure at the surface and causing shrinkage (Sağlam et al., 2013). Secondly, decrease in mean and median diameter size is contributed by the emerging small particles below 10 μm as a result of calcium-induced aggregation of soluble proteins.

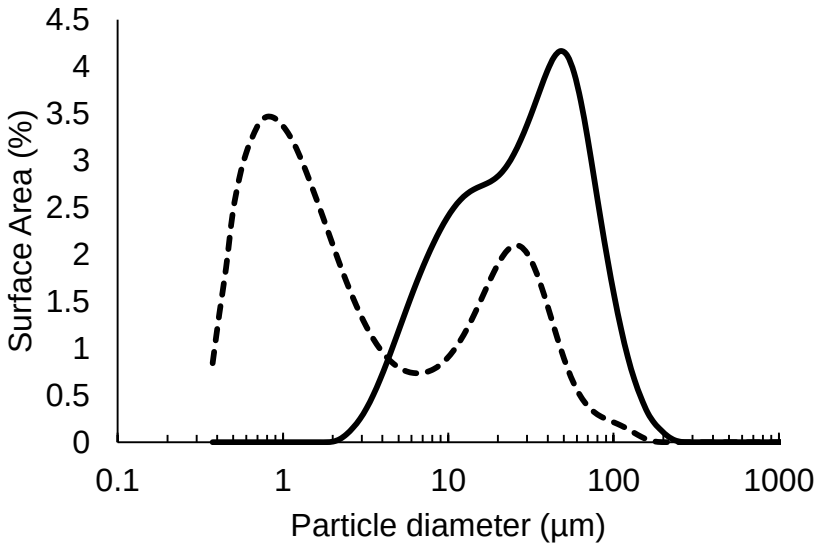

Figure 5.4 Particle size distribution of 1% (w/w) Supro 760 SPI dispersions at 0 mM (solid line) and 20 mM (dashed line) $CaCl_2$ concentrations. The results are the average of duplicate experiments.

It is important to understand how changes in solubility and the insoluble particle morphology contributes to rheology and stability of dispersion. A higher concentration of Supro 760 SPI dispersions, i.e. 10% (w/w), was used

to examine these properties considering its relevancy to high protein food applications. The effect of different ratios of protein and calcium concentrations has also been considered. Figure 5.5 showed changes in specific viscosity and Power Law index as a function of $CaCl_2$ concentration. In the absence of $CaCl_2$, a very high specific viscosity was observed with non-Newtonian behaviour as shown by Power Law index close to zero. This viscosity is contributed to by highly interacting swollen insoluble protein particles at high dispersed phase volume fraction. Viscosity of dispersions gradually decreased with increasing $CaCl_2$ concentration that can now be attributed to higher number of smaller particles due to calcium ions disruption leading to lower dispersed phase volume. Increasing $CaCl_2$ concentration from 15 to 20 mM did not further decrease the viscosity indicating maximum number of shrunken particles has been reached. Dispersions with lower viscosity tended to display Newtonian flow behaviour as shown by Power Law index closer to 1. However, the effects of smaller particles on viscosity seem to be less pronounced.

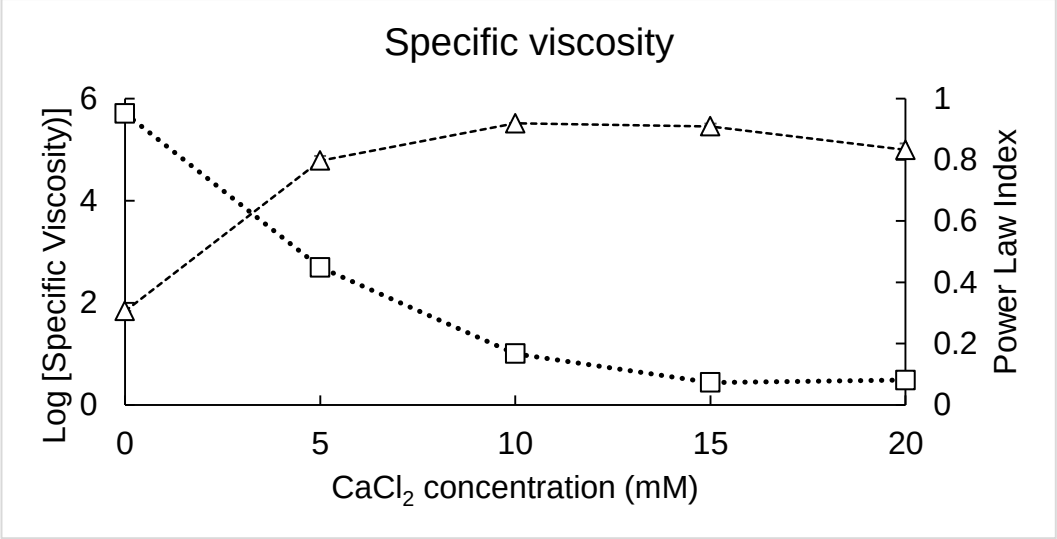

Figure 5.5 Specific viscosity (square symbols) and Power Law index (triangle symbols) of 10% (w/w) Supro 760 SPI dispersion at different $CaCl_2$ concentrations. The results are the average of duplicate experiments.

The stability of Supro 760 SPI dispersions were examined by monitoring gravitational phase separation. Figure 5.6 showed light backscattering intensity of dispersion in the absence and presence of $CaCl_2$ after settling for 60 min. Dispersions without $CaCl_2$ addition showed a uniformly distributed light backscattering intensity across the height of vial indicating a stable dispersion. In contrast, phase separation was observed in the presence of 20 mM $CaCl_2$ as shown by uneven light backscattering intensity between the upper, middle, and lower parts of vial. Higher intensity of light backscattering at the lower part of vial indicated denser structure of particle sedimented due to gravity, whereas at the upper part showed adsorption of some smaller particles to air bubbles. This also means at this calcium ion to protein ratio, a

higher protein concentration is required to occupy higher dispersed phase volume and achieve a stable dispersion.

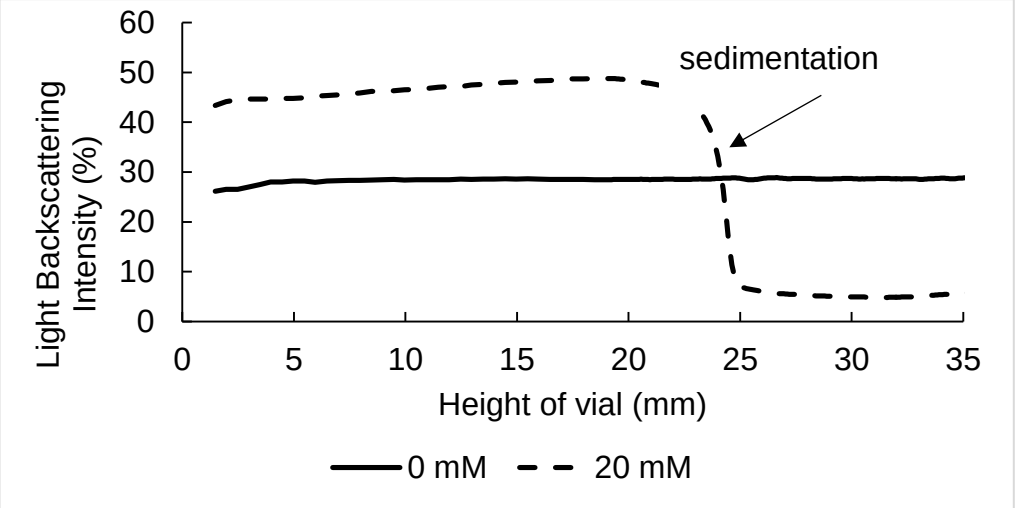

Figure 5.6 Light backscattering intensity of 10% (w/w) Supro 760 SPI dispersions across the height of vial measured after 60 min settling under normal gravity, in the absence (solid line) and presence of 20 mM $CaCl_2$ (dashed line). The results are representative of duplicate experiments.

5.3.3 Comparing the effects of $CaCl_2$ and MTGase on heat-induced SPI gels

Moduli of Supro 760 SPI dispersion were evaluated at 10% concentration upon temperature ramp in the absence or presence of $CaCl_2$ (Figure 5.7). Since all samples exhibited elastic-dominant behaviour, the presented result mainly focused on storage modulus changes. In the absence of $CaCl_2$, SPI dispersion was comprised of highly packed insoluble protein particles hence showing the highest storage modulus. Thermo-reversibility of SPI dispersion is attributed to non-covalent bonds within the structure as have been

discussed earlier. Dispersions with higher $CaCl_2$ concentration exhibited lower storage modulus due to lower dispersed phase volume of insoluble protein particles. During temperature ramp-up, dispersions with 10 and 20 mM $CaCl_2$ displayed increasing storage modulus with different magnitudes. At 10 mM $CaCl_2$ concentration, increasing modulus were observed until the temperature reached about 80 ^{o}C, followed by modulus decrease upon further heating and temperature holding at 95 ^{o}C. Similar modulus increase was more pronounced at 20 mM followed by continuous development during isothermal holding at 95 ^{o}C. Since the protein particles were occupying low dispersed phase volume, rising temperature reduced viscosity of water that led to an attractive hydrophobic interaction between protein particles followed by flocculation and aggregation. Dispersions with lower dispersed phase volume required longer time and/or higher temperature to achieve a stable aggregated structure. As the temperature quenched back to room temperature, the modulus increase was observed in all dispersions. At the end of the temperature sweep, dispersions with 20 mM $CaCl_2$ concentration achieved the highest final storage modulus emphasising formation of a stiff, solidified gel. Higher $CaCl_2$ concentration is favourable for protein aggregation due to largely distributed calcium ions that increase the number of calcium-protein bridges (Ryan et al., 2008). In addition, increasing calcium concentration within dispersions caused immense separation of insoluble protein from the continuous phase. As the separation took place, protein aggregation occurred incorporating large numbers of protein particles in creating denser solid structure as favoured by hydrophobic interactions, calcium bridges, and any other non-covalent links.

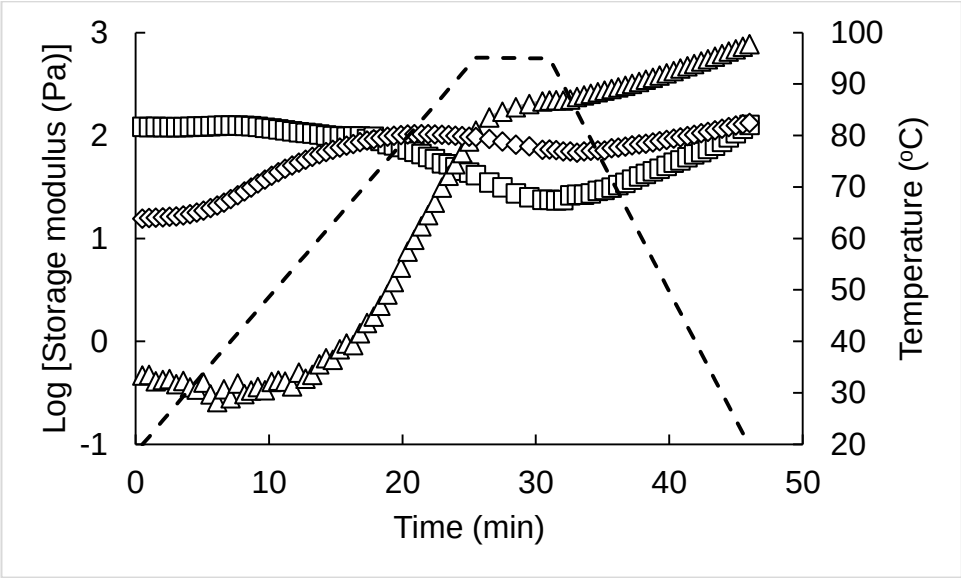

Figure 5.7 Storage modulus of 10% (w/w) Supro 760 SPI dispersions during temperature-sweep in the absence (square symbols) and presence of CaCl2 at 10 (diamond symbols) and 20 mM (triangle symbols) concentrations. Temperature programme (dashed line) was: heating at 3 ^{o}C min^{-1}, holding at 95 ^{o}C for 5 min, and cooling at 5 ^{o}C min^{-1}. The results are representative of duplicate experiments.

Similarly, storage modulus changes of Supro 760 SPI dispersion in the presence of MTGase enzyme were evaluated using temperature-sweep with different scenario involving isothermal incubation at 40 ^{o}C for 80 min and enzyme deactivation at 70 ^{o}C (Figure 5.8). In the absence of enzyme, heating and isothermal incubation decreased storage modulus of dispersion as expected from earlier discussions. Once the enzyme was added and stirred into the dispersion at room temperature, protein crosslinking begins to

take place instantaneously, as shown by higher measure storage modulus of dispersions prior to incubation. Higher storage modulus of enzyme-added dispersions was also contributed to by higher solid concentration contained in the enzyme preparation. The higher enzyme concentration led to a higher crosslinking reaction rate as shown by tremendously increasing storage modulus during incubation at 40 ^{o}C. At the end of the incubation time, dispersions with lower enzyme concentrations showed slightly reduced storage modulus, indicating water immobilisation that prevent the water-soluble enzyme from accessing protein substrates at other reaction sites (Akinori Mizuno et al., 2000; Tang et al., 2006a). Unlike the effects of calcium ions, the presence of MTGase enzyme did not the alter spatial structures of insoluble protein particles which means protein concentrations involved within the network structures is unlikely to change. Therefore, increasing modulus of dispersions could be attributed to newly formed covalent bonds within particle and between particles that strengthen intra-particle structures and inter-particle interactions leading to formation of solidified gel. Temperature quenching led to storage modulus increase of all samples with some slope variations. Dispersion with highest enzyme concentration showed the least steep modulus increase which reveals a more thermally stable gel structure due to covalent bond formation by protein crosslinking reactions. At the end of temperature quenching, dispersion with higher enzyme concentration led to a solidified gel with the highest elastic moduli.

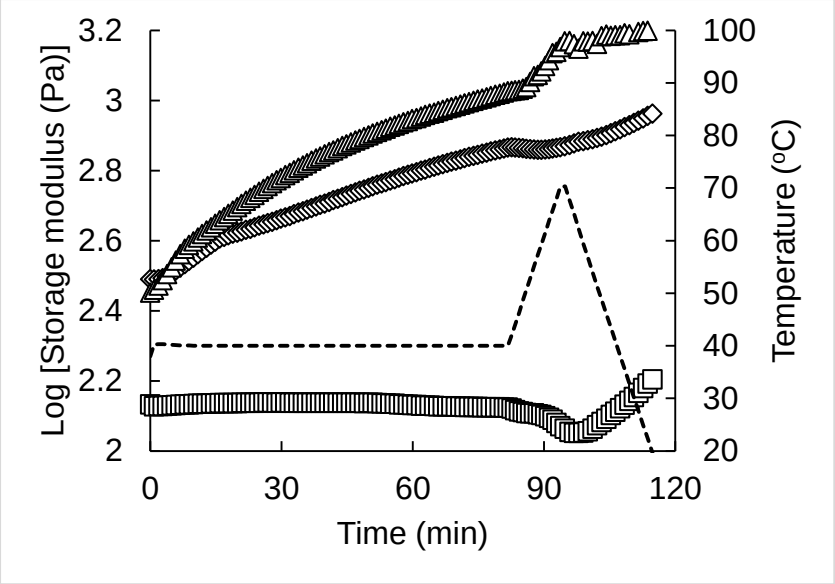

Figure 5.8 Storage modulus of 10% (w/w) Supro 760 SPI dispersions during temperature-sweep as affected by transglutaminase enzyme at different concentrations: 0 (square symbols), 10 (diamond symbols), and 20 (triangle symbols) U g^{-1} SPI. Temperature (dashed line) was programmed as follows: incubation at 40 ^{o}C for 80 min, heated to 70 ^{o}C at 2.5 ^{o}C min^{-1}, and quenched to 20 ^{o}C at 2.5 ^{o}C min^{-1}. The results are representative of duplicate experiments.

Viscoelastic properties of different SPI gels with or without addition of either $CaCl_2$ or MTGase were compared (Figure 5.9). SPI gels without either of these compounds showed the lowest moduli due to predominant contribution of non-covalent interactions. On the other hand, non-covalent interactions of $CaCl_2$-added SPI gels were intensified in the presence of calcium ions which resulted in a rigid and dense solid structure with increasing moduli. The highest moduli was achieved by MTGase-added SPI gel as favoured by newly formed covalent bonds. Interestingly, the MTGase-added SPI gel

shared a similar spatial structure with the lowest moduli in term of dispersed phase volume fraction of insoluble protein particles. This emphasised the strengthening effects of the covalently crosslinked proteins within the particle structure as well as between the closely packed particles. However, current findings differed from recent work reporting that calcium-induced gel was stiffer than the one with transglutaminase (Wang et al., 2018). This is possibly due to different SPI characteristics, such as protein solubility and their insoluble fractions. The previous study used highly soluble SPI as starting material, whereas this study focused on SPI with limited solubility hence intensifying the effects of protein crosslinking within and between the highly packed insoluble particles.

Differences in linear viscoelastic region of SPI gels were also observed. MTGase-added SPI gel exhibited the longest strain-independent elastic region compared to the other gels. Storage modulus started to decrease when amplitude strain approached circa 20% followed by gel rupture at higher strain. This might be an evidence of the presence of large fractal gel structure due to crosslinked protein particles. Furthermore, loss moduli of the gel retained strain-independency prior to gel rupture, which revealed a strong immobilisation of water within gel structure. In contrast, the other SPI gels displayed shorter linear viscoelastic region below 10% amplitude strain. The enhancing effects of MTGase on SPI gel elasticity have been confirmed in other studies (Chang et al., 2011; Hou et al., 2016; Wang et al., 2018).

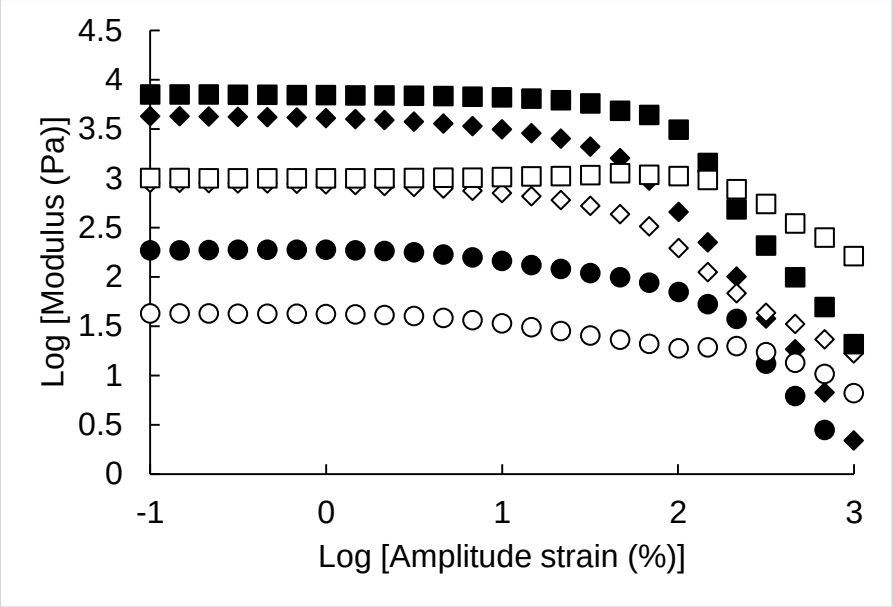

Figure 5.9 Storage (filled symbols) and loss modulus (open symbols) of solidified SPI gel as a function of amplitude strain in the absence (circle symbols) and presence of either $CaCl_2$ (diamond symbols) or MTGase (square symbols). The results are representative of duplicate experiments.

A comparison between microstructure of SPI gels as affected by $CaCl_2$ and MTGase are shown in scanning electron micrograph (Figure 5.10). $CaCl_2$-added SPI gels appeared to have a dense structure containing smaller size of holes distributed throughout the solid matrix indicating less capability to retain large amount of water. In contrast, MTGase-added SPI gel showed longer solid network with larger size empty spaces between matrices demonstrating water retaining-ability within the structure.

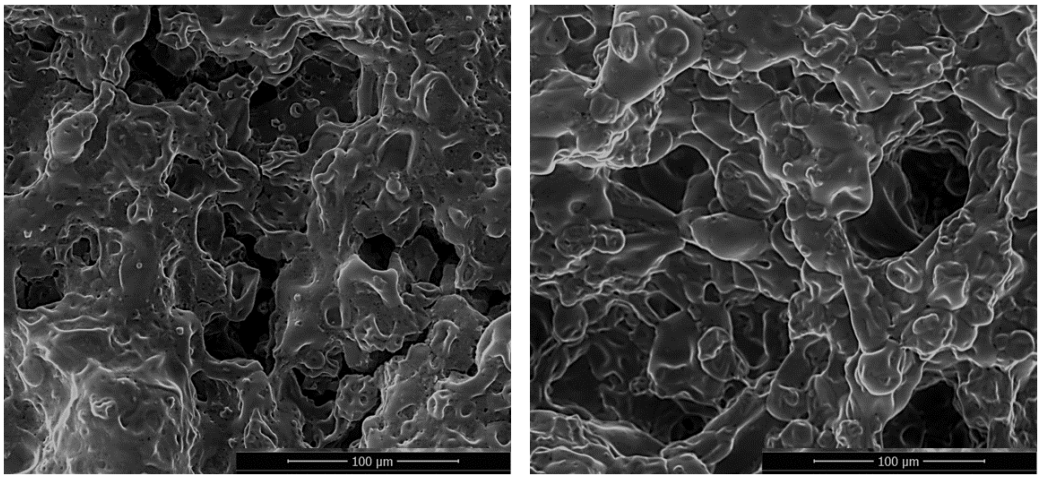

Figure 5.10 Environmental scanning electron microscopy images of SPI gels with addition of $CaCl_2$ (left) and TGase (right). Scale bar shows 100 µm.

Structural differences of SPI gels at molecular level were evaluated using FTIR spectroscopy as shown in Figure 5.11. The presence of calcium ions within SPI gel shifted the position of amide I and II' peaks to lower wavenumbers, i.e. from ~1631 and ~1444 to ~1623 and ~1436 cm^{-1}. Peak shifting of amide I indicated some interactions between the calcium ions and carboxyl groups which led to backbone conformational changes and hence followed by shifting of the other amide vibrations (Arii and Takenaka, 2014; Zhang et al., 2012). However, FTIR spectra of MTGase-added SPI gel did not show considerable changes on carbonyl stretching at amide I peak. MTGase-induced protein crosslinking has been reported to predominantly affect hydrophobic interactions involving aliphatic side chains rather than new bonds formation around the protein backbone environment (Eissa et al., 2006; Gaspar and de Góes-Favoni, 2015).

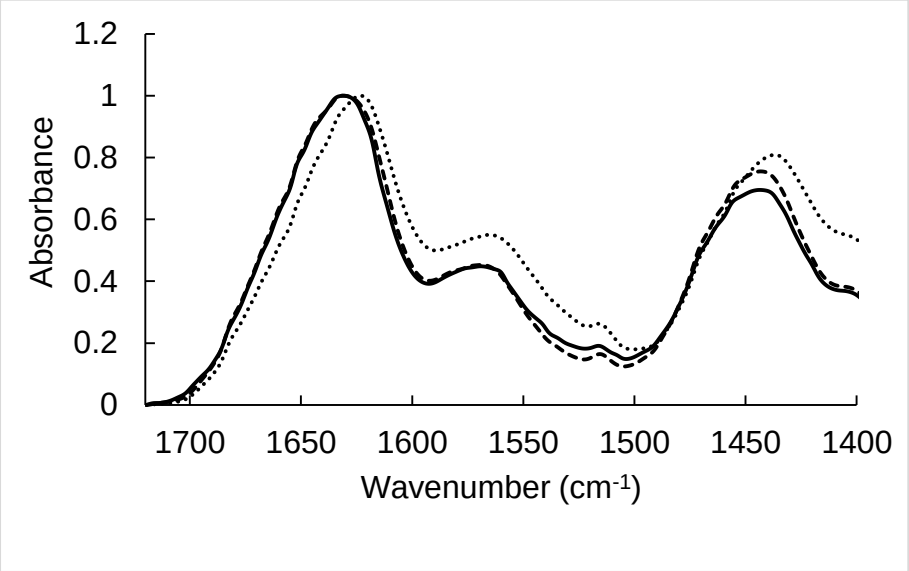

Figure 5.11 FTIR spectra of solidified SPI gel in the absence (solid line) and presence of either $CaCl_2$ (dotted line) or MTGase (dashed line). The results are representative of duplicate experiments.

5.4 Conclusions

Heat-induced solidification of SPI with limited solubility required addition of either $CaCl_2$ or MTGase enzyme which resulted in different characteristics of SPI gels. The presence of calcium ions altered the spatial structure of SPI dispersion leading to formation of a denser gel matrices that was attributed to protein conformational changes at molecular level. In contrast, MTGase-added SPI gel preserved water holding ability of initial spatial structure with increased dynamic moduli due to strengthening of intra and interparticle network as favoured by newly formed covalent linkages. The presented work

provides useful insight on utilisation of insoluble SPI for solid gel structure formation.

6 Physicochemical characterisation of oat bran protein-rich material and its modification by ball milling

6.1 Introduction

Oat bran is a by-product from oat flour milling that is abundant in both fibre and protein content. However, full utilisation oat bran protein remains challenging due to limitation in protein extraction and solubility. Enzymatic pre-treatment of oat bran is necessary to assist protein extraction by degrading thick cell walls, otherwise a highly alkaline pH is required to release protein that adversely affect the nutritional quality (Guan and Yao, 2008; Jodayree et al., 2012; Liu et al., 2008). Furthermore, low solubility of oat protein in slightly acidic to neutral pH range also restrict its applicability in foods (Konak et al., 2014). In order to bridge the gap between the limitations and advantages of oat bran protein for utilisation in foods, a feasible separation technique has been introduced to obtain protein concentrate with low degree of purity (Sozer et al., 2017).

Many previous studies on oat bran protein focused on extraction and functional properties of high purity protein, such as concentrates and isolates (Guan et al., 2007; Guan and Yao, 2008; Jodayree et al., 2012; Liu et al., 2008). There are limited references elaborating on the characteristics of low purity oat protein concentrate, hence this can be of interest. The retained starch, lipid, and fibre in a protein-rich material is expected to contribute to the functional properties but may require modification (Sozer et al., 2017).

Physical modification of food materials by means of ball milling has gained attention due to ability in changing functionality. The modified functionality can be attributed to alteration in structural conformation as found in starchy food materials (Dhital et al., 2011; Liu et al., 2011; Roa et al., 2014a). However, there are limited studies reporting the effects of ball milling on structural conformation changes in food proteins (Liu et al., 2017; Sun et al., 2015). This present study aims to evaluate the effects of ball milling on structural and physicochemical properties of oat bran protein-rich material. This study would provide useful insights to extend the utilisation of oat bran protein in food formulations.

6.2 Experimental

Physical characterisation of oat bran protein-rich material (OBP) involved visual examination and microscopic observation of OBP dispersions. Preparation of OBP dispersion began with dispersing dry OBP powder in distilled water at 10, 15, 20, 25, and 30% (w/w) concentrations, followed by stirring for at least 30 min at ambient temperature. The dispersions were transferred into 7 ml vials, settled for 30 min, then visually observed to obtain information regarding physical stability of OBP dispersion. Subsequently, the dispersion was diluted to 0.1% concentration and subjected to observation under light microscope.

Structural properties of OBP were resolved by means of FTIR spectroscopy and micro-DSC analysis. Since OBP contained considerable amount of lipid and carbohydrate, elimination of both components was conducted to obtain OBP fractions with higher protein concentration. OBP was subjected to lipid

elimination by using either hexane or isopropanol as non-polar and polar solvents respectively. Lipid elimination were carried out in soxhlet apparatus as described by Pandey and Shrivastava (2018) with modifications. The resulting fractions are denoted as non-polar solvent-defatted OBP (NPDO) and polar solvent-defatted OBP (PDO). The attempts to extract protein from OBP did not lead to reasonable protein yields for further analysis. Therefore, elimination of carbohydrate was conducted to obtain OBP with higher protein concentration by dispersing and stirring the PDO into alkaline solution for 30 min as described by De Souza et al. (2016). The dispersion was then centrifuged followed by collection of sediment. The collected fraction was frozen and lyophilised to obtain dry powder. This carbohydrate-eliminated fraction is denoted as APDO. OBP and its derived fractions in powder form were subjected to FTIR spectroscopy, whereas OBP dispersions at 20% (w/w) concentration were analysed using micro-DSC. Comparison between signals from measured samples was used to confirm the assignment of OBP chemical constituents.

Useful information can be obtained from FTIR spectra with appropriate assignment and data processing for absorption bands of interest. Absorption bands of protein was assigned according to the established literatures (Barth, 2007; Jing et al., 2016). Considering protein as predominant constituent, the amide I band of protein was used as reference band. Intensity ratio between band of interest and reference was calculated to evaluate the differences between OBP and its derived fractions, hence the absorption band assignment for lipid and carbohydrate can be confirmed.

The assigned band can be used to elucidate the structural information of chemical constituents.

Modification of OBP was carried out by ball milling in Planetary Micro Mill (Pulverisette 7 classic line, FritschGmbH, Germany) as described by Abbaszadeh et. al. (2014) with modified procedure. Two and a half grams of dry OBP powder was put into 12 ml grinding bowl containing 6 Zirconium dioxide grinding balls. High speed milling was run at 800 revolutions per minute (rpm) for 30 min and denoted as HSST, whereas low speed milling was carried out at 200 rpm for 360 min and denoted as LSLT. The applied milling cycle configuration was 5 min milling followed by 5 min rest to dissipate heat. Reversed milling directions were set to prevent ball slippage at both milling speeds. Effects of ball milling on structural properties were evaluated using FTIR spectroscopy and micro-DSC, whereas effects on physical structure of OBP dispersions was evaluated by means of temperature sweep oscillatory rheology test. Solid concentration of the evaluated dispersions was 30% (w/w) which exhibited a more stable dispersion.

6.3 Results and discussion

6.3.1 Characterisation of OBP dispersion

When dispersed in water, OBP showed a characteristic of suspension due to sedimentation of insoluble particulates as shown in Figure 6.1. Higher OBP concentrations led to an increased height of sediment fraction and the more turbid supernatant fraction due to higher dispersed phase volume fraction.

Thin opaque layer between sediment and supernatant fractions indicated that larger and heavier particulates were sedimented at the lower part of sediment, whereas the smaller and lighter particulates formed the upper layer of sediment. This is confirmed by microscopic observation showing granular particles with in various irregular shapes and sizes, that can be differentiated into two groups, i.e. larger-darker, and smaller-brighter particles. OBP dispersion with higher solid concentration, i.e. above 25% (w/w), exhibited concentrated dispersion without visually noticeable phase separation. This observation confirmed poor solubility of OBP when dispersed in water that may be attributed to exposure to high temperature during preparation processes.

(a)

(b)

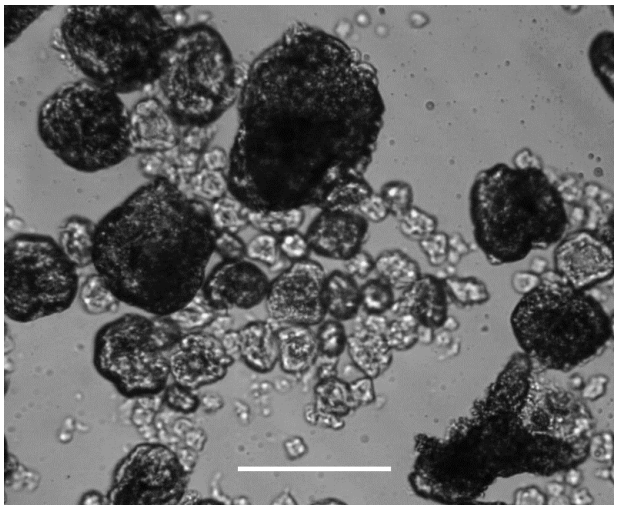

Figure 6.1 OBP dispersions at 10, 15, 20, 25, and 30% (w/w) concentration after settling for 5 min (a); Microscopic image of OBP dispersion at 0.1% (w/w) observed under light microscope (b).

6.3.2 Structural properties of OBP chemical constituents

FTIR spectra of dry OBP sample showed typical absorption bands of various functional groups that belong to protein, lipid, and carbohydrate, e.g. at the wavenumber ~3270, ~2920, ~2855, ~1745, ~1630, ~1520, ~1150, ~1080, and ~1020 cm^{-1} (Figure 6.2). Absorption bands of protein, as the predominant chemical constituent, appeared as two consecutive signals at wavenumbers ~1630 and ~1520 cm^{-1} known as amide I and II. The bands are predominantly induced by C=O and C-N stretching vibrations. In addition, N-H stretching vibrations of proteins may also contributed to the broad

absorption band at ~3270 cm^{-1} that highly dependent on the strength of hydrogen bonds (Barth, 2007; Miller and Fulcher, 2011).

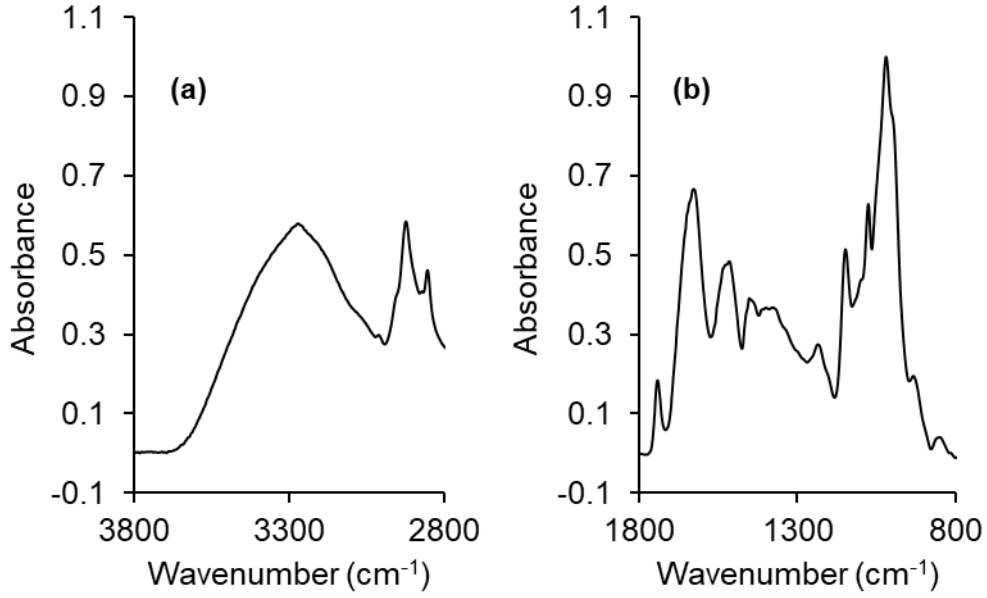

Figure 6.2 FTIR spectra of OBP from selected wavenumber regions: (a) 3800-2800 and (b) 1800-800 cm^{-1}.

Band intensity ratio of OBP and its derived fractions are shown in Table 6.1. Elimination of neutral lipids by non-polar solvent drastically decreased the absorption signal at ~2920, ~2855, and ~1745 cm^{-1}. However, the use of polar solvent diminished the second peaks and left small signal of the third peak. This might indicate the asymmetric stretching vibrations of C-H at ~2920 cm^{-1} is not solely contributed by of lipid alone, but also from other major chemical constituents. The peak at ~2855 cm^{-1} could be uniquely assigned to -CH_2- symmetric stretching of fatty acid chains. The peak ~1745 cm−1 corresponds to carbonyl (C=O) stretching vibration identifying the ester

functional group of lipid (Cerqueira et al., 2012). Oats contain higher amounts of polar lipids compared to other cereals, such as glycolipids and monoacyl lipids (Doehlert et al., 2010).

Saccharide region of infrared spectra ranges from 1200 to 900 cm^{-1}. The intensity ratio of three absorption bands at ~1150, ~1080, and ~1020 cm^{-1} increased after lipid elimination. The bands can be attributed to typical vibration characteristics of C-O, C-C, O-H bonds and asymmetric stretching of C-O-C glycosidic bonds within the starch. The strongest absorption band at ~1020 cm^{-1} indicated predominant disordered conformational structure of OBP starch that have gone through thermal treatment during production. This peak contains shoulder at the lower wavenumber that possibly indicate small amount of ordered conformation (Liu et al., 2011; Roa et al., 2014b). Alkaline exposure treatment dramatically decreased absorbance intensity of the three above mentioned peaks, indicating irreversible solubilisation of starch. This confirmed the correct assignment for starch within infrared spectra.

Table 6.1 Intensity ratio of OBP and its derived fractions at peaks of interest.

Sample	Band intensity ratio relative to peak at ~1630 cm^{-1}					
	~2924 cm^{-1}	~2854 cm^{-1}	~1745 cm^{-1}	~1150 cm^{-1}	~1078 cm^{-1}	~1022 cm^{-1}
OBP	0.55 ± 0.04	0.11 ± 0.02	0.32 ± 0.02	0.67 ± 0.05	0.49 ± 0.06	0.94 ± 0.14
HDO	0.31 ± 0.02	0.02 ± 0.00	0.16 ± 0.08	0.69 ± 0.06	0.53 ± 0.06	0.92 ± 0.03
PDO	0.29 ± 0.01	N/A	0.08 ± 0.01	0.79 ± 0.08	0.54 ± 0.08	1.02 ± 0.15
APDO	0.21 ± 0.02	N/A	0.05 ± 0.01	0.48 ± 0.06	0.37 ± 0.04	0.61 ± 0.12

For abbreviations see experimental section.

The DSC thermograms and the corresponding thermal transition peak temperature and enthalpy changes of OBP dispersions are presented in Figure 6.3 and Table 6.2, respectively. Upon the first heating, a broad endothermic peak appeared at c.a. 90 °C and consequently shifted to a higher temperature when reheated. Whereas upon cooling, a sharp exothermic peak was observed at c.a. 74 °C in either cycles. The ΔH value was 1.7 J g^{-1} on the first heating and subsequently decreased over the following cycles. The use of polar solvent greatly reduced ΔH values due to elimination of higher amounts of lipids as confirmed by FTIR study. However, scanning calorimetry of extracted lipids did not show any thermal transition events (data not shown). Carbohydrate elimination, particularly starch, by alkaline exposure further decreased the ΔH values. It shows that the ΔH values are more dependent to starch and lipid rather than protein. The absence of thermal events associated to protein is might be due to the presence of thermally-stable aggregated protein.

The reversible thermal events at very high temperature upon heating, i.e. 90 ^{o}C, can be associated to the characteristics of complexes between lipid, starch, and possibly protein. Starch-lipid complexes in the presence of protein as a result of thermal processing have been found in previous studies (De Pilli et al., 2015; Moisio et al., 2015; Wang et al., 2017). When the heated starch is cooled back in the presence of lipid, the amylose formed complexes with lipids by the inclusion of fatty acid chain into helical cavity (Tufvesson et al., 2003). The amount of amylose-lipid complexes is the major factor determining the ΔH value as proposed by Kawai et al. (2012). Interestingly, melting temperature of starch-lipid complexes slightly increased

upon second heating hence indicating a more thermally stable structure as a result of complexes reformation in more ordered structure.

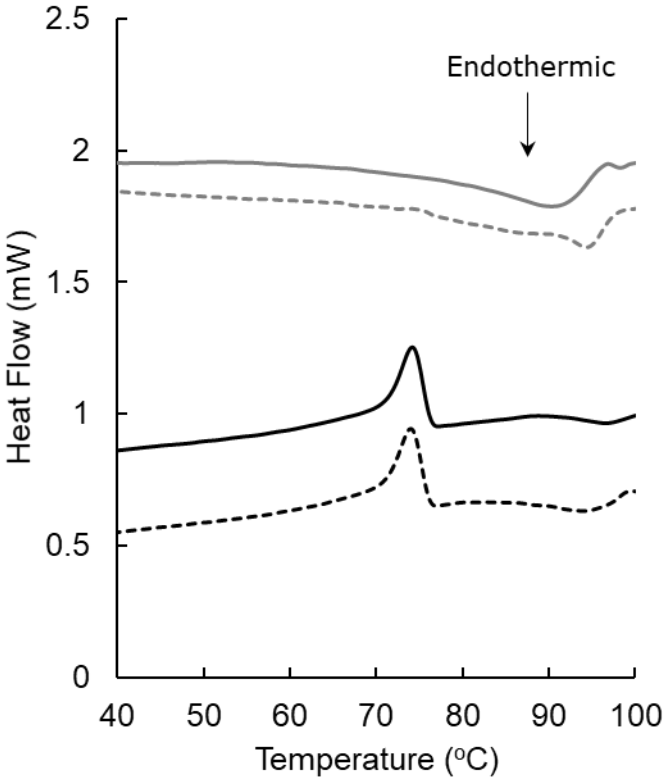

Figure 6.3 Micro-DSC thermogram of OBP dispersion obtained from two heating-cooling cycles at the rate of 1 ^{o}C min^{-1}.

Table 6.2 Thermal transition peak temperatures (T_p) and enthalpy changes (ΔH) of OBP dispersions and its derived fractions.

Sample	First heating		First cooling		Second heating		Second cooling	
	T_p (^oC)	ΔH (J g^{-1} solid)	T_p (^oC)	ΔH (J g^{-1} solid)	T_p (^oC)	ΔH (J g^{-1} solid)	T_p (^oC)	ΔH (J g^{-1} solid)
OBP	90.63 ± 0.32	1.70 ± 0.21	74.14 ± 0.04	-1.02 ± 0.04	94.42 ± 0.10	1.01 ± 0.02	73.97 ± 0.04	-0.94 ± 0.02
NPDO	91.12 ± 0.74	0.94 ± 0.18	74.49 ± 0.05	-0.84 ± 0.02	94.98 ± 0.08	0.72 ± 0.13	74.34 ± 0.03	-0.72 ± 0.07
PDO	90.41 ± 0.59	0.76 ± 0.02	73.80 ± 0.25	-0.64 ± 0.04	94.07 ± 0.16	0.61 ± 0.04	73.73 ± 0.25	-0.53 ± 0.08
APDO	92.07 ± 0.51	0.48 ± 0.01	72.28 ± 0.41	-0.32 ± 0.02	92.76 ± 0.16	0.26 ± 0.02	71.88 ± 0.61	-0.26 ± 0.05

For abbreviations see experimental section.

6.3.3 Structural properties of ball milled OBP

Ball milling affected structural conformation changes on both protein and starch in solid-state as illustrated in Figure 6.4 and Table 6.3. Prior to ball milling, secondary structure of protein prominently presented as β-sheets structure and some minor helical structures. This result demonstrated a higher composition in β-sheets compared to previous study on oat protein isolate secondary structure at low moisture (Liu et al., 2009). The explanation for this condition is the protein contained in OBP has been thermally treated during the production, hence most likely in denatured and aggregated form. The β-sheet structures have been associated with hydrophobic and aggregated protein (Maltais et al., 2008; Tang and Ma, 2009; Wellner et al., 2005). However, other study on oat protein conformation in aqueous dispersion showed lower relative amount of β-sheets as the major structure (Jing et al., 2016). Secondary structure of protein in dispersion is a result from peptide-solvent interactions in aqueous environment, whereas at low moisture the peptide-peptide interactions are predominant factor due to dense packing in a solid environment.

Ball milling gradually increased relative amounts of helical conformations in expense of β-sheet structures. Longer ball milling time, regardless the applied speed, demonstrated greater effect on protein conformational changes due to simultaneous mechanical impact. Similar result of increasing α -helix and decreasing β-sheet structure after ball milling soy protein isolate has been reported (Liu et al., 2017). Ball milling involves high pressure, shear force, and air contact that might cause rearrangement of aggregated

protein secondary structure as suggested by Sun et al. (2015). Among the protein fractions and sub-units, low molecular weight proteins are the most susceptible to disruptions caused by ball milling (Thanatuksorn et al., 2009).

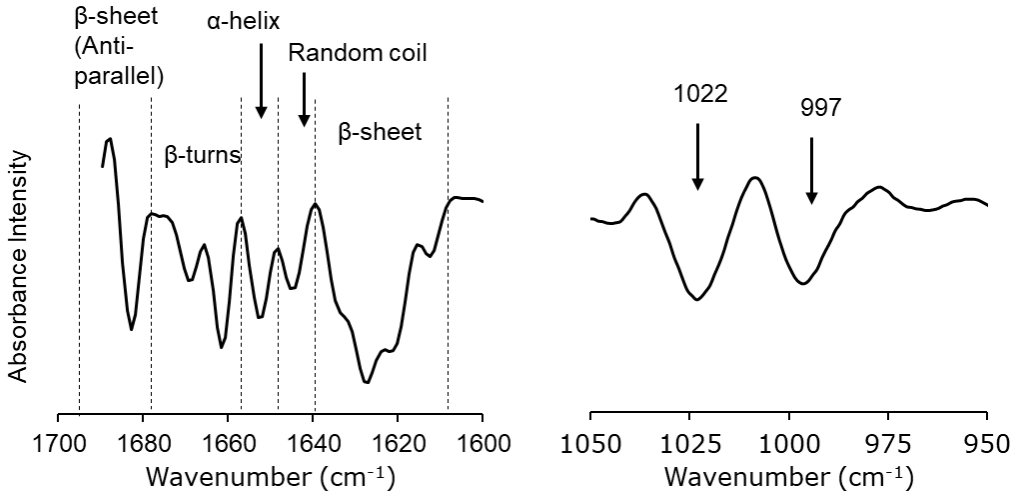

Figure 6.4 Second derivative spectra of OBP at amide I and saccharide bands

Evaluation of ball milling effects on starch conformation are presented in the Table 6.3. A higher ratio of peak ~997 to ~1022 indicated small degree of ordered structure within starch conformation. The presence of amylose-lipid complexes has been reported to consists of some starch crystalline order (Kawai et al., 2012). In this study, lower speed milling with longer duration greatly reduced the starch's ordered structure compared to short time high speed milling. This ball milling effects on starch has been extensively studied

in previous reports known by disruption effects on starch helical structures (Liu et al., 2011; Roa et al., 2015).

Table 6.3 Ball milling effects on protein and starch structural conformation of dry OBP samples estimated from FTIR spectroscopy data

Sample	Abundant of protein secondary structure (%)		Starch
	Total β-sheets and β-turns	Total α-helix and random coil	~997/~1022 cm^{-1} ratio
OBP	88.03 ± 2.69	11.97 ± 2.69	0.63 ± 0.02
HSST	79.85 ± 0.61	20.15 ± 0.61	0.50 ± 0.02
LSLT	80.33 ± 6.95	19.67 ± 6.95	0.38 ± 0.04

For abbreviations see experimental section.

Thermal properties of OBP prior to and after ball milling are presented in Table 6.4. Ball milling did not greatly affect the transition peak temperature, whereas the enthalpy values gradually decreased as the milling time increased, regardless the applied speed. Decreasing enthalpy values can be interpreted as the decrease on amounts of amylose-lipid complexes within OBP. This is confirmed by further loss of crystallinity provided by FTIR spectroscopy study. Simultaneous mechanical impact during ball milling disrupted the helical structure of amylose, hence disintegrated the amylose-lipid complexes. Ball milled samples did not differ in transition temperature

peak upon the second heating showing thermal behaviour remain unchanged.

Table 6.4 Thermal transition peak temperatures (T_p) and enthalpy changes (ΔH) of OBP dispersions affected by ball milling.

Sample	First heating		First cooling		Second heating		Second cooling	
	T_p (^oC)	ΔH (J g^{-1} solid)	T_p (^oC)	ΔH (J g^{-1} solid)	T_p (^oC)	ΔH (J g^{-1} solid)	T_p (^oC)	ΔH (J g^{-1} solid)
OBP	90.63 ± 0.32	1.70 ± 0.21	74.14 ± 0.04	-1.02 ± 0.04	94.42 ± 0.10	1.01 ± 0.02	73.97 ± 0.04	-0.94 ± 0.02
HSST	90.50 ± 0.26	1.19 ± 0.14	73.72 ± 0.09	-0.78 ± 0.07	94.10 ± 0.01	0.65 ± 0.12	73.63 ± 0.10	-0.51 ± 0.01
LSLT	91.20 ± 0.34	0.85 ± 0.07	74.04 ± 0.09	-0.77 ± 0.07	94.52 ± 0.07	0.66 ± 0.10	73.96 ± 0.07	-0.60 ± 0.04

For abbreviations see experimental section.

6.3.4 Particle size distribution of ball milled OBP

Particle size distributions of OBP prior to and after ball milling are presented in Figure 6.5. As expected, ball milling reduced the size distribution towards smaller particle sizes. High speed milling at a shorter duration resulted to a more severe particle breakage, whereas simultaneous milling at lower speed up to 6 hours caused a less intense particle size reduction. According to Yin et al. (2015), particle size reduction caused by ball milling depends on several parameters, such as the size of grinding balls, milling speed, and filling ratio, that can be described into stress intensity. In this study, differences in milling speed can be regarded as the main contribution to stress intensity.

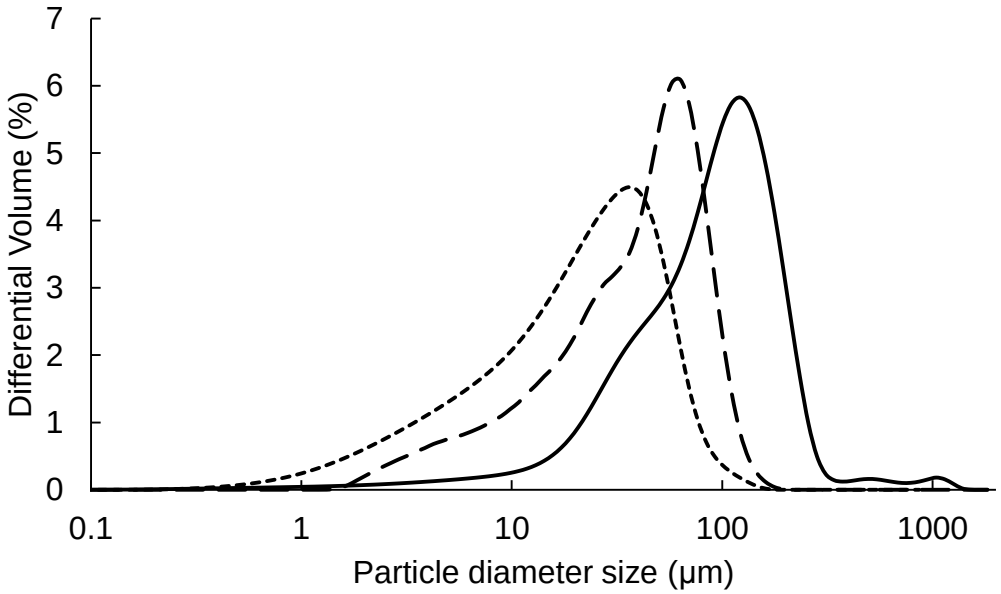

Figure 6.5 Particle size distribution of OBP (solid line), HSST (dashed line), and LTST (long dashed line)

6.3.5 Heat-induced structure formation of concentrated OBP dispersion

Mechanical properties of 30% (w/w) OBP dispersion were evaluated using oscillatory shear rheology test. Storage modulus of dispersions as affected by heating and cooling are illustrated in Figure 6.6. All samples exhibited elastic-dominant behaviour therefore the presented data focus on storage modulus changes. Prior to heating, storage modulus of dispersion is contributed by the volume-occupying particles at various sizes. Dispersions containing ball milled samples exhibited lower storage modulus due to lower dispersed phase volume fraction of smaller particles. This finding agreed the previous studies on particle size effect on storage modulus of dispersion (Moreira et al., 2010; Sendra et al., 2010). Temperature dependency of storage modulus were recorded upon heating and cooling all dispersions. Heating up to 40 °C led to a slight modulus decrease that can be attributed to the effects of increasing particle mobility since there were no thermal events recorded by scanning calorimetry within this temperature range. Further modulus decrease took place when temperature approach 90 °C that might be related to melting behaviour of starch-lipid complexes within OBP as found in micro-DSC data and leading to particle softening. Subsequently, decreasing temperature of dispersion induced stiffening as favoured by starch recrystallisation, decreasing particle motions, and strengthening of hydrogen bonds. Moreover, quenched dispersions reached higher storage modulus compared to their initial values prior to heating in which might indicate the formation of structure and connectivity between particles.

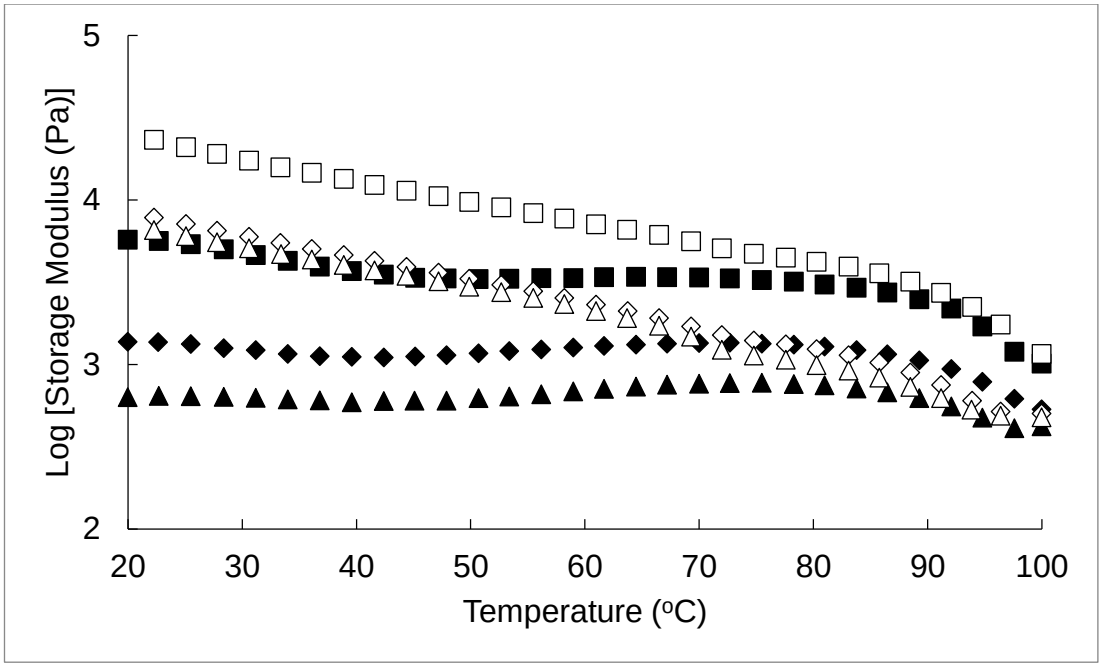

Figure 6.6 Storage modulus of 30% (w/w) OBP dispersions upon heating (filled symbols) and cooling (open symbols) at 5 ^{o}C min^{-1} heating and cooling rate. OBP, HSST, and LSLT are depicted as square, triangle, and diamond symbols respectively.

The effects of heating-cooling treatment on the structure of dispersion were also evaluated by amplitude strain sweep tests as presented in the Figure 6.7. Heated dispersion was higher in both storage and loss modulus indicating a more rigid structure. Linear-viscoelastic region of heated dispersion was slightly longer than unheated sample and followed by an extended non-linear transition prior to crossover point indicating inter-particle connectivity within the concentrated dispersion.

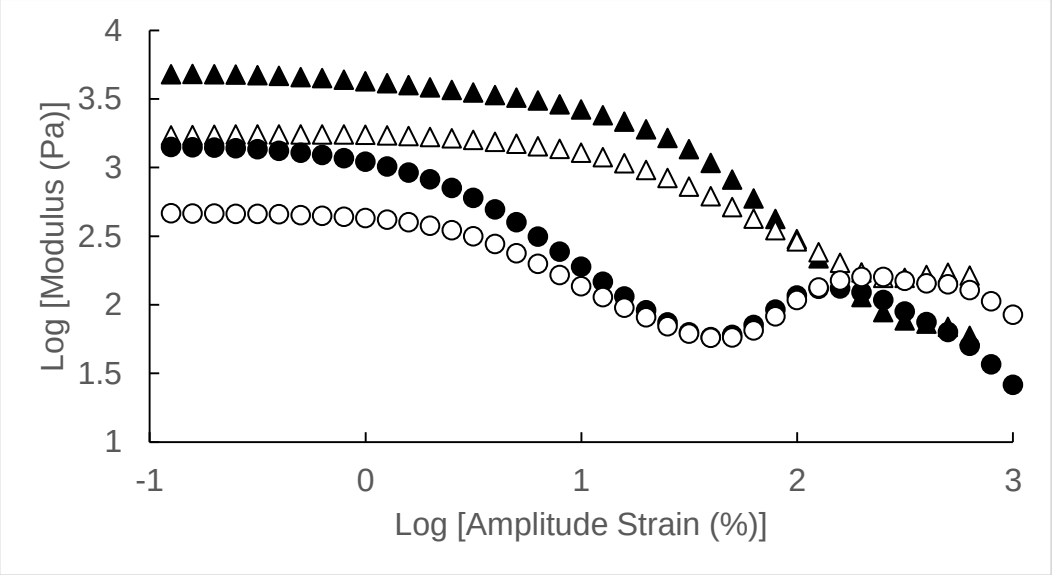

Figure 6.7 Storage (filled symbols) and loss (open symbols) modulus of OBP dispersions at 30% (w/w) concentration prior to (circle symbols) and after (triangle symbols) temperature cycle as a function of amplitude strain.

Frequency dependency of heated OBP dispersions were evaluated within linear viscoelastic region as shown in Figure 6.8. Both storage and loss modulus of all samples increased with increasing angular frequency. At high frequency regime, a more intensive friction between particles took place within concentrated dispersion that led to an increased modulus. Domination of storage modulus over the loss modulus were observed within the tested frequency indicating a typical behaviour of particle suspension. Either storage or loss modulus curves of each sample showed generally similar curve patterns indicating similarity in behaviour. However, dispersions containing smaller particles as affected by ball milling exhibited lower modulus due to lower volume packing of particles.

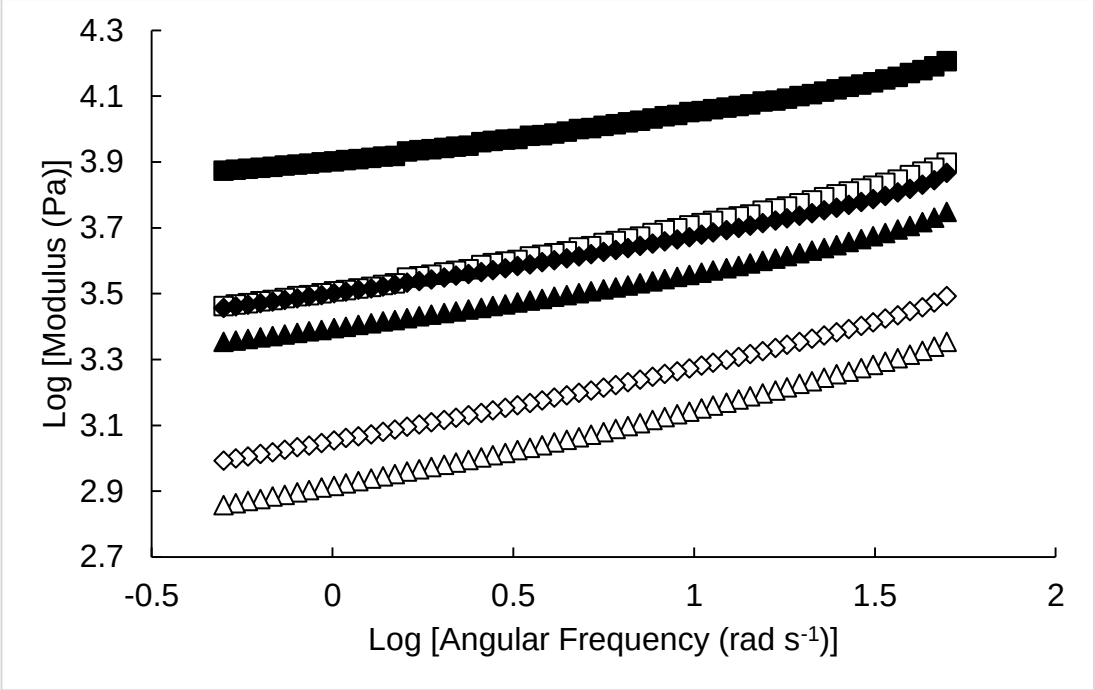

Figure 6.8 Storage (filled symbols) and loss (open symbols) modulus of heated OBP dispersions at 30% (w/w) concentration as a function of angular frequency. OBP, HSST, and LSLT are depicted as square, triangle, and diamond symbols respectively.

6.4 Conclusions

Characterisation of oat bran protein-rich material showed the presence of lipid and carbohydrate in complexes form. Ball milling altered the structural conformations of protein and starch. Higher speed ball milling reduced particle size distributions, led to lower particle volume packing, hence decreased the modulus of dispersions. Subsequent heating-cooling processes of dispersions allowed the starch to build a stiffer networked structure.

7 Modulating the structure of gels containing protein mixtures of soy and oat bran

7.1 Introduction

Plant-based protein is considered as alternative sustainable protein source. Increasing utilisation of plant-based protein in foods have been a current research interest. In high protein foods, the ability of protein to form three-dimensional gel network is an important contributing factor to the food structure. Among the plant proteins, soybean is the most readily available and widely used plant protein with a well-known gelation ability (Nishinari et al., 2014). Protein from other plants have also been reported to exhibit gelation ability, such as amaranth (Avanza et al., 2005), canola (Yang et al., 2014), cottonseed (Zhou et al., 2015), lupin (Berghout et al., 2015), and peas (Shand et al., 2007).

Consumption of combined plant proteins from different sources has been suggested to overcome the limitation on amino acid profile of protein from single plant source (Gorissen et al., 2018). In addition to nutritional properties, mixtures of different plant proteins cause differences in food physical structure. Recent studies of soy protein-wheat gluten blends showed compatibility of the mixture in forming meat-like fibrous structures (Grabowska et al., 2014; Krintiras et al., 2015).

Cereal bran protein concentrate at low purity is thought to be more sustainable to be used in food application (Schutyser and van der Goot, 2011; Sozer et al., 2017). Structure formation of low purity oat bran protein

concentrate induced by heating has been discussed in the previous chapter. Therefore, this study aims to elaborate the structure of protein gels prepared from mixtures of soy protein isolate and low purity oat bran protein concentrate. The structural evaluation focuses on gel stiffness and deformability measured using amplitude strain sweep test oscillatory rheology. The result of this study would provide insight on utilisation of mixed plant proteins for the application of solid protein-rich foods.

7.2 Experimental

The main materials used in this study were Supro® 760 IP soy protein isolate (SPI) and PrOatein® oat bran protein concentrate (OBP). Protein-blend dispersions were prepared by dispersing SPI and OBP in $CaCl_2$ solution. The tested concentrations were varied as described in

Table 7.1 and final concentration of $CaCl_2$ was 50 mM. Solid mass fraction was calculated by dividing the weight of either SPI or OBP by total weight of solid materials. In the latter part of this work, microbial transglutaminase (MTGase) enzyme was added to the protein-blend dispersions containing 13% (w/w) SPI. The required final enzyme concentration was 20 U g^{-1} solid material.

Table 7.1 Concentration of SPI and OBP used in mixed protein gel

SPI concentration (%w/w)	SPI solid mass fraction (%w/w)	OBP concentration (%w/w)	OBP solid mass fraction (%w/w)	Total solid concentration (%w/w)
11	100	0	0	11
11	84.6	2	15.4	13
11	73.3	4	26.7	15
11	64.7	6	35.3	17
11	57.9	8	42.1	19
13	100	0	0	13
13	86.7	2	13.3	15
13	76.5	4	23.5	17
13	68.4	6	31.6	19
13	61.9	8	38.1	21
15	100	0	0	15
15	88.3	2	11.8	17
15	79.0	4	21.1	19
15	71.4	6	28.6	21
15	65.2	8	34.8	23

Sample dispersions were transferred into serrated parallel plate at 1 mm gap on a rheometer (Physica MCR 301, Anton Paar, Austria). The rheometer was operated using Rheoplus software version 3.40 (Anton Paar Germany GmbH). Solidification of dispersion into gel was conducted in-situ by applying heating-cooling scenarios without any shear. Low viscosity mineral oil and peltier-controlled hood were used to prevent drying. The gel was

subsequentially subjected to oscillatory amplitude strain sweep test at 20 ^{o}C using angular frequency of 50 rad s^{-1}. Each measurement was run in duplicate. Critical strain was determined using Rheoplus software remarking the end-boundary of linear viscoelastic region when the modulus deviated 5% from its value at initial strain. Normalisation of storage modulus were calculated by dividing the storage modulus at particular strain by the modulus at initial strain.

7.3 Results and discussion

7.3.1 Effect of solid concentration on gel stiffness and deformability

Stiffness of protein gels containing mixture SPI and OBP blend at different ratios were evaluated using log storage modulus data, as illustrated in Figure 7.1. Increasing concentrations of either SPI or OBP led to a higher gel stiffness. At constant SPI concentration, OBP addition caused a more rigid gel structure. In this study, SPI acted as dominant phase and OBP is considered as active gel filler due to increased stiffness as affected by reinforcing the SPI gel matrix (Yang et al., 2013).

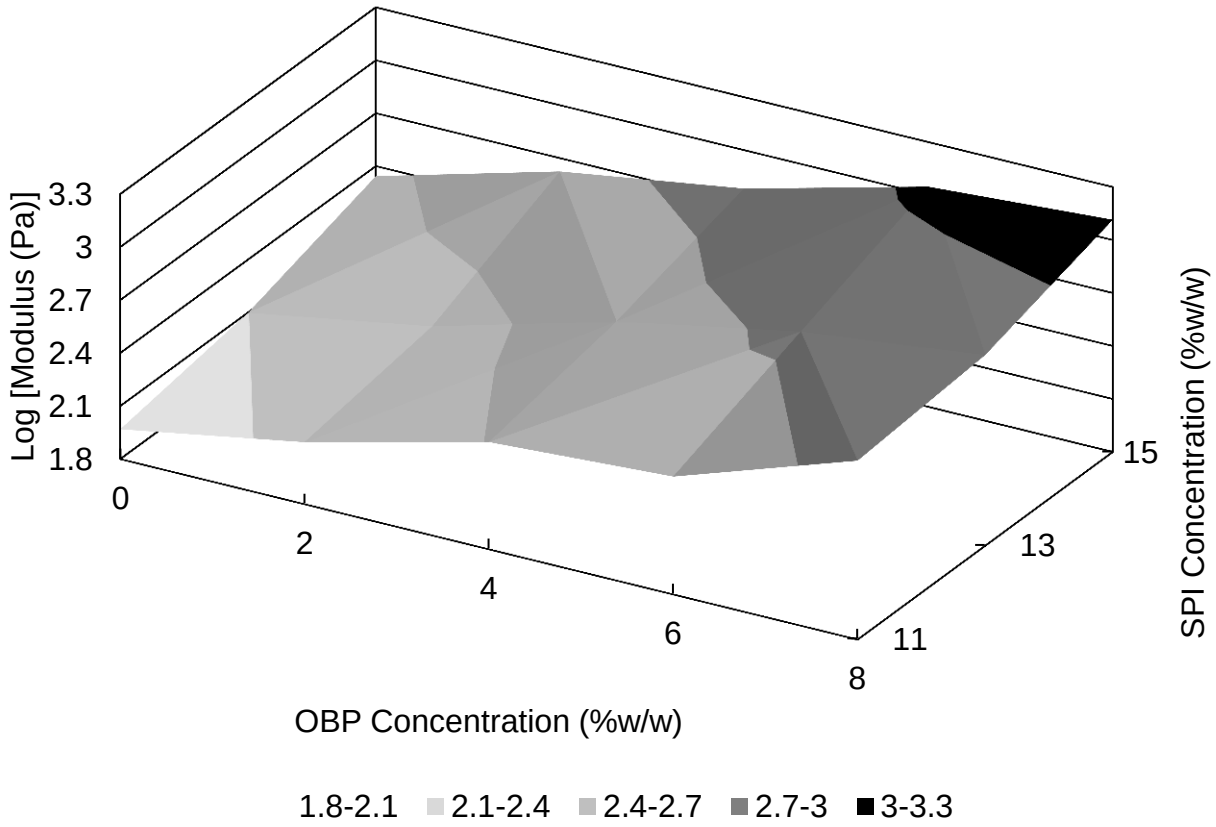

Figure 7.1 Three-dimensional surface plot of log storage modulus of mixed protein gels. The results are the average of duplicate experiments.

Increasing protein gel stiffness is also related to a higher total solid concentration as shown in Figure 7.2. Interestingly, log storage modulus at the same total solid concentration up to 19%w/w seems to be similar. This might indicate the reinforcement effect is minor due to less dense protein matrix at these concentrations. However, log storage modulus of a gel at 21%w/w total solid concentration showed a significant difference between two protein gels, i.e. SPI and OBP concentration of 15%-6%, and 13%-8%, with the former exhibited higher gel stiffness. Linearly increasing storage modulus, as affected by higher solid concentration, indicated the phase volume fraction of dispersion was below their random close packing.

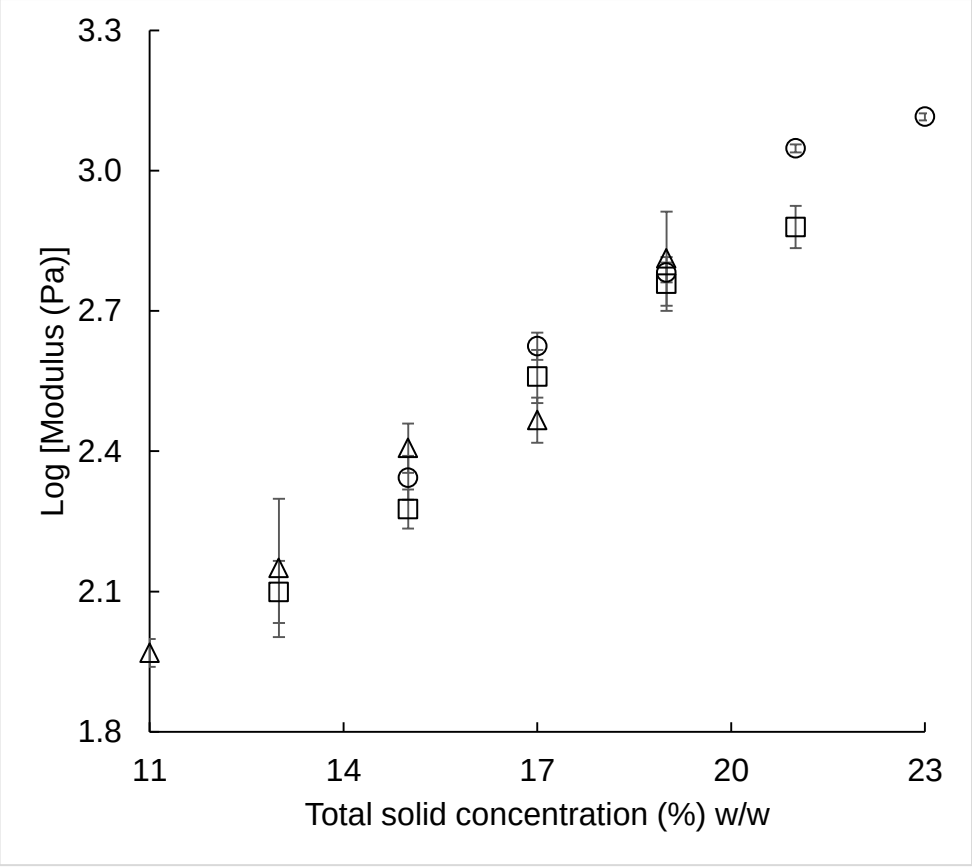

Figure 7.2 Logarithmic plot of storage modulus of protein gels at various total solid concentrations. Triangle, square, and circle symbols represent gels

containing SPI at 11, 13, and 15 %w/w concentrations respectively. Bars are standard deviations. The results are the average of duplicate experiments.

Deformability of protein gels were evaluated by critical strain data as shown in Figure 7.3. Protein gels containing lower SPI concentrations exhibited shorter linear viscoelastic range as indicated by low critical strain. This reflects a brittle gel structure that is more prone to deformation. Increasing OBP concentration within protein gels further decreased the critical strain. Similar effects has been reported in other studies where higher concentration or volume fraction of filler particles decrease the linear viscoelasticity of protein gel by breaking the continuity of protein gel matrix (Ramel and Marangoni, 2018; Sağlam et al., 2014).

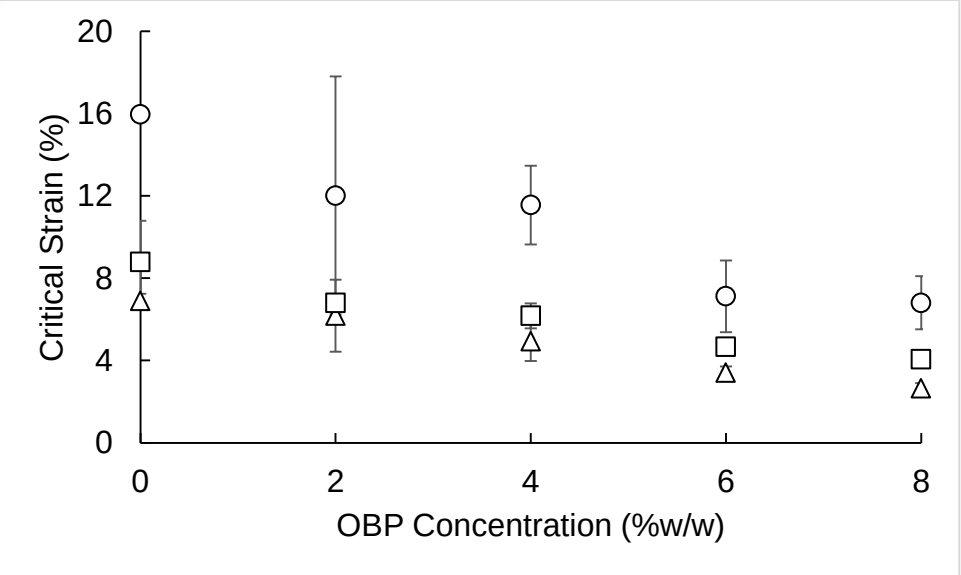

Figure 7.3 Critical strain of protein gels containing 11 (triangle symbols), 13 (square symbols), and 15 (circle symbols) %w/w SPI and various OBP concentrations. The results are the average of duplicate experiments.

7.3.2 Effect of enzymatic crosslinking on protein gel structure

Enzymatic protein crosslinking was meant to modulate the structure of mixed protein gels. Prior to evaluation of mixed system, it is important to examine the effect of MTGase enzyme on individual gel constituents, i.e. SPI and OBP. Figure 7.4 illustrated the effects of MTGase on dynamic modulus of each dispersion. Protein crosslinking activities were observed in SPI dispersion during heating and incubation at 50 ^{o}C. Development of storage modulus accompanied by a relatively constant loss modulus indicated strengthening of protein elastic network. In contrast, a similar effect was not observed within OBP dispersion. This finding differs from other studies that reported successful crosslinking of oat protein induced by MTGase (Huang et al., 2010; Nivala et al., 2017). Responses of protein to MTGase enzyme depend on several factors, including availability, quantity, and spatial distribution of enzyme-reactive substrates, e.g. lisyne and glutamine residues. In this study, justification of non-reactivity of OBP to MTGase requires further investigation. However, some possible causes might include limited substrate availability and/or accessibility due to OBP low purity and matrix complexities of biopolymer mixtures (Gaspar and de Góes-Favoni, 2015; Zeeb et al., 2016).

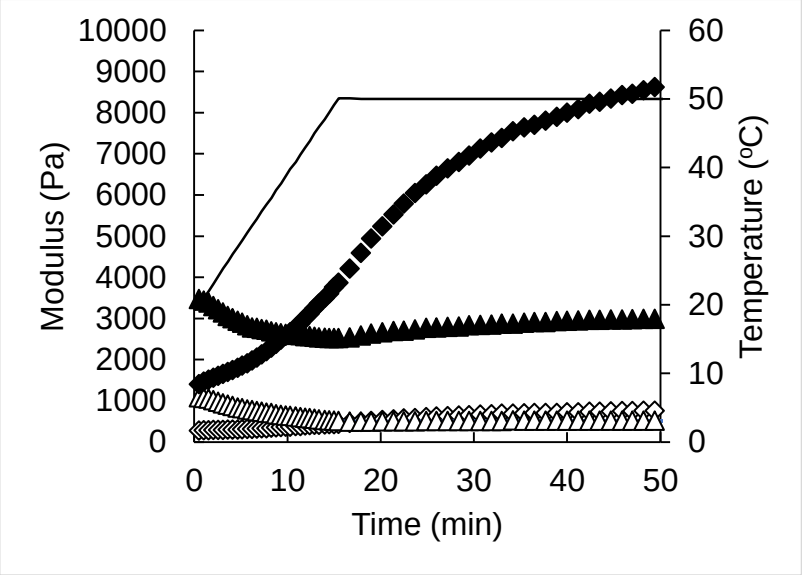

Figure 7.4 Development of storage (filled symbols) and loss (open symbols) modulus of 13%w/w SPI (diamond symbols) and 30%w/w OBP (triangle symbols) dispersions in 50 mM $CaCl_2$ incubated with MTGase enzyme.

Effects of enzymatic crosslinking to the storage modulus of mixed protein gels are presented in Figure 7.5. Increasing OBP concentration in mixed protein gels led to a higher stiffness as previously described. Enzymatic crosslinking further increased the stiffness of protein gels at the same level of OBP concentration. Since OBP did not react with MTGase enzyme, higher storage modulus of crosslinked protein gels is primarily attributed to the strengthening of SPI gel network as a result of polymerisation.

.

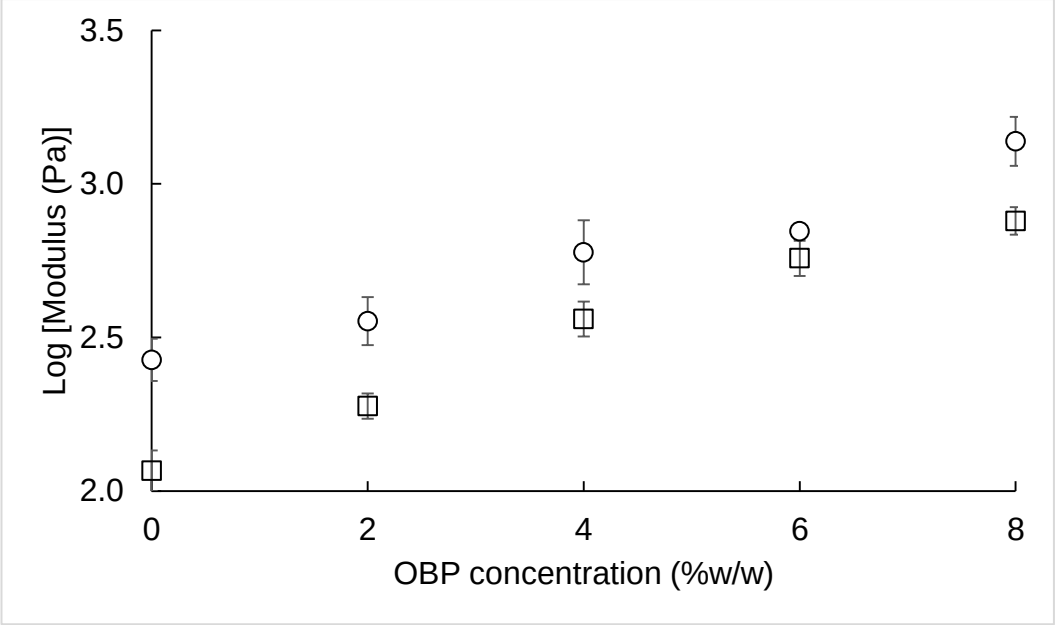

Figure 7.5 Logarithmic plot of storage modulus of mixed protein gels containing 13%w/w SPI and various concentrations of OBP with (circle symbols) and without (square symbols) addition of MTGase enzyme. The results are the average of duplicate experiments.

Enzymatic crosslinking altered deformability and strain-dependency of protein gels as shown in Figure 7.6 and Figure 7.7, respectively. Matrices of the evaluated protein gel samples consisted of interacting SPI particles and showed strain-dependency at high strain values. Crosslinked protein gel, in the absence of OBP, exhibited the lowest critical strain hence the shortest linear viscoelastic region in oppose to non-crosslinked sample. Low critical strain indicated a brittle structure favoured by highly interacting gel (van Riemsdijk et al., 2010). Therefore, enzymatic crosslinking increased the interaction between constituting particles of SPI gel. At the non-linear regime,

crosslinked protein gel showed a steeper modulus decrease indicating a more abruptly affected gel network at high strain values.

OBP addition to protein gels affected deformability and strain-dependency differently between crosslinked and non-crosslinked samples. Increasing OBP concentration within non-crosslinked protein gel gradually decreased critical strain and shortened linear viscoelastic region, whereas the presence of OBP within crosslinked protein gel showed inverse effects. In the former system, the presence of OBP reinforced the SPI matrix hence increasing the interaction of constituting particles. In the latter system, OBP acted as limiting factors to the highly interacting crosslinked SPI particles since OBP was not involved in the crosslinked network.

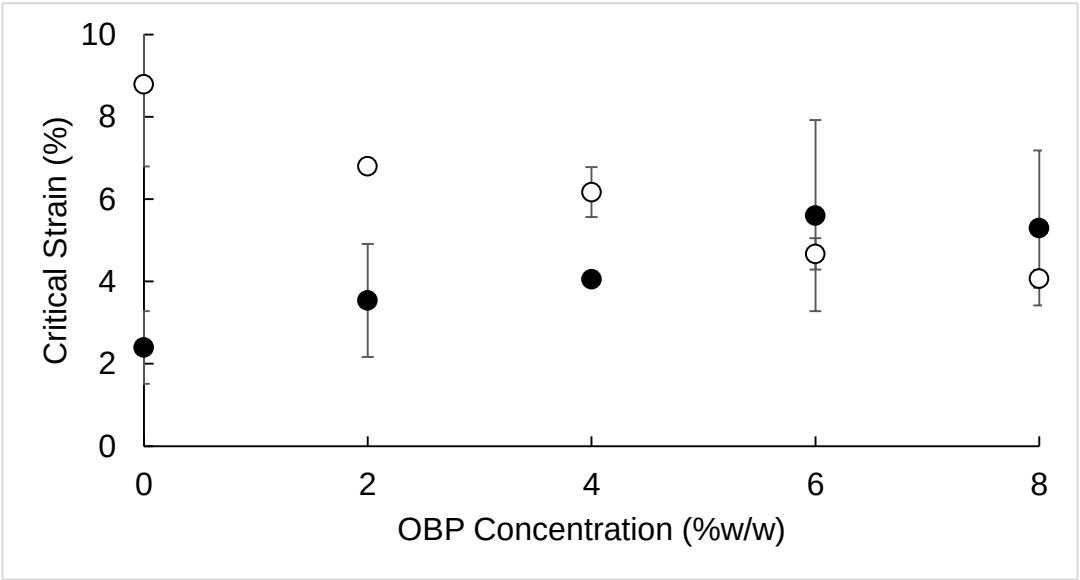

Figure 7.6 Critical strain of protein gels containing 13%w/w SPI treated with (filled symbols) and without (open symbols) enzymatic crosslinking at various concentrations of OBP addition.

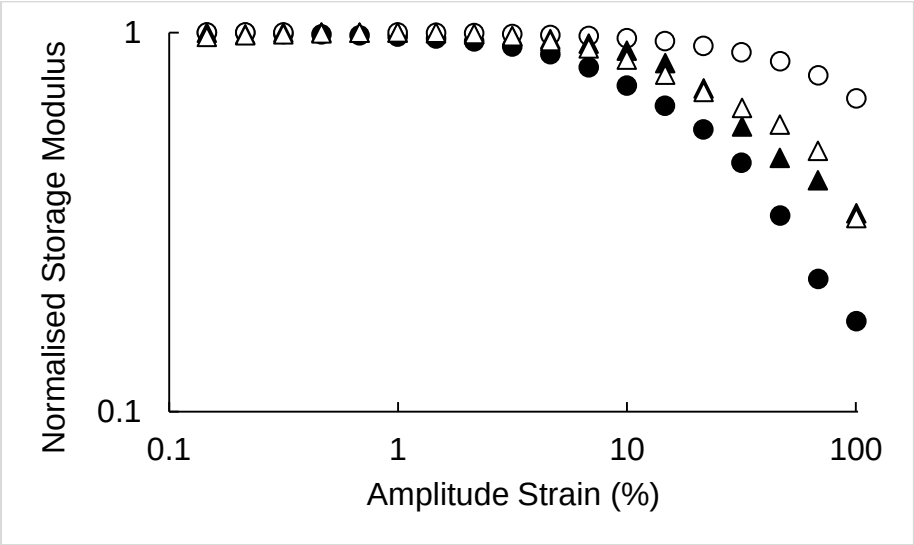

Figure 7.7 Normalised storage modulus of crosslinked (filled symbols) and non-crosslinked (open symbols) protein gels in the absence (circle symbols) and presence (triangle symbols) of 8% OBP concentration plotted against amplitude strain.

7.4 Conclusions

Structural evaluation of heat-induced protein gels containing mixture of SPI and OBP were evaluated. In this study, SPI formed a continuous matrix and OBP was used as filler. Transglutaminase enzyme was able to crosslink SPI, but not OBP due to their lower protein concentration and complexity of polymer mixture. Inclusion of OBP particles up to 8% (w/w) concentration into the enzymatically crosslinked gel matrix achieved the highest gel stiffness and an extended linear viscoelastic region. Therefore, the structure of mixed protein gel system can be modulated by varying concentration of solid constituents and application of enzymatic crosslinking.

8 Conclusions and future work

The usability of commercial protein products in creating solidified gel structure were evaluated in this thesis. The initial works focused on the investigation of highly purified protein materials derived from soybean, namely soy protein isolates (SPI). Comparison of the dispersions containing the same solid concentration of commercial SPI showed variations in its flow properties. These rheological differences were highly influenced by physical and morphological factors of SPI insoluble fractions at the mesoscale structure, which linked to the protein conformation and constituting polypeptide at the molecular scale. Protein conformations of all commercial SPI showed a highly denatured and aggregated structures. Dispersions containing SPI with low molecular weight profile exhibited higher protein solubility and lower specific viscosity, whereas SPI with high molecular weight profile exhibited viscosifying effect to the dispersions and lower solubility. SPI with the lowest protein solubility occupied the largest volume fraction that led to a lower SPI concentration required to exhibit viscoelastic behaviour.

The use of SPI with limited protein solubility in creating solidified gel structure required a thermal treatment in the presence of either calcium chloride or microbial transglutaminase enzyme. Characteristics of the SPI gels were varied according to either compounds. The added calcium ion caused alteration on SPI spatial structure leading to formation of a denser gel matrices. In contrast, the presence of microbial transglutaminase enzyme

increased the dynamic moduli without losing the water retaining ability of initial spatial structure as favoured by newly formed covalent linkages.

Investigation on low purity protein product derived from oat bran were also conducted. Oat bran protein-rich material (OBP) exhibited limited solubility in water. Evaluation on structural properties indicated the aggregated protein structure and the presence of lipid and carbohydrate within OBP in the form of complexes. Physical modification as affected by ball milling resulted in OBP particle size reduction and decreasing the amounts of complexes. OBP dispersions required high solid concentration to obtain a stable concentrated dispersion. Dynamic moduli of OBP dispersion increased as a result of heat-induced structure formation.

The use of SPI and OBP to create mixed protein gel was investigated in the last part of this work. Protein gel structure was built using higher concentration of SPI to create continuous gel matrix, whereas OBP acted as filler particles. Heat-induced gel formation was conducted in the presence of calcium chloride. Increasing filler concentrations to the gel matrix led to a more stiff and brittle protein gel structure. However, addition of filler particles at higher concentration to the enzymatically crosslinked gel matrix increased both stiffness and elasticity of the gel structure.

This work has attempted to show the usability of commercial protein products in creating solidified gel structure that would be beneficial to the development of plant-based protein-rich foods. The solid structure formation required thermal treatment in the presence of calcium ions, which can be modulated by varying the ratio of filler particles and addition of protein crosslinking

enzyme. Since SPI and OBP showed different reactivity to the crosslinking enzyme, it would be useful to further examine the complexes structure within OBP and amino acid compositions to explain enzyme accessibility and reactivity to the substrate. Heat-induced structure formation can be combined with other processing method, such as shearing during extrusion process to manipulate the structure. Therefore, it would be also of great interest to investigate the effect of shearing upon heat-induced structure formation of mixed plant protein system aiming to create a novel protein-rich food structure.

References

Abbaszadeh, A., Macnaughtan, W., Foster, T.J., 2014. The effect of ball milling and rehydration on powdered mixtures of hydrocolloids. Carbohydr. Polym. 102, 978–985. https://doi.org/10.1016/j.carbpol.2013.10.020

Achouri, A., Boye, J.I., Belanger, D., Chiron, T., Yaylayan, V.A., Yeboah, F.K., 2010. Functional and molecular properties of calcium precipitated soy glycinin and the effect of glycation with κ-carrageenan. Food Res. Int. 43, 1494–1504. https://doi.org/10.1016/J.FOODRES.2010.04.005

Ahmed, J., Ramaswamy, H.S., Alli, I., 2006. Thermorheological Characteristics of Soybean Protein Isolate. J. Food Sci. 71, E158–E163. https://doi.org/10.1111/j.1365-2621.2006.tb15629.x

Aiking, H., 2011. Future protein supply. Trends Food Sci. Technol. https://doi.org/10.1016/j.tifs.2010.04.005

Akinori Mizuno, , Masata Mitsuiki, and, Motoki, M., 2000. Effect of Transglutaminase Treatment on the Glass Transition of Soy Protein. https://doi.org/10.1021/JF9911500

Amani, N.G., Buléon, A., Kamenan, A., Colonna, P., 2004. Variability in starch physicochemical and functional properties of yam (*Dioscorea* sp) cultivated in Ivory Coast. J. Sci. Food Agric. 84, 2085–2096. https://doi.org/10.1002/jsfa.1834

Añón, M.C., Sorgentini, D.A., Wagner, J.R., 2001. Relationships between

different hydration properties of commercial and laboratory soybean isolates. J. Agric. Food Chem. 49, 4852–4858. https://doi.org/10.1021/jf010384s

Arii, Y., Takenaka, Y., 2014. Initiation of protein association in tofu formation by metal ions. Biosci. Biotechnol. Biochem. 78, 86–91. https://doi.org/10.1080/09168451.2014.877341

Avanza, M. V., Puppo, M.C., Añón, M.C., 2005. Rheological characterization of amaranth protein gels. Food Hydrocoll. 19, 889–898. https://doi.org/10.1016/j.foodhyd.2004.12.002

Bainy, E.M., Tosh, S.M., Corredig, M., Woodrow, L., Poysa, V., 2008. Protein subunit composition effects on the thermal denaturation at different stages during the soy protein isolate processing and gelation profiles of soy protein isolates. JAOCS, J. Am. Oil Chem. Soc. 85, 581–590. https://doi.org/10.1007/s11746-008-1238-6

Barth, A., 2007. Infrared spectroscopy of proteins. Biochim. Biophys. Acta - Bioenerg. https://doi.org/10.1016/j.bbabio.2007.06.004

Belitz, H.-D., Grosch, W., Schieberle, P., 2009a. Legumes, in: Food Chemistry. Springer Berlin Heidelberg, Berlin, Heidelberg, pp. 746–769. https://doi.org/10.1007/978-3-540-69934-7_17

Belitz, H.-D., Grosch, W., Schieberle, P., 2009b. Cereals and Cereal Products, in: Food Chemistry. Springer Berlin Heidelberg, Berlin, Heidelberg, pp. 275–319.

Berghout, J.A.M., Boom, R.M., van der Goot, A.J., 2015. Understanding the

differences in gelling properties between lupin protein isolate and soy protein isolate. Food Hydrocoll. 43, 465–472. https://doi.org/10.1016/j.foodhyd.2014.07.003

Bio-Rad, 2011. Mini-PROTEAN ® Precast Gels Instruction Manual and Application Guide Bio-Rad Technical Support.

Bock, J.E., Damodaran, S., 2013. Bran-induced changes in water structure and gluten conformation in model gluten dough studied by Fourier transform infrared spectroscopy. Food Hydrocoll. 31, 146–155. https://doi.org/10.1016/j.foodhyd.2012.10.014

Boye, J.I., Aksay, S., Roufik, S., Ribéreau, S., Mondor, M., Farnworth, E., Rajamohamed, S.H., 2010. Comparison of the functional properties of pea, chickpea and lentil protein concentrates processed using ultrafiltration and isoelectric precipitation techniques. Food Res. Int. 43, 537–546. https://doi.org/10.1016/J.FOODRES.2009.07.021

Brückner-Gühmann, M., Banovic, M., Drusch, S., 2019. Towards an increased plant protein intake: Rheological properties, sensory perception and consumer acceptability of lactic acid fermented, oat-based gels. Food Hydrocoll. 96, 201–208. https://doi.org/10.1016/j.foodhyd.2019.05.016

Campbell, C.L., Wagoner, T.B., Foegeding, E.A., 2017. Designing foods for satiety: The roles of food structure and oral processing in satiation and satiety. Food Struct. https://doi.org/10.1016/j.foostr.2016.08.002

Campbell, L.J., Gu, X., Dewar, S.J., Euston, S.R., 2009. Effects of heat treatment and glucono-δ-lactone-induced acidification on characteristics

of soy protein isolate. Food Hydrocoll. 23, 344–351. https://doi.org/10.1016/J.FOODHYD.2008.03.004

Celia, C., Trapasso, E., Cosco, D., Paolino, D., Fresta, M., 2009. Turbiscan Lab® Expert analysis of the stability of ethosomes® and ultradeformable liposomes containing a bilayer fluidizing agent. Colloids Surfaces B Biointerfaces 72, 155–160. https://doi.org/10.1016/J.COLSURFB.2009.03.007

Cerqueira, M.A., Souza, B.W.S., Teixeira, J.A., Vicente, A.A., 2012. Effect of glycerol and corn oil on physicochemical properties of polysaccharide films – A comparative study. Food Hydrocoll. 27, 175–184. https://doi.org/10.1016/J.FOODHYD.2011.07.007

Chambers, L., McCrickerd, K., Yeomans, M.R., 2015. Optimising foods for satiety. Trends Food Sci. Technol. 41, 149–160. https://doi.org/10.1016/J.TIFS.2014.10.007

Chang, Y.-H., Shiau, S.-Y., Chen, F.-B., Lin, F.-R., 2011. Effect of microbial transglutaminase on the rheological and textural characteristics of black soybean packed tofu coagulating with Agar. LWT - Food Sci. Technol. 44, 1107–1112. https://doi.org/10.1016/J.LWT.2010.10.020

Clara Sze, K.W., Kshirsagar, H.H., Venkatachalam, M., Sathe, S.K., 2007. A Circular Dichroism and Fluorescence Spectrometric Assessment of Effects of Selected Chemical Denaturants on Soybean (*Glycine max* L.) Storage Proteins Glycinin (11S) and β-Conglycinin (7S). J. Agric. Food Chem. 55, 8745–8753. https://doi.org/10.1021/jf071364e

Day, L., 2013. Proteins from land plants - Potential resources for human

nutrition and food security. Trends Food Sci. Technol. https://doi.org/10.1016/j.tifs.2013.05.005

De Pilli, T., Legrand, J., Derossi, A., Severini, C., 2015. Effect of proteins on the formation of starch-lipid complexes during extrusion cooking of wheat flour with the addition of oleic acid. Int. J. Food Sci. Technol. https://doi.org/10.1111/ijfs.12698

De Souza, D., Sbardelotto, A.F., Ziegler, D.R., Marczak, L.D.F., Tessaro, I.C., 2016. Characterization of rice starch and protein obtained by a fast alkaline extraction method. Food Chem. https://doi.org/10.1016/j.foodchem.2015.03.032

Deutz, N.E.P., Bauer, J.M., Barazzoni, R., Biolo, G., Boirie, Y., Bosy-Westphal, A., Cederholm, T., Cruz-Jentoft, A., Krznariç, Z., Nair, K.S., Singer, P., Teta, D., Tipton, K., Calder, P.C., 2014. Protein intake and exercise for optimal muscle function with aging: Recommendations from the ESPEN Expert Group. Clin. Nutr. 33, 929–936. https://doi.org/10.1016/j.clnu.2014.04.007

Dhital, S., Shrestha, A.K., Flanagan, B.M., Hasjim, J., Gidley, M.J., 2011. Cryo-milling of starch granules leads to differential effects on molecular size and conformation. Carbohydr. Polym. 84, 1133–1140. https://doi.org/10.1016/j.carbpol.2011.01.002

Doehlert, D.C., Moreau, R.A., Welti, R., Roth, M.R., McMullen, M.S., 2010. Polar Lipids from Oat Kernels. Cereal Chem. J. 87, 467–474. https://doi.org/10.1094/CCHEM-04-10-0060

Don, C., 2017. Future proteins: Functionality, processing, and sourcing.

Cereal Foods World 62, 144–147. https://doi.org/10.1094/CFW-62-4-0144

Dubey, B.N., Windhab, E.J., 2013. Iron encapsulated microstructured emulsion-particle formation by prilling process and its release kinetics. J. Food Eng. 115, 198–206. https://doi.org/10.1016/j.jfoodeng.2012.10.013

Eissa, A.S., Puhl, C., Kadla, J.F., Khan, S.A., 2006. Enzymatic Cross-Linking of β-Lactoglobulin: Conformational Properties Using FTIR Spectroscopy. Biomacromolecules 7, 1707–1713. https://doi.org/10.1021/bm050928p

Fabian, C., Ju, Y.H., 2011. A review on rice bran protein: Its properties and extraction methods. Crit. Rev. Food Sci. Nutr. 51, 816–827. https://doi.org/10.1080/10408398.2010.482678

Foegeding, E.A., 2015. Food Protein Functionality—A New Model. J. Food Sci. 80, C2670–C2677. https://doi.org/10.1111/1750-3841.13116

Food and Agriculture Organization of the United Nations, 2019. FAOSTAT Database [WWW Document]. URL http://www.fao.org/faostat/en/#data/QC

Formulaction SAS, 2007. Turbiscan® LAB user guide.

Gaspar, A.L.C., de Góes-Favoni, S.P., 2015. Action of microbial transglutaminase (MTGase) in the modification of food proteins: A review. Food Chem. 171, 315–322. https://doi.org/10.1016/J.FOODCHEM.2014.09.019

Gorissen, S.H.M., Crombag, J.J.R., Senden, J.M.G., Waterval, W.A.H.,

Bierau, J., Verdijk, L.B., van Loon, L.J.C., 2018. Protein content and amino acid composition of commercially available plant-based protein isolates. Amino Acids 50, 1685–1695. https://doi.org/10.1007/s00726-018-2640-5

Grabowska, K.J., Tekidou, S., Boom, R.M., van der Goot, A.J., 2014. Shear structuring as a new method to make anisotropic structures from soy-gluten blends. Food Res. Int. 64, 743–751. https://doi.org/10.1016/j.foodres.2014.08.010

Grygorczyk, A., Corredig, M., 2013. Acid induced gelation of soymilk, comparison between gels prepared with lactic acid bacteria and glucono-δ-lactone. Food Chem. 141, 1716–1721. https://doi.org/10.1016/J.FOODCHEM.2013.03.096

Guan, X., Yao, H., 2008. Optimization of Viscozyme L-assisted extraction of oat bran protein using response surface methodology. Food Chem. 106, 345–351. https://doi.org/10.1016/j.foodchem.2007.05.041

Guan, X., Yao, H., Chen, Z., Shan, L., Zhang, M., 2007. Some functional properties of oat bran protein concentrate modified by trypsin. Food Chem. 101, 163–170. https://doi.org/10.1016/j.foodchem.2006.01.011

Guerrero, P., Kerry, J.P., de la Caba, K., 2014. FTIR characterization of protein–polysaccharide interactions in extruded blends. Carbohydr. Polym. 111, 598–605. https://doi.org/10.1016/J.CARBPOL.2014.05.005

Gunasekaran, S., Xiao, L., Ould Eleya, M.M., 2006. Whey protein concentrate hydrogels as bioactive carriers. J. Appl. Polym. Sci. 99, 2470–2476. https://doi.org/10.1002/app.22838

Guo, J., Yang, X.Q., He, X.T., Wu, N.N., Wang, J.M., Gu, W., Zhang, Y.Y., 2012. Limited aggregation behavior of β-conglycinin and its terminating effect on glycinin aggregation during heating at pH 7.0. J. Agric. Food Chem. 60, 3782–3791. https://doi.org/10.1021/jf300409y

Halton, T.L., Hu, F.B., 2013. The Effects of High Protein Diets on Thermogenesis, Satiety and Weight Loss: A Critical Review. http://dx.doi.org/10.1080/07315724.2004.10719381.

Hartmann, C., Siegrist, M., 2017. Consumer perception and behaviour regarding sustainable protein consumption: A systematic review. Trends Food Sci. Technol. https://doi.org/10.1016/j.tifs.2016.12.006

Hou, J.-J., Yang, X.-Q., Fu, S.-R., Wang, M.-P., Xiao, F., 2016. Preparation of double-network tofu with mechanical and sensory toughness. Int. J. Food Sci. Technol. 51, 962–969. https://doi.org/10.1111/ijfs.13043

Hsiao, Y.H., Yu, C.J., Li, W.T., Hsieh, J.F., 2015. Coagulation of β-conglycinin, glycinin and isoflavones induced by calcium chloride in soymilk. Sci. Rep. 5. https://doi.org/10.1038/srep13018

Hu, H., Wu, J., Li-Chan, E.C.Y., Zhu, L., Zhang, F., Xu, X., Fan, G., Wang, L., Huang, X., Pan, S., 2013. Effects of ultrasound on structural and physical properties of soy protein isolate (SPI) dispersions. Food Hydrocoll. 30, 647–655. https://doi.org/10.1016/J.FOODHYD.2012.08.001

Huang, W., Li, L., Wang, F., Wan, J., Tilley, M., Ren, C., Wu, S., 2010. Effects of transglutaminase on the rheological and Mixolab thermomechanical characteristics of oat dough. Food Chem. 121, 934–

939. https://doi.org/10.1016/j.foodchem.2010.01.008

Hui, L.K., Easa, A.M., Ismail, N., 2000. Effects of thermal treatments on texture of soy protein isolate tofu. J. Food Process. Preserv. 24, 275–286. https://doi.org/10.1111/j.1745-4549.2000.tb00419.x

Jambrak, A.R., Lelas, V., Mason, T.J., Krešić, G., Badanjak, M., 2009. Physical properties of ultrasound treated soy proteins. J. Food Eng. 93, 386–393. https://doi.org/10.1016/J.JFOODENG.2009.02.001

Janssen, F., Pauly, A., Rombouts, I., Jansens, K.J.A., Deleu, L.J., Delcour, J.A., 2017. Proteins of Amaranth (*Amaranthus* spp.), Buckwheat (*Fagopyrum* spp.), and Quinoa (*Chenopodium* spp.): A Food Science and Technology Perspective. Compr. Rev. Food Sci. Food Saf. 16, 39–58. https://doi.org/10.1111/1541-4337.12240

Jing, X., Yang, C., Zhang, L., 2016. Characterization and Analysis of Protein Structures in Oat Bran. J. Food Sci. https://doi.org/10.1111/1750-3841.13445

Jodayree, S., Smith, J.C., Tsopmo, A., 2012. Use of carbohydrase to enhance protein extraction efficiency and antioxidative properties of oat bran protein hydrolysates. Food Res. Int. 46, 69–75. https://doi.org/10.1016/j.foodres.2011.12.004

Kasprzak, M.M., Macnaughtan, W., Harding, S., Wilde, P., Wolf, B., 2018. Stabilisation of oil-in-water emulsions with non-chemical modified gelatinised starch. Food Hydrocoll. 81, 409–418. https://doi.org/10.1016/j.foodhyd.2018.03.002

Kawai, K., Takato, S., Sasaki, T., Kajiwara, K., 2012. Complex formation, thermal properties, and in-vitro digestibility of gelatinized potato starch-fatty acid mixtures. Food Hydrocoll. https://doi.org/10.1016/j.foodhyd.2011.07.003

Keerati-u-rai, M., Wang, Z., Corredig, M., 2011. Adsorption of Soy Protein Isolate in Oil-in-Water Emulsions: Difference Between Native and Spray Dried Isolate. J. Am. Oil Chem. Soc. 88, 1593–1602. https://doi.org/10.1007/s11746-011-1818-8

Konak, Ü.İ., Ercili-Cura, D., Sibakov, J., Sontag-Strohm, T., Certel, M., Loponen, J., 2014. CO2-defatted oats: Solubility, emulsification and foaming properties. J. Cereal Sci. 60, 37–41. https://doi.org/10.1016/j.jcs.2014.01.013

Kong, J., Yu, S., 2007. Fourier transform infrared spectroscopic analysis of protein secondary structures. Acta Biochim. Biophys. Sin. (Shanghai). 39, 549–559. https://doi.org/10.1111/j.1745-7270.2007.00320.x

Krintiras, G.A., Göbel, J., Van Der Goot, A.J., Stefanidis, G.D., 2015. Production of structured soy-based meat analogues using simple shear and heat in a Couette Cell. J. Food Eng. 160, 34–41. https://doi.org/10.1016/j.jfoodeng.2015.02.015

Kwan, S.W., Easa, A.M., 2003. Comparing physical properties of retort-resistant glucono-δ-lactone tofu treated with commercial transglutaminase enzyme or low levels of glucose. LWT - Food Sci. Technol. 36, 643–646. https://doi.org/10.1016/S0023-6438(03)00080-X

Lakemond, C.M.M., Jongh, H.H.J. de, Hessing, M., Gruppen, H., Voragen,

A.G.J., 2000. Soy Glycinin: Influence of pH and Ionic Strength on Solubility and Molecular Structure at Ambient Temperatures. https://doi.org/10.1021/JF9908695

Larsen, D.S., Tang, J., Ferguson, L.R., James, B.J., 2016. Increased textural complexity in food enhances satiation. Appetite 105, 189–194. https://doi.org/10.1016/j.appet.2016.05.029

Liu, B., Wang, H., Hu, T., Zhang, P., Zhang, Z., Pan, S., Hu, H., 2017. Ball-milling changed the physicochemical properties of SPI and its cold-set gels. J. Food Eng. https://doi.org/10.1016/j.jfoodeng.2016.10.006

Liu, G., Li, J., Shi, K., Wang, S., Chen, J., Liu, Y., Huang, Q., 2009. Composition, secondary structure, and self-assembly of oat protein isolate. J. Agric. Food Chem. https://doi.org/10.1021/jf900135e

Liu, J., Guan, X., Zhu, D., Sun, J., 2008. Optimization of the enzymatic pretreatment in oat bran protein extraction by particle swarm optimization algorithms for response surface modeling. LWT - Food Sci. Technol. 41, 1913–1918. https://doi.org/10.1016/j.lwt.2008.02.013

Liu, T.Y., Ma, Y., Yu, S.F., Shi, J., Xue, S., 2011. The effect of ball milling treatment on structure and porosity of maize starch granule. Innov. Food Sci. Emerg. Technol. 12, 586–593. https://doi.org/10.1016/J.IFSET.2011.06.009

Maltais, A., Remondetto, G.E., Subirade, M., 2008. Mechanisms involved in the formation and structure of soya protein cold-set gels: A molecular and supramolecular investigation. Food Hydrocoll. 22, 550–559. https://doi.org/10.1016/j.foodhyd.2007.01.026

Maphosa, Y., Jideani, V.A., 2017. The Role of Legumes in Human Nutrition, in: Functional Food - Improve Health through Adequate Food. https://doi.org/10.5772/intechopen.69127

Miller, S.S., Fulcher, R.G., 2011. Microstructure and Chemistry of the Oat Kernel, in: Oats: Chemistry and Technology: Second Edition. pp. 77–94. https://doi.org/10.1016/B978-1-891127-64-9.50010-5

Miriani, M., Keerati-u-rai, M., Corredig, M., Iametti, S., Bonomi, F., 2011. Denaturation of soy proteins in solution and at the oil–water interface: A fluorescence study. Food Hydrocoll. 25, 620–626. https://doi.org/10.1016/J.FOODHYD.2010.07.020

Moisio, T., Forssell, P., Partanen, R., Damerau, A., Hill, S.E., 2015. Reorganisation of starch, proteins and lipids in extrusion of oats. J. Cereal Sci. https://doi.org/10.1016/j.jcs.2015.04.001

Molina, E., Papadopoulou, A., Ledward, D.., 2001. Emulsifying properties of high pressure treated soy protein isolate and 7S and 11S globulins. Food Hydrocoll. 15, 263–269. https://doi.org/10.1016/S0268-005X(01)00023-6

Moreira, R., Chenlo, F., Torres, M.D., Prieto, D.M., 2010. Influence of the particle size on the rheological behaviour of chestnut flour doughs. J. Food Eng. 100, 270–277. https://doi.org/10.1016/j.jfoodeng.2010.04.009

Morell, P., Fiszman, S., 2017. Revisiting the role of protein-induced satiation and satiety. Food Hydrocoll. 68, 199–210. https://doi.org/10.1016/J.FOODHYD.2016.08.003

Moure, A., Sineiro, J., Domínguez, H., Parajó, J.C., 2006. Functionality of oilseed protein products: A review. Food Res. Int. https://doi.org/10.1016/j.foodres.2006.07.002

Nadathur, S.R., Wanasundara, J.P.D., Scanlin, L., 2016. Proteins in the Diet: Challenges in Feeding the Global Population, in: Sustainable Protein Sources. Elsevier Inc., pp. 1–19. https://doi.org/10.1016/B978-0-12-802778-3.00001-9

Nishinari, K., Fang, Y., Guo, S., Phillips, G.O., 2014. Soy proteins: A review on composition, aggregation and emulsification. Food Hydrocoll. 39, 301–318. https://doi.org/10.1016/j.foodhyd.2014.01.013

Nivala, O., Mäkinen, O.E., Kruus, K., Nordlund, E., Ercili-Cura, D., 2017. Structuring colloidal oat and faba bean protein particles via enzymatic modification. Food Chem. 231, 87–95. https://doi.org/10.1016/j.foodchem.2017.03.114

Orona-Tamayo, D., Paredes-López, O., 2017. Amaranth Part 1—Sustainable Crop for the 21st Century: Food Properties and Nutraceuticals for Improving Human Health. Sustain. Protein Sources 239–256. https://doi.org/10.1016/B978-0-12-802778-3.00015-9

Ottenhof, M.-A., MacNaughtan, W., Farhat, I.A., 2003. FTIR study of state and phase transitions of low moisture sucrose and lactose. Carbohydr. Res. 338, 2195–2202. https://doi.org/10.1016/S0008-6215(03)00342-2

Pandey, R., Shrivastava, S.L., 2018. Comparative evaluation of rice bran oil obtained with two-step microwave assisted extraction and conventional solvent extraction. J. Food Eng.

https://doi.org/10.1016/j.jfoodeng.2017.09.009

Pelgrom, P.J.M., Vissers, A.M., Boom, R.M., Schutyser, M.A.I., 2013. Dry fractionation for production of functional pea protein concentrates. Food Res. Int. https://doi.org/10.1016/j.foodres.2013.05.004

Pihlanto, A., Mattila, P., Mäkinen, S., Pajari, A.-M., 2017. Bioactivities of alternative protein sources and their potential health benefits. Food Funct. 8, 3443–3458. https://doi.org/10.1039/C7FO00302A

Preece, K.E., Hooshyar, N., Zuidam, N.J., 2017. Whole soybean protein extraction processes: A review. Innov. Food Sci. Emerg. Technol. 43, 163–172. https://doi.org/10.1016/J.IFSET.2017.07.024

Ramel, P.R., Marangoni, A.G., 2018. Engineering the rheological and thermomechanical properties of model imitation cheese using particle fillers. J. Food Eng. 235, 9–15. https://doi.org/10.1016/j.jfoodeng.2018.03.023

Raphaely, T., Marinova, D., 2014. Flexitarianism: Decarbonising through flexible vegetarianism. Renew. Energy 67, 90–96. https://doi.org/10.1016/j.renene.2013.11.030

Renkema, J.M.., Lakemond, C.M.., de Jongh, H.H.., Gruppen, H., van Vliet, T., 2000. The effect of pH on heat denaturation and gel forming properties of soy proteins. J. Biotechnol. 79, 223–230. https://doi.org/10.1016/S0168-1656(00)00239-X

Renkema, J.M.S., 2004. Relations between rheological properties and network structure of soy protein gels. Food Hydrocoll. 18, 39–47.

https://doi.org/10.1016/S0268-005X(03)00040-7

Renkema, J.M.S., Gruppen, H., Van Vliet, T., 2002. Influence of pH and ionic strength on heat-induced formation and rheological properties of soy protein gels in relation to denaturation and their protein compositions. J. Agric. Food Chem. 50, 6064–6071. https://doi.org/10.1021/jf020061b

Renkema, J.M.S., Knabben, J.H.M., van Vliet, T., 2001. Gel formation by β-conglycinin and glycinin and their mixtures. Food Hydrocoll. 15, 407–414. https://doi.org/10.1016/S0268-005X(01)00051-0

Roa, D.F., Baeza, R.I., Tolaba, M.P., 2015. Effect of ball milling energy on rheological and thermal properties of amaranth flour. J. Food Sci. Technol. https://doi.org/10.1007/s13197-015-1976-z

Roa, D.F., Santagapita, P.R., Buera, M.P., Tolaba, M.P., 2014a. Ball Milling of Amaranth Starch-Enriched Fraction. Changes on Particle Size, Starch Crystallinity, and Functionality as a Function of Milling Energy. Food Bioprocess Technol. 7, 2723–2731. https://doi.org/10.1007/s11947-014-1283-0

Roa, D.F., Santagapita, P.R., Buera, M.P., Tolaba, M.P., 2014b. Amaranth Milling Strategies and Fraction Characterization by FT-IR. Food Bioprocess Technol. 7, 711–718. https://doi.org/10.1007/s11947-013-1050-7

Rutherfurd, S.M., Montoya, C.A., Zou, M.L., Moughan, P.J., Drummond, L.N., Boland, M.J., 2011. Effect of actinidin from kiwifruit (Actinidia deliciosa cv. Hayward) on the digestion of food proteins determined in the growing rat. Food Chem. 129, 1681–1689.

https://doi.org/10.1016/J.FOODCHEM.2011.06.031

Ryan, M., McEvoy, E., Duignan, S., Crowley, C., Fenelon, M., O'Callaghan, D.M., FitzGerald, R.J., 2008. Thermal stability of soy protein isolate and hydrolysate ingredients. Food Chem. 108, 503–510. https://doi.org/10.1016/J.FOODCHEM.2007.11.001

Sağlam, D., Venema, P., de Vries, R., van den Berg, M., van der Linden, E., 2014. Whey protein particles modulate mechanical properties of gels at high protein concentrations. Food Hydrocoll. 38, 163–171. https://doi.org/10.1016/j.foodhyd.2013.11.015

Sağlam, D., Venema, P., de Vries, R., van der Linden, E., 2013. The influence of pH and ionic strength on the swelling of dense protein particles. Soft Matter 9, 4598. https://doi.org/10.1039/c3sm50170a

Sandefur, H.N., McCarty, J.A., Boles, E.C., Matlock, M.D., 2016. Peanut Products as a Protein Source: Production, Nutrition, and Environmental Impact, in: Sustainable Protein Sources. Elsevier, pp. 209–221. https://doi.org/10.1016/B978-0-12-802778-3.00013-5

Saowapark, S., Apichartsrangkoon, A., Bell, A.E., 2008. Viscoelastic properties of high pressure and heat induced tofu gels. Food Chem. 107, 984–989. https://doi.org/10.1016/J.FOODCHEM.2007.08.091

Scanlin, L., Lewis, K.A., 2017. Quinoa as a Sustainable Protein Source: Production, Nutrition, and Processing. Sustain. Protein Sources 223–238. https://doi.org/10.1016/B978-0-12-802778-3.00014-7

Schmitt, C., Bovay, C., Vuilliomenet, A.-M., Rouvet, M., Bovetto, L., Barbar,

R., Sanchez, C., 2009. Multiscale Characterization of Individualized β-Lactoglobulin Microgels Formed upon Heat Treatment under Narrow pH Range Conditions. Langmuir 25, 7899–7909. https://doi.org/10.1021/la900501n

Schutyser, M.A.I., van der Goot, A.J., 2011. The potential of dry fractionation processes for sustainable plant protein production. Trends Food Sci. Technol. https://doi.org/10.1016/j.tifs.2010.11.006

Scilingo, A.A., Añón, M.C., 2004. Characterization of soybean protein isolates The effect of calcium presence. J. Am. Oil Chem. Soc. 81, 63–69. https://doi.org/10.1007/s11746-004-0858-y

Sendra, E., Kuri, V., Fernández-López, J., Sayas-Barberá, E., Navarro, C., Pérez-Alvarez, J.A., 2010. Viscoelastic properties of orange fiber enriched yogurt as a function of fiber dose, size and thermal treatment. LWT - Food Sci. Technol. 43, 708–714. https://doi.org/10.1016/j.lwt.2009.12.005

Shand, P.J., Ya, H., Pietrasik, Z., Wanasundara, P.K.J.P.D., 2007. Physicochemical and textural properties of heat-induced pea protein isolate gels. Food Chem. 102, 1119–1130. https://doi.org/10.1016/j.foodchem.2006.06.060

Shewan, H., 2015. Rheology of soft particle suspensions. The University of Queensland. https://doi.org/10.14264/uql.2015.533

Shewan, H.M., Stokes, J.R., 2015. Viscosity of soft spherical micro-hydrogel suspensions. J. Colloid Interface Sci. 442, 75–81. https://doi.org/10.1016/J.JCIS.2014.11.064

Shewan, H.M., Stokes, J.R., 2012. Biopolymer Microgel Suspension Rheology as a Function of Particle Modulus and Effective Phase Volume, in: Gums and Stabilisers for the Food Industry 16. pp. 165–174.

Shivu, B., Seshadri, S., Li, J., Oberg, K.A., Uversky, V.N., Fink, A.L., 2013. Distinct β-Sheet Structure in Protein Aggregates Determined by ATR–FTIR Spectroscopy. Biochemistry 52, 5176–5183. https://doi.org/10.1021/bi400625v

Singh, P., Kumar, R., Sabapathy, S.N., Bawa, A.S., 2008. Functional and Edible Uses of Soy Protein Products. Compr. Rev. Food Sci. Food Saf. 7, 14–28. https://doi.org/10.1111/j.1541-4337.2007.00025.x

Sirison, J., Matsumiya, K., Samoto, M., Hidaka, H., Kouno, M., Matsumura, Y., 2017. Solubility of soy lipophilic proteins: Comparison with other soy protein fractions. Biosci. Biotechnol. Biochem. 81, 790–802. https://doi.org/10.1080/09168451.2017.1282808

Sozer, N., Nordlund, E., Ercili-Cura, D., Poutanen, K., 2017. Cereal Side-Streams as Alternative Protein Sources. Cereal Foods World 62, 132–137. https://doi.org/10.1094/CFW-62-4-0132

Sun, C., Liu, R., Wu, T., Liang, B., Shi, C., Zhang, M., 2015. Effect of superfine grinding on the structural and physicochemical properties of whey protein and applications for microparticulated proteins. Food Sci. Biotechnol. https://doi.org/10.1007/s10068-015-0212-y

Tang, C.-H., Chen, Z., Li, L., Yang, X.-Q., 2006a. Effects of transglutaminase treatment on the thermal properties of soy protein isolates. Food Res. Int. 39, 704–711. https://doi.org/10.1016/J.FOODRES.2006.01.012

Tang, C.-H., Li, L., Wang, J.-L., Yang, X.-Q., 2007. Formation and rheological properties of ‘cold-set’ tofu induced by microbial transglutaminase. LWT - Food Sci. Technol. 40, 579–586. https://doi.org/10.1016/J.LWT.2006.03.001

Tang, C.-H., Wu, H., Yu, H., Li, L., Chen, Z., Yang, X., 2006b. Coagulation and gelation of soy protein isolates induced by microbial transglutaminase. J. Food Biochem. 30, 35–55. https://doi.org/10.1111/j.1745-4514.2005.00049.x

Tang, C.H., Ma, C.Y., 2009. Effect of high pressure treatment on aggregation and structural properties of soy protein isolate. LWT - Food Sci. Technol. 42, 606–611. https://doi.org/10.1016/j.lwt.2008.07.012

Tang, C.H., Wang, X.Y., Yang, X.Q., Li, L., 2009. Formation of soluble aggregates from insoluble commercial soy protein isolate by means of ultrasonic treatment and their gelling properties. J. Food Eng. 92, 432–437. https://doi.org/10.1016/j.jfoodeng.2008.12.017

Tang, J., Larsen, D.S., Ferguson, L.R., James, B.J., 2016. The effect of textural complexity of solid foods on satiation. Physiol. Behav. 163, 17–24. https://doi.org/10.1016/j.physbeh.2016.04.042

Thanatuksorn, P., Kawai, K., Kajiwara, K., Suzuki, T., 2009. Effects of ball-milling on the glass transition of wheat flour constituents. J. Sci. Food Agric. https://doi.org/10.1002/jsfa.3463

Thermo Scientific, 2011. User Guide: Pierce BCA Protein Assay Kit. Pierce Biotechnol. https://doi.org/10.1016/j.ijproman.2010.02.012

Thrane, M., Paulsen, P.V., Orcutt, M.W., Krieger, T.M., 2017. Soy Protein: Impacts, Production, and Applications, in: Sustainable Protein Sources. Academic Press, pp. 23–45.

Totosaus, A., Montejano, J.G., Salazar, J.A., Guerrero, I., 2002. A review of physical and chemical protein-gel induction. Int. J. Food Sci. Technol. https://doi.org/10.1046/j.1365-2621.2002.00623.x

Tufvesson, F., Wahlgren, M., Eliasson, A.C., 2003. Formation of amylose-lipid complexes and effects of temperature treatment - Part 1. Monoglycerides. Starch/Staerke. https://doi.org/10.1002/star.200390018

United States Department of Agriculture, 2019. World Agricultural Production.

Urbonaite, V., de Jongh, H.H.J.J., Van der Linden, E., Pouvreau, L., 2014. Origin of water loss from soy protein gels. J. Agric. Food Chem. 62, 7550–7558. https://doi.org/10.1021/jf501728t

Utrilla-Coello, R.G., Rodríguez-Huezo, M.E., Carrillo-Navas, H., Hernández-Jaimes, C., Vernon-Carter, E.J., Alvarez-Ramirez, J., 2014. In vitro digestibility, physicochemical, thermal and rheological properties of banana starches. Carbohydr. Polym. 101, 154–162. https://doi.org/10.1016/J.CARBPOL.2013.09.019

Van Der Sman, R.G.M., 2012. Soft matter approaches to food structuring. Adv. Colloid Interface Sci. https://doi.org/10.1016/j.cis.2012.04.002

van Riemsdijk, L.E., Sprakel, J.H.B., van der Goot, A.J., Hamer, R.J., 2010. Elastic Networks of Protein Particles. Food Biophys. 5, 41–48.

https://doi.org/10.1007/s11483-009-9142-7

Vercet, A., Sánchez, C., Burgos, J., Montañés, L., Lopez Buesa, P., 2002. The effects of manothermosonication on tomato pectic enzymes and tomato paste rheological properties. J. Food Eng. 53, 273–278. https://doi.org/10.1016/S0260-8774(01)00165-0

Wagner, J.R., Sorgentini, D.A., Anon, M.C., 2000. Relation between solubility and surface hydrophobicity as an indicator of modifications during preparation processes of commercial and laboratory-prepared soy protein isolates. J. Agric. Food Chem. 48, 3159–3165. https://doi.org/10.1021/jf990823b

Wanasundara, J.P.D., 2011. Proteins of brassicaceae oilseeds and their potential as a plant protein source. Crit. Rev. Food Sci. Nutr. https://doi.org/10.1080/10408391003749942

Wang, Shujun, Zheng, M., Yu, J., Wang, Shuo, Copeland, L., 2017. Insights into the Formation and Structures of Starch-Protein-Lipid Complexes. J. Agric. Food Chem. https://doi.org/10.1021/acs.jafc.6b05772

Wang, X., Luo, K., Liu, S., Zeng, M., Adhikari, B., He, Z., Chen, J., 2018. Textural and Rheological Properties of Soy Protein Isolate Tofu-Type Emulsion Gels: Influence of Soybean Variety and Coagulant Type. Food Biophys. 13, 324–332. https://doi.org/10.1007/s11483-018-9538-3

Wellner, N., Mills, E.N.C., Brownsey, G., Wilson, R.H., Brown, N., Freeman, J., Halford, N.G., Shewry, P.R., Belton, P.S., 2005. Changes in protein secondary structure during gluten deformation studied by dynamic fourier transform infrared spectroscopy. Biomacromolecules.

https://doi.org/10.1021/bm049584d

Westerterp-Plantenga, M.S., Lemmens, S.G., Westerterp, K.R., 2017. Dietary protein – its role in satiety, energetics, weight loss and health. https://doi.org/10.1017/S0007114512002589

Williamson, D.A., Geiselman, P.J., Lovejoy, J., Greenway, F., Volaufova, J., Martin, C.K., Arnett, C., Ortego, L., 2006. Effects of consuming mycoprotein, tofu or chicken upon subsequent eating behaviour, hunger and safety. Appetite 46, 41–48. https://doi.org/10.1016/J.APPET.2005.10.007

Wu, H., Wang, Q., Ma, T., Ren, J., 2009. Comparative studies on the functional properties of various protein concentrate preparations of peanut protein. Food Res. Int. 42, 343–348. https://doi.org/10.1016/J.FOODRES.2008.12.006

Wu, S., Murphy, P.A., Johnson, L.A., Reuber, M.A., Fratzke, A.R., 2000. Simplified process for soybean glycinin and β-conglycinin fractionation. J. Agric. Food Chem. 48, 2702–2708. https://doi.org/10.1021/jf990785w

Yang, C., Wang, Y., Vasanthan, T., Chen, L., 2014. Impacts of pH and heating temperature on formation mechanisms and properties of thermally induced canola protein gels. Food Hydrocoll. 40, 225–236. https://doi.org/10.1016/j.foodhyd.2014.03.011

Yang, M., Liu, F., Tang, C.H., 2013. Properties and microstructure of transglutaminase-set soy protein-stabilized emulsion gels. Food Res. Int. 52, 409–418. https://doi.org/10.1016/j.foodres.2011.11.012

Yin, T., Park, J.W., Xiong, S., 2015. Physicochemical properties of nano fish bone prepared by wet media milling. LWT - Food Sci. Technol. 64, 367–373. https://doi.org/10.1016/j.lwt.2015.06.007

Yuan, Y.J., Velev, O.D., Chen, K., Campbell, B.E., Kaler, E.W., Lenhoff, A.M., 2002. Effect of pH and Ca2+-induced associations of soybean proteins. J. Agric. Food Chem. 50, 4953–4958. https://doi.org/10.1021/jf025582d

Zeeb, B., Grossmann, L., Weiss, J., 2016. Accessibility of Transglutaminase to Induce Protein Crosslinking in Gelled Food Matrices - Impact of Membrane Structure. Food Biophys. 11, 176–183. https://doi.org/10.1007/s11483-016-9428-5

Zhang, J., Liang, L., Tian, Z., Chen, L., Subirade, M., 2012. Preparation and in vitro evaluation of calcium-induced soy protein isolate nanoparticles and their formation mechanism study. Food Chem. 133, 390–399. https://doi.org/10.1016/J.FOODCHEM.2012.01.049

Zhou, J.Z., Zhang, H., Gao, L., Wang, L., Qian, H.F., 2015. Influence of pH and ionic strength on heat-induced formation and rheological properties of cottonseed protein gels. Food Bioprod. Process. 96, 27–34. https://doi.org/10.1016/j.fbp.2015.06.004

Appendices

Effects of ball milling on the structural, thermal, and rheological properties of oat bran protein flour

Kurnia Ramadhan[a, b, *]

kurnia.ramadhan@nottingham.ac.uk

Tim J. Foster[a]

[a]Division of Food Sciences, University of Nottingham, Sutton Bonington Campus, Leicestershire LE12 5RD, United Kingdom

[b]Department of Food Technology, Universitas Bakrie, Jakarta 12920, Indonesia

*Corresponding author. Division of Food Sciences, University of Nottingham, Sutton Bonington Campus, Leicestershire LE12 5RD, United Kingdom.

Abstract

Oat bran protein flour (OBPF), containing protein, starch, and lipid as major constituents, was ball milled and subsequently evaluated on structural conformation, thermal properties, particle size distributions, and rheological properties. Prior to ball milling, characterisation of OBPF were conducted by means of Fourier transform infrared (FTIR) spectroscopy and differential scanning calorimetry (DSC) showing the existence of aggregated protein and starch-lipid complexes as predominant constituents of OBPF. Ball milling altered structural conformations of both protein and starch. Moreover, increase of ball milling time gradually decreased the transition enthalpy changes of amylose-lipid complexes upon heating which can be related to disruption of amylose-lipid complexes helical structure. Ball milling at higher speed resulted to smaller average particle size distributions of OBPF. Dynamic mechanical spectra of concentrated dispersions containing ball milled OBPF exhibited lower storage (G′) and loss (G″) moduli compared to control sample due to reduced particles volume packing. Moduli-frequency sweep data satisfactory fitted the Power Law's model.

Keywords: Oat protein; FTIR spectroscopy; DSC; Amylose-lipid complex; Dispersion

1 Introduction

Interests in protein-rich foods are rising favoured by its health-promoting effects. The benefits of dietary protein intake has been associated with body weight management and maintenance of muscle mass and function (Deutz et al., 2014; Westerterp-Plantenga et al., 2017). The urge to search for alternative food protein sources have led to valorisation of underexploited plants and side stream agricultural products.

Oat bran is a by-product of oat flour milling and have been used as a fibre-enriching ingredient. Although oat bran contains abundance of protein, its full utilisation remains challenging. Enzymatic pre-treatment of oat bran thick cell walls is necessary to assist protein extraction, otherwise a highly alkaline pH is required to release protein that adversely affect the nutritional quality (Jodayree et al., 2012). Low solubility of oat protein in slightly acidic to neutral pH range also restrict its applicability for foods (Konak et al., 2014). In order to bridge the gap between the limitations and advantages of oat bran protein for utilisation in foods, a feasible separation technique has been introduced to obtain protein-enriched flour with low degree of purity (Sozer et al., 2017). The presence of protein, starch and lipid, as constituents of composite flour, are known contributing to the physicochemical properties and functionality of flour (Puncha-Arnon and Uttapap, 2013; Saleh, 2017).

Physical modification of food materials by means of ball milling has gained attention due to ability in changing functionality. The modified functionality can be attributed to alteration in structural conformation as found in ball milled starch and starch-enriched food materials (Dhital et al., 2011; Liu et al., 2011; Roa et al., 2014a). However, there are limited studies reporting the effects of ball milling on structural conformation changes in food proteins including whey and soy protein (Liu et al., 2017; Sun et al., 2015).

This present study aims to evaluate the alteration on structural conformation of chemical constituents within ball milled oat bran protein flour, and subsequently to extrapolate the conformational changes into the thermal and rheological properties of its dispersion. This study would provide useful insights to extend the utilisation of oat bran protein flour in food formulations.

2 Materials and methods

2.1 Materials

Oat bran protein flour (OBPF) was supplied by Tate & Lyle Oat Ingredients (Kimstad, Sweden) as a brand of PrOatein®. This material was in the form of coarse powder and declared to have ca. 94% dry matter containing 54% protein, 17% fat, 18% carbohydrate, and 2% fibre on a dry basis. This material was prepared from oat bran that have gone through enzymatic, thermal, and physical separation processes.

2.2 Elimination of lipid and starch

Elimination of lipid and reduction of starch were intended to provide a correct assignment of FTIR spectra bands and interpretation of thermal properties in the later analyses. Lipid were extracted using solvent in soxhlet apparatus as described by Pandey and Shrivastava (2017) with modifications. Two solvents with different polarity were used, i.e. hexane for the non-polar solvent, and isopropanol for the polar solvent. Defatted samples are addressed as NPDO for the hexane-defatted OBPF and PDO for the isopropanol-defatted OBPF. Protein extraction from defatted samples, i.e. NPDO and PDO, did not lead to reasonable protein yields for further analysis. Therefore, in this study, starch reduction was chosen to obtain a higher protein concentration. Starch reduction was conducted by dispersing and stirring the defatted samples into alkaline solution for 30 min as described by De Souza et al. (~~De Souza et al.,~~ 2016). The sample was then lyophilised to obtain dry powder and addressed as APDO.

2.3 Ball milling procedure

Ball milling was carried out by using Planetary Micro Mill (Pulverisette 7 classic line, FritschGmbH, Germany) as described by Abbaszadeh et al. (2014) with modifications. Two and a half grams of OBPF was put into 12 ml grinding bowl containing 6 Zirconium dioxide grinding balls. High speed milling was run at 800 revolutions per minute (rpm) for 15 min. The low speed milling was carried out at 200 rpm for 240 min. The applied milling cycle configuration was 5 min milling followed by 5 min rest to dissipate heat. Reversed milling directions were set to prevent ball slippage at both milling speeds.

2.4 Preparation of OBPF dispersions

OBPF dispersions (5%, 20%, and 30%-wt) were prepared by suspending the flour into distilled water as described by Roa et al. (2015)- with modifications. These concentrations were selected according to previous trials conducted with OBPF dispersions from 5% to 30%-wt. A dilute system (5%-wt) was selected to evaluate the particle size distributions, while the 20%-wt dispersion was subjected to thermal analysis for its flow-ability reason, and the 30%-wt dispersion was selected for rheological analysis to avoid sedimentation.

2.5 Attenuated total reflectance – fourier transform infrared (ATR-FTIR) spectroscopy

The infrared spectra were obtained by using a Bruker Tensor 27 System (Bruker Optik GmbH, Ettlingen, Germany) equipped with diamond Attenuated Total Reflection (ATR) crystal and operated using OPUS software version 7.2.139.1294. The tests were performed at ambient temperature. The open-air background test was run prior to sample measurement. Approximately 50 mg of dry sample was placed into contact with the diamond ATR crystal and sample holder. Each absorbance measurement was conducted under 128 scans with 4 cm^{-1} resolutions. The presented infrared spectra were obtained as a mean from three measurements of duplicate samples that have undergone normalisation and baseline correction. Height of peaks were determined by calculating the absorption intensity differences between peak and its own baseline. Peak height ratio of selected absorption bands was used to quantify the infrared spectral changes. The amide I band, i.e. ~1630 cm^{-1}, was selected as reference band in evaluating spectral changes due to elimination of lipids and starch. Calculation of absorbance intensity ratio ~997 to ~1022 cm^{-1} was used to assess structural conformation changes on starch as described by Liu et al. (2011). The use of second derivative spectra was intended to resolve the overlapping bands both in amide and saccharide regions (Fig. 3). The assignment of protein secondary structure within amide I band referred to a study reported by Tang and Ma (2009). Further processing of infrared spectra was conducted using Spectragryph optical spectroscopy software version 1.0.2 (https://www.effemm2.de/spectragryph/).

2.6 Micro-differential scanning calorimetry

Scanning calorimetry was performed in a Micro-Differential Scanning Calorimeter III (Setaram Instrumentation, France). About 800 mg of dispersions containing 20%wt solid sample was transferred into hermetically sealed sample vial made from hastelloy, while similar weight of deionized water was used as reference. Heating-cooling processes were performed in two cycles from 20 to 120 °C at a rate of 1 °C min^{-1}. Measurement was run in duplicate for each sample. The heat flow curves were processed using Calisto Processing software v1.43 (AKTS, Switzerland) to obtain the maximum heat absorption temperatures (T_m) and the transition enthalpy changes (ΔH).

2.7 Particle size distributions

Particle size and size distributions were measured based on the principles of light scattering using LS13320 Laser Diffraction Particle Size Analyzer (Beckman Coulter, High Wycombe, UK). A dispersion of 5% OBPF in distilled water was pipetted into a liquid module sample cell. The measurement was run for 60 s under following conditions: Fraunhofer theory was used as optical model treating particles in spherical approximation, refractive indexes of dispersant and sample were 1.33 and 1.6 respectively. The particle size was determined by the volume-weighted mean diameter size. Each measurement was run in duplicate.

2.8 Rheology

~~Structuring~~Rheological properties of OBPF dispersions was evaluated using ~~rheological analysis. Small deformation tests of oat dispersion were conducted using~~ a stress-controlled rheometer (Physica MCR 301, Anton Paar, Austria) with a serrated parallel-plate geometry of 50 mm diameter and 1 mm gap. The linear viscoelastic region (LVR) was determined by strain amplitude sweep tests at a fixed angular frequency of 10 rad s^{-1}. The temperature sweep tests were performed at a constant angular frequency of 10 rad s^{-1} and a strain amplitude of 0.1%. A programmed heating-cooling process was used, i.e. heating from 20 to 100 °C, temperature hold at 100 °C for 10 min, and cooling from 100 to 20 °C with heating and cooling rate of 5 °C min^{-1}. Prevention of evaporation and temperature gradient were taken into account by using low-viscosity mineral oil and a peltier-controlled hood. Subsequently, frequency sweep tests were carried out from 0.5 to 50 rad s^{-1} at constant strain amplitude of 0.1%. Frequency sweep data were correlated by means of the Power Law model using the following equations:

$$G' = a'\omega^{b'} \quad (1)$$

$$G'' = a''\omega^{b''} \quad (2)$$

where the ω, G′, and G″~~, and~~ are the angular frequency, storage, and loss modulus respectively, and the a', a'', b', and b'' are the intercepts and slopes of corresponding fitting parameters. Each test was run in duplicate.

3 Results and discussion

3.1 Assignment of OBPF chemical constituent in infrared spectra

Infrared spectra of OBPF are illustrated in Fig. 1 showing chemical-bond vibrations of mixture system. Protein as the primary constituent can be traced by the presence of amide A, I, and II absorption bands. Amide A vibrations occurred at higher wavenumber and is contributed by N-H groups stretching vibrations. Amide I and II are predominantly induced by C=O and C-N stretching vibrations, and appear as two consecutive absorption signals between 1700 and 1500 cm^{-1} (Barth, 2007). The Amide A, I, and II absorption bands of OBPF appear at wavenumbers 3271, 1630, and 1517 cm^{-1} respectively. Evaluation of amide I region can provide useful information on protein secondary structure conformation which will be discussed in the later section.

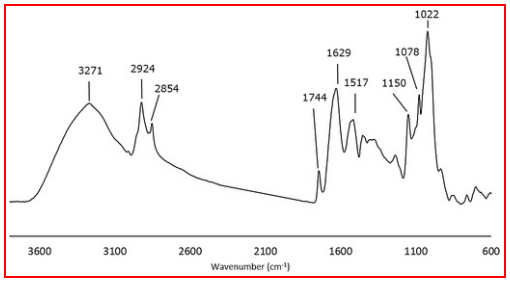

Fig. 1 Typical infrared spectra of oat bran protein flour.

alt-text: Fig. 1

Infrared spectral changes as affected by lipids and starch eliminations are presented in Table 1. Removal of neutral lipids by non-polar solvent drastically decreased the absorption signal at ~2924, ~2854, and ~1744 cm^{-1}. However, the use of polar solvent diminished the second peaks and left small signal of the third peak. This might indicate the asymmetric stretching vibrations of C-H at ~2924 cm^{-1} is not solely contributed by of lipid alone, but also from other major chemical constituents. The peak at ~2854 cm^{-1} could be uniquely assigned to -CH_2- symmetric stretching of fatty acid chains. The peak ~1744 cm^{-1} corresponds to carbonyl (C=O) stretching vibration identifying the ester functional group of lipid (Cerqueira et al., 2012). Oats contain higher amounts of polar lipids compared to other cereals, such as glycolipids and monoacyl lipids (Doehlert et al., 2010).

Table 1 Infrared spectral changes on selected bands of OBPF and its derived fractions.

alt-text: Table 1

Sample	Peak height ratio relative to peak at ~1630 cm^{-1}					
	~2924 cm^{-1}	~2854 cm^{-1}	~1744 cm^{-1}	~1150 cm^{-1}	~1078 cm^{-1}	~1022 cm^{-1}
OBPF	0.55 ± 0.04	0.11 ± 0.02	0.32 ± 0.02	0.67 ± 0.05	0.49 ± 0.06	0.94 ± 0.14

NPDO	0.31 ± 0.02	0.02 ± 0.00	0.16 ± 0.08	0.69 ± 0.06	0.53 ± 0.06	0.92 ± 0.03
PDO	0.29 ± 0.01	N/A	0.08 ± 0.01	0.79 ± 0.08	0.54 ± 0.08	1.02 ± 0.15
APDO	0.21 ± 0.02	N/A	0.05 ± 0.01	0.48 ± 0.06	0.37 ± 0.04	0.61 ± 0.12

Abbreviations: OBPF (Oat bran protein flour), NPDO (Non polar solvent defatted OBPF), PDO (Polar solvent defatted OBPF), APDO (Alkaline exposed PDO).

Saccharide region of infrared spectra ranges from 1200 to 900 cm^{-1}. Three intense absorption bands at 1150, 1078, and 1022 cm^{-1} confirming typical vibration characteristics of C-O, C-C, O-H bonds and asymmetric stretching of C-O-C glycosidic bonds within the starch (Liu et al., 2011; Roa et al., 2014b). The strongest absorption band at 1022 cm^{-1} indicated predominant disordered conformational structure of OBPF starch that have gone through thermal treatment during production. This peak contains shoulder at the lower wavenumber that possibly indicate small amount of crystalline conformation. Alkaline exposure treatment dramatically decreased absorbance intensity of the three above mentioned peaks, indicating irreversible solubilisation of starch. This confirms the correct assignment for starch within infrared spectra and can be used to evaluate structural conformations in the later section.

3.2 Thermal properties of OBPF dispersions

The DSC thermograms and the corresponding thermal transition peak temperature and enthalpy changes of OBPF dispersions are presented in Fig. 2 and Table 2 respectively. Upon the first heating, a broad endothermic peak appeared at c.a. 90 °C and consequently shifted to a higher temperature when reheated. Whereas upon cooling, a sharp exothermic peak was observed at c.a. 74 °C in either cycles. The ΔH values was 1.7 J g^{-1} on the first heating and subsequently decrease over the following cycles. The use of polar solvent greatly reduced ΔH values due to elimination of higher amounts of lipids as confirmed by FTIR study. However, calorimetry scanning of extracted lipids did not show any thermal transition events (data not shown). Starch solubilisation by alkaline exposure further decreased the ΔH values. It shows that the ΔH values are more dependent to the starch and lipids rather than the protein.

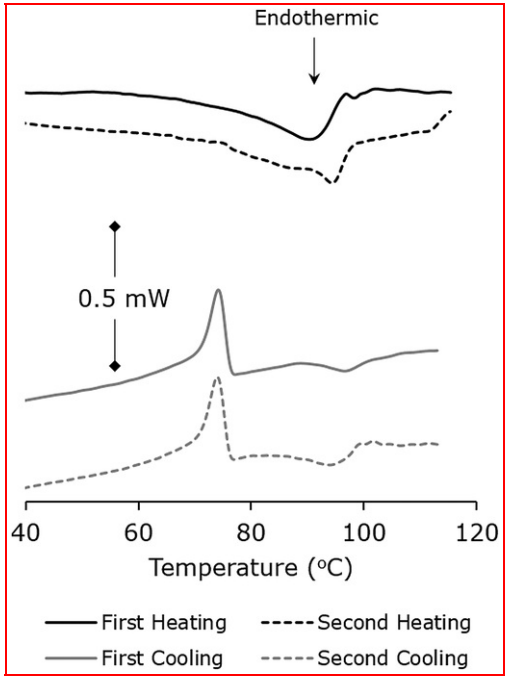

Fig. 2 DSC thermogram of OBPF dispersions upon heating-cooling cycles.

alt-text: Fig. 2

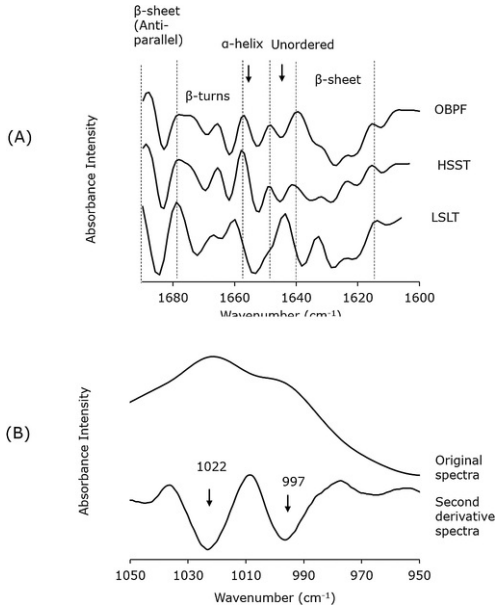

Fig. 3 (A) Second derivative spectra at amide I region of OBPF prior to and after ball milling; (B) original and second derivative spectra of OBPF at saccharide region. For abbreviations see Table 3.

alt-text: Fig. 3

Table 2 Thermal transition peak temperatures (T_p) and enthalpy changes (ΔH) of OBPF dispersions and its derived fractions.

alt-text: Table 2

Sample	First heating		First cooling		Second heating		Second cooling	
	T_p (°C)	ΔH (J g^{-1} solid)	T_p (°C)	ΔH (J g^{-1} solid)	T_p (°C)	ΔH (J g^{-1} solid)	T_p (°C)	ΔH (J g^{-1} solid)
OBPF	90.63 ± 0.32	1.70 ± 0.21	74.14 ± 0.04	−1.02 ± 0.04	94.42 ± 0.10	1.01 ± 0.02	73.97 ± 0.04	−0.94 ± 0.02
NPDO	91.12 ± 0.74	0.94 ± 0.18	74.49 ± 0.05	−0.84 ± 0.02	94.98 ± 0.08	0.72 ± 0.13	74.34 ± 0.03	−0.72 ± 0.07
PDO	90.41 ± 0.59	0.76 ± 0.02	73.80 ± 0.25	−0.64 ± 0.04	94.07 ± 0.16	0.61 ± 0.04	73.73 ± 0.25	−0.53 ± 0.08
APDO	92.07 ± 0.51	0.48 ± 0.01	72.28 ± 0.41	−0.32 ± 0.02	92.76 ± 0.16	0.26 ± 0.02	71.88 ± 0.61	−0.26 ± 0.05

For abbreviations see Table 1.

The reversible thermal events at very high temperature upon heating, i.e. 90 °C, can be associated to the characteristics of starch-lipid complexes in the presence of protein contained in thermally treated foods as found in previous studies (De Pilli et al., 2015; Moisio et al., 2015; Wang et al., 2017). When the heated starch is cooled back in the presence of lipid, the amylose recrystallize and form complexes with lipids by the inclusion of fatty acid chain into helical cavity (Tufvesson et al., 2003). The amount of amylose-lipid complexes is the major factor determining the ΔH value as proposed by Kawai et al. (2012). Interestingly, melting temperature of starch-lipid complexes slightly increased upon second heating hence indicating a more thermally-stable structure as a result of complexes reformation in more ordered structure.

3.3 Ball milling effects on structural conformation of OBPF chemical constituents

Ball milling affected structural conformation changes on both protein and starch in solid-state as illustrated in Fig. 3 and Table 3. Prior to ball milling, secondary structure of protein prominently presented as β-sheets structure and some minor helical structures. This result demonstrated a higher composition in β-sheets compared to previous study on oat protein isolate secondary structure at low moisture (Liu et al., 2009). The explanation for this condition is

the protein contained in OBPF has been thermally treated during the production, hence most likely in denatured and aggregated form. The β-sheet structures have been associated with hydrophobic and aggregated protein (Maltais et al., 2008; ~~Nikolaus~~ Wellner et al., 2004; Tang and Ma, 2009). However, other study on oat protein conformation in aqueous dispersion showed lower relative amount of β-sheets as the major structure (Jing et al., 2016). Secondary structure of protein in dispersion is a result from peptide-solvent interactions in aqueous environment, whereas at low moisture the peptide-peptide interactions are predominant factor due to dense packing in a solid environment.

Table 3 Ball milling effects on protein and starch structural conformation.

alt-text: Table 3

Sample	Relative area of protein secondary structure bands (%)		Starch
	Total β-sheets and β-turns (%)	Total α-helix and random coil (%)	~997/~1022 cm^{-1} ratio
OBPF	88.03 ± 2.69	11.97 ± 2.69	0.63 ± 0.02
HSST10	82.33 ± 2.68	17.67 ± 2.68	0.57 ± 0.06
HSST20	82.53 ± 1.02	17.47 ± 1.02	0.56 ± 0.05
HSST30	79.85 ± 0.61	20.15 ± 0.61	0.50 ± 0.02
LSLT120	80.96 ± 4.39	19.04 ± 4.39	0.56 ± 0.04
LSLT240	81.88 ± 1.38	18.12 ± 1.38	0.49 ± 0.04
LSLT360	80.33 ± 6.95	19.67 ± 6.95	0.38 ± 0.04

Abbreviations: OBPF (Oat bran protein flour), HSST10, 20, and 30 (Ball milled OBPF at high speed, i.e. 800 rpm for short time, i.e. 10, 20, or 30 min), LSLT120, 240, and 360 (Ball milled OBPF at low speed, i.e. 200 rpm for long time, i.e. 120, 240, or 360 min).

Ball milling gradually increased relative amount of helical conformations in expense of β-sheet structures. Longer ball milling time, regardless the applied speed, demonstrated greater effect on protein conformational changes due to simultaneous mechanical impact. Similar result of increasing α -helix and decreasing β-sheet structure after ball milling soy protein isolate has been reported (Liu et al., 2017). Ball milling involves high pressure, shear force, and air contact that might cause rearrangement of aggregated protein secondary structure as suggested by Sun et al. (2015). Among the protein fractions and sub-units, low molecular weight proteins are the most susceptible to disruptions caused by ball milling (Thanatuksorn et al., 2009).

Evaluation of ball milling effects on starch conformation are presented in Table 3. A higher ratio of peak ~997 to ~1022 indicated small degree of ordered structure within starch conformation. The presence of amylose-lipid complexes has been reported to consists of some starch crystalline order (Kawai et al., 2012). In this study, longer ball milling time greatly reduced ordered structure of starch conformation. This ball milling effects on starch has been extensively studied in previous reports known by disruption effects on helical structures (Liu et al., 2011; Roa et al., 2015).

3.4 Ball milling effects on thermal properties of OBPF dispersions

Thermal properties of OBPF prior to and after ball milling are presented in Table 4. Ball milling did not greatly affect the transition peak temperature, whereas the enthalpy values gradually decreased as the milling time increased, regardless the applied speed. Decreasing enthalpy values can be interpreted as the decrease on amounts of amylose-lipid complexes. This is confirmed by further loss of crystallinity provided by FTIR spectroscopy study. Simultaneous mechanical impact during ball milling disrupted the helical structure of amylose, hence disintegrated the amylose-lipid complexes. Ball milled samples did not differ in transition temperature peak upon the second heating showing thermal behaviour remain unchanged.

Table 4 Thermal transition peak temperatures and enthalpy changes of OBPF dispersions affected by ball milling.

alt-text: Table 4

Sample	First heating		First cooling		Second heating		Second cooling	
	T_p (°C)	ΔH (J g^{-1} solid)	T_p (°C)	ΔH (J g^{-1} solid)	T_p (°C)	ΔH (J g^{-1} solid)	T_p (°C)	ΔH (J g^{-1} solid)

OBPF	90.63 ± 0.32	1.70 ± 0.21	74.14 ± 0.04	−1.02 ± 0.04	94.42 ± 0.10	1.01 ± 0.02	73.97 ± 0.04	−0.94 ± 0.02
HSST30	90.50 ± 0.26	1.19 ± 0.14	73.72 ± 0.09	−0.78 ± 0.07	94.10 ± 0.01	0.65 ± 0.12	73.63 ± 0.10	−0.51 ± 0.01
LSLT360	91.20 ± 0.34	0.85 ± 0.07	74.04 ± 0.09	−0.77 ± 0.07	94.52 ± 0.07	0.66 ± 0.10	73.96 ± 0.07	−0.60 ± 0.04

For abbreviations see Table 3.

3.5 Ball milling effects on particle size distribution

Particle size distributions of OBPF prior to and after ball milling are presented in Fig. 4 and Table 5. Prior to ball milling, wide range of particle size distributions were observed. The D_{10}, D_{50}, and D_{90} values represent 10, 50, and 90% particle size distributions within the dispersed sample, whereas the $D_{(4,3)}$ show average particle sizes. Ball milling at high speed reduced the particle size distributions to about quarter of initial values, e.g. from 116.45 ± 21.85 to 27.67 ± 0.93 μm. However, low speed ball milling could reduce to only about half of initial even after 360 min milling duration. This might be explained that rotational speed is a major factor to cause particle breakage during ball milling as suggested by Yin et al. (2015).

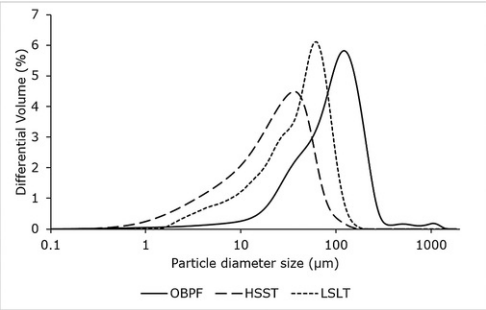

Fig. 4 Volume-weighted particle size distributions of OBPC prior to and after ball milling. For abbreviations see Table 3.

alt-text: Fig. 4

Table 5 Particle size distributions OBPF prior to and after ball milling.

alt-text: Table 5

Sample	$D_{(4,3)}$ (μm)	D_{10} (μm)	D_{50} (μm)	D_{90} (μm)
OBPF	116.45 ± 21.85	27.33 ± 0.80	98.11 ± 5.79	203.50 ± 21.92
HSST	27.67 ± 0.93	4.09 ± 0.10	23.22 ± 0.47	56.67 ± 1.66
LSLT	49.33 ± 0.23	10.01 ± 0.86	46.88 ± 0.36	91.55 ± 0.05

For abbreviations see Table 3.

3.6 Ball milling effects on viscoelastic properties of OBPF dispersions

Fig. 5 illustrated the viscoelastic properties of OBPF dispersions affected by ball milling and temperature changes. Ball milled samples at higher speed exhibited the lowest moduli at the same applied shear. Since the dispersions contain same weight fraction of samples, the volume packing fraction of HSST and LTST dispersions were lower, and hence decreased the storage moduli.

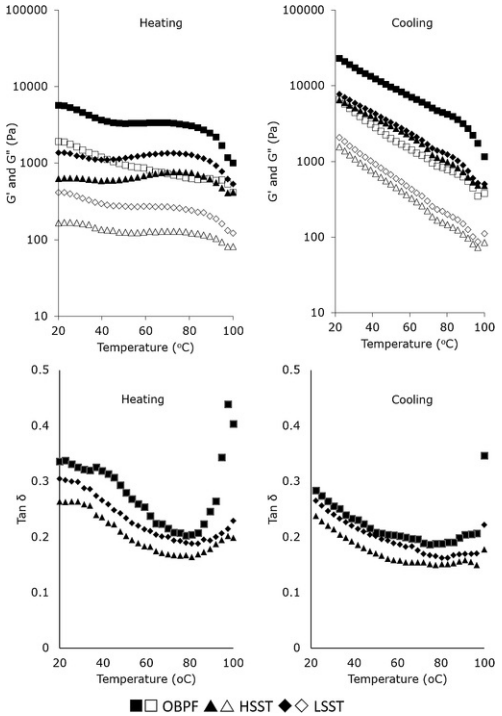

Fig. 5 Storage (filled) and loss (open) moduli (top), and tangent of phase angle (bottom) of OBPC concentrated dispersions prior to and after ball milling over changing temperatures. For abbreviations see Table 3.

alt-text: Fig. 5

Temperature effects on moduli were observed in both heating and cooling cycles. Moduli decreases occurred below 40 °C seems to be the effects of increasing particle mobility since there were no thermal events recorded by scanning calorimetry within this temperature range. On the other hand, further decrease on moduli when temperature approached 90 °C indicate the melting of starch-lipid complexes contained in dispersions. Noticeable differences in melting behaviour of ball milled samples were observed using the tangent of phase angle (tan δ). Dispersions containing ball milled samples showed lower tan δ when reach the melting temperature that might due to the lower enthalpy changes.

The moduli of dispersions increased steadily upon cooling back to room temperature due to the recrystallisation of melted particles. Moreover, cooled dispersions reached higher moduli compared to initial values prior to heating. This might indicate the connectivity between particles were built during cooling which most likely contributed by starch.

Fig. 6 illustrated the frequency-dependency of OBPF concentrated dispersions. The moduli increased with increase of angular frequency. Effects of ball milling were observed in the fitting parameters of frequency sweep data, presented in Table 6. Decreases in intercepts are consistent with the decreases of G′ and G″ due to particle volume packing effects. Ball milling also increased the slopes of moduli-frequency curves which revealed a weaker gel-like structure. As the particle volume packing decreases, solvent-particles interactions increase and inhibit the particle-particle interactions in building the structure. This is agreed with previous study on other flour dispersions (Ahmed et al., 2014). Both G′ and G″ of all samples were satisfactory fitted to Power Law's model, shown by the R^2 values close to 1.

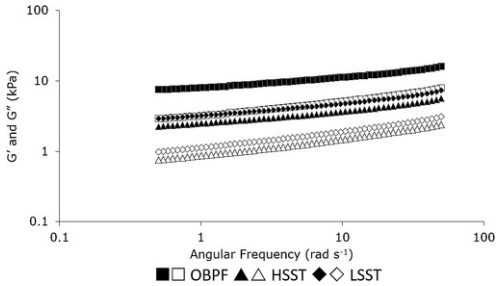

Fig. 6 Storage (filled) and loss (open) moduli of OBPC concentrated dispersions prior to and after ball milling over changing angular frequencies. For abbreviations see Table 3.

alt-text: Fig. 6

Table 6 Parameters of moduli-frequency fitting based on the Power Law model.

alt-text: Table 6

Sample	G′			G″		
	a' (kPa)	b'	R^2	a' (kPa)	b'	R^2
OBPF	7.94 ± 0.93	0.16 ± 0.00	0.986 ± 0.008	3.18 ± 0.17	0.21 ± 0.01	0.992 ± 0.004
HSST	2.44 ± 0.11	0.19 ± 0.05	0.985 ± 0.005	0.85 ± 0.35	0.24 ± 0.02	0.994 ± 0.002
LSLT	3.15 ± 0.67	0.19 ± 0.04	0.988 ± 0.002	1.11 ± 0.02	0.24 ± 0.02	0.994 ± 0.003

For abbreviations see Table 3.

4 Conclusions

Major constituent of OBPF were observed in the form of aggregated proteins and starch-lipid complexes. Ball milling altered the structural conformations of protein and starch, and reduced the enthalpy changes of starch-lipid complexes melting properties. Higher speed ball milling reduced particle size distributions to about quarter of initial values, e.g. from 116.45 ± 21.85 to 27.67 ± 0.93 μm, led to lower particle volume packing, and hence decreased the mechanical moduli of dispersions. Subsequent heating-cooling processes of OBPF dispersions allowed the starch to build a stronger networked structure. Therefore, the starch contained in OBPF plays as important constituent in influencing the structure of dispersion.

Acknowledgments

The first author would like to express gratitude to the Ministry of Research, Technology, and Higher Education of the Republic of Indonesia for the financial support.

References

Abbaszadeh A., MacNaughtan W. and Foster T.J., The effect of ball milling and rehydration on powdered mixtures of hydrocolloids, *Carbohydr. Polym.* **102**, 2014, 978–985, https://doi.org/10.1016/j.carbpol.2013.10.020.

Ahmed J., Al-Foudari M., Al-Salman F. and Almusallam A.S., Effect of particle size and temperature on rheological, thermal, and structural properties of pumpkin flour dispersion, *J. Food Eng.* **124**, 2014, 43–53, https://doi.org/10.1016/j.jfoodeng.2013.09.030.

Barth A., Infrared spectroscopy of proteins, *Biochim. Biophys. Acta - Bioenerg.* **1767**, 2007, 1073–1101, https://doi.org/10.1016/j.bbabio.2007.06.004.

Cerqueira M.A., Souza B.W.S., Teixeira J.A. and Vicente A.A., Effect of glycerol and corn oil on physicochemical properties of polysaccharide films – a comparative study, *Food Hydrocoll.* **27**, 2012, 175–184, https://doi.org/10.1016/j.foodhyd.2011.07.007.

De Pilli T., Legrand J., Derossi A. and Severini C., Effect of proteins on the formation of starch-lipid complexes during extrusion cooking of wheat flour with the addition of oleic acid, *Int. J. Food Sci. Technol.* **50**, 2015,

515–521, https://doi.org/10.1111/ijfs.12698.

De Souza D., Sbardelotto A.F., Ziegler D.R., Marczak L.D.F. and Tessaro I.C., Characterization of rice starch and protein obtained by a fast alkaline extraction method, *Food Chem.* **191**, 2016, 36–44, https://doi.org/10.1016/j.foodchem.2015.03.032.

Deutz N.E.P., Bauer J.M., Barazzoni R., Biolo G., Boirie Y., Bosy-Westphal A., Cederholm T., Cruz-Jentoft A., Krznariç Z., Nair K.S., Singer P., Teta D., Tipton K. and Calder P.C., Protein intake and exercise for optimal muscle function with aging: recommendations from the ESPEN expert group, *Clin. Nutr.* **33**, 2014, 929–936, https://doi.org/10.1016/j.clnu.2014.04.007.

Dhital S., Shrestha A.K., Flanagan B.M., Hasjim J. and Gidley M.J., Cryo-milling of starch granules leads to differential effects on molecular size and conformation, *Carbohydr. Polym.* **84**, 2011, 1133–1140, https://doi.org/10.1016/j.carbpol.2011.01.002.

Doehlert D.C., Moreau R.A., Welti R., Roth M.R. and McMullen M.S., Polar lipids from oat kernels, *Cereal Chem.* **87**, 2010, 467–474, https://doi.org/10.1094/CCHEM-04-10-0060.

Jing X., Yang C. and Zhang L., Characterization and analysis of protein structures in oat bran, *J. Food Sci.* **81**, 2016, C2337–C2343, https://doi.org/10.1111/1750-3841.13445.

Jodayree S., Smith J.C. and Tsopmo A., Use of carbohydrase to enhance protein extraction efficiency and antioxidative properties of oat bran protein hydrolysates, *Food Res. Int.* **46**, 2012, 69–75, https://doi.org/10.1016/j.foodres.2011.12.004.

Kawai K., Takato S., Sasaki T. and Kajiwara K., Complex formation, thermal properties, and in-vitro digestibility of gelatinized potato starch-fatty acid mixtures, *Food Hydrocoll.* **27**, 2012, 228–234, https://doi.org/10.1016/j.foodhyd.2011.07.003.

Konak Ü.İ., Ercili-Cura D., Sibakov J., Sontag-Strohm T., Certel M. and Loponen J., CO2-defatted oats: solubility, emulsification and foaming properties, *J. Cereal Sci.* **60**, 2014, 37–41, https://doi.org/10.1016/j.jcs.2014.01.013.

Liu B., Wang H., Hu T., Zhang P., Zhang Z., Pan S. and Hu H., Ball-milling changed the physicochemical properties of SPI and its cold-set gels, *J. Food Eng.* **195**, 2017, 158–165, https://doi.org/10.1016/j.jfoodeng.2016.10.006

Liu G., Li J., Shi K., Wang S., Chen J., Liu Y. and Huang Q., Composition, secondary structure, and self-assembly of oat protein isolate, *J. Agric. Food Chem.* **57**, 2009, 4552–4558, https://doi.org/10.1021/jf900135e.

Liu T.Y., Ma Y., Yu S.F., Shi J. and Xue S., The effect of ball milling treatment on structure and porosity of maize starch granule, *Innov. Food Sci. Emerg. Technol.* **12**, 2011, 586–593, https://doi.org/10.1016/j.ifset.2011.06.009

Maltais A., Remondetto G.E. and Subirade M., Mechanisms involved in the formation and structure of soya protein cold-set gels: a molecular and supramolecular investigation, *Food Hydrocoll.* **22**, 2008, 550–559, https://doi.org/10.1016/j.foodhyd.2007.01.026.

Moisio T., Forssell P., Partanen R., Damerau A. and Hill S.E., Reorganisation of starch, proteins and lipids in extrusion of oats, *J. Cereal Sci.* **64**, 2015, 48–55, https://doi.org/10.1016/j.jcs.2015.04.001.

~~Wellner Nikolaus, Clare Mills E.N., Brownsey Geoff, Wilson Reginald H., Brown Neil, Freeman Jacqueline, Halford Nigel G., Shewry Peter R. and Belton P.S., Changes in Protein Secondary Structure during Gluten Deformation Studied b Dynamic Fourier Transform Infrared Spectroscopy, 2004https://doi.org/10.1021/BM049584D~~ (This reference needs to be moved to the latter order).

Pandey R. and Shrivastava S.L., Comparative evaluation of rice bran oil obtained with two-step microwave assisted extraction and conventional solvent extraction, *J. Food Eng.* **218**, 2017, 106–114, https://doi.org/10.1016/j.jfoodeng.2017.09.009.

Puncha-Arnon S. and Uttapap D., Rice starch vs. rice flour: differences in their properties when modified by heat-moisture treatment, *Carbohydr. Polym.* **91**, 2013, 85–91, https://doi.org/10.1016/j.carbpol.2012.08.006.

Roa D.F., Baeza R.I. and Tolaba M.P., Effect of ball milling energy on rheological and thermal properties of amaranth flour, *J. Food Sci. Technol.* **52**, 2015, 8389–8394, https://doi.org/10.1007/s13197-015-1976-z.

Roa D.F., Santagapita P.R., Buera M.P. and Tolaba M.P., Ball milling of amaranth starch-enriched fraction. Changes on particle size, starch crystallinity, and functionality as a function of milling energy, *Food Bioprocess Technol.* **7**, 2014a, 2723–2731, https://doi.org/10.1007/s11947-014-1283-0.

Roa D.F., Santagapita P.R., Buera M.P. and Tolaba M.P., Amaranth milling strategies and fraction characterization by FT-IR, *Food Bioprocess Technol.* **7**, 2014b, 711–718, https://doi.org/10.1007/s11947-013-1050-7.

Saleh M.I., Protein-starch matrix microstructure during rice flour pastes formation, *J. Cereal Sci.* **74**, 2017, 183–186, https://doi.org/10.1016/j.jcs.2017.02.005.

Sozer N., Nordlund E., Ercili-Cura D. and Poutanen K., Cereal side-streams as alternative protein sources, *Cereal Foods World* **62**, 2017, 132–137, https://doi.org/10.1094/CFW-62-4-0132.

Sun C., Liu R., Wu T., Liang B., Shi C. and Zhang M., Effect of superfine grinding on the structural and physicochemical properties of whey protein and applications for microparticulated proteins, *Food Sci. Biotechnol.* **24**, 2015, 1637–1643, https://doi.org/10.1007/s10068-015-0212-y.

Tang C.-H. and Ma C.-Y., Effect of high pressure treatment on aggregation and structural properties of soy protein isolate, *LWT - Food Sci. Technol.* **42**, 2009, 606–611, https://doi.org/10.1016/j.lwt.2008.07.012.

Thanatuksorn P., Kawai K., Kajiwara K. and Suzuki T., Effects of ball-milling on the glass transition of wheat flour constituents, *J. Sci. Food Agric.* **89**, 2009, 430–435, https://doi.org/10.1002/jsfa.3463.

Tufvesson F., Wahlgren M. and Eliasson A.C., Formation of amylose-lipid complexes and effects of temperature treatment - Part 1, *Monoglycerides. Starch/Stärke* **55**, 2003, 61–71, https://doi.org/10.1002/star.200390018.

Wang S.S., Zheng M., Yu J., Wang S.S. and Copeland L., Insights into the formation and structures of starch-protein-lipid complexes, *J. Agric. Food Chem.* **65**, 2017, 1960–1966, https://doi.org/10.1021/acs.jafc.6b05772.

(Please move this reference to this order:
Wellner N., Mills E.N.C., Brownsey G., Wilson R.H., Brown N., Freeman J., Halford N.G., Shewry P.R. and Belton P.S., Changes in protein secondary structure during gluten deformation studied by dynamic Fourier transform infrared spectroscopy, *Biomacromolecules*, ***6***, 2005, 255-261, https://doi.org/10.1021/bm049584d)Westerterp-Plantenga M.S., Lemmens S.G. and Westerterp K.R., Dietary Protein – its Role in Satiety, Energetics, Weight Loss and Health, 2017https://doi.org/10.1017/S0007114512002589.

Yin T., Park J.W. and Xiong S., Physicochemical properties of nano fish bone prepared by wet media milling, *LWT - Food Sci. Technol.* **64**, 2015, 367–373, https://doi.org/10.1016/j.lwt.2015.06.007.

Highlights

- Ball milling alters structural conformations of aggregated proteins and starch-lipid complexes.
- Mechanical impact caused by ball milling disrupted the ordered structure of amylose-lipid complexes.
- Changes in mechanical moduli of dispersions are mainly contributed by differences in particle size distributions ~~after ball milling~~.

Queries and Answers

Query: Please check the address for the corresponding author that has been added here, and correct if necessary.
Answer: Corresponding author's address is correct

Query: Could you please provide the grant number for Ministry of Research, Technology, and Higher Education, if any?
Answer: There is no grant number available. The financial support is provided in the form of PhD scholarship.

Query: Symbols “*, †, ‡, §” has been designated to the authors “Nikolaus Wellner, E. N. Clare Mills, Geoff Brownsey, Reginald H. Wilson, Neil Brown, Jacqueline Freeman, Nigel G. Halford, Peter R. Shewry and, Belton, P.S.” were doesn’t have any significance and it has been deleted. Kindly check and correct if necessary.
Answer: This reference needs to be moved to the latter order and rewritten as:
Wellner N., Mills E.N.C., Brownsey G., Wilson R.H., Brown N., Freeman J., Halford N.G., Shewry P.R. and Belton P.S., Changes in protein secondary structure during gluten deformation studied by dynamic Fourier transform infrared spectroscopy, *Biomacromolecules*, ***6***, 2005, 255-261, https://doi.org/10.1021/bm049584d

Query: Highlights should only consist of “125” characters per bullet point, including spaces. The highlights provided are too long; please edit them to meet the requirement.
Answer: The words within the third bullet point have been reduced.

Query: Please confirm that given names and surnames have been identified correctly and are presented in the desired order and please carefully verify the spelling of all authors’ names.
Answer: Yes

Query: Your article is registered as belonging to the Special Issue/Collection entitled “FSD 2016”. If this is NOT correct and your article is a regular item or belongs to a different Special Issue please

contact a.anwerbasha@elsevier.com immediately prior to returning your corrections.

Answer: Yes

Understanding structural differences of soy protein isolate dispersions at multiple length scales that contribute to viscoelastic behaviour

Journal:	*European Food Research and Technology*
Manuscript ID	EFRT-20-0018
Manuscript Type:	Original paper
Date Submitted by the Author:	05-Jan-2020
Complete List of Authors:	Ramadhan, Kurnia; University of Nottingham School of Biosciences, Division of Food, Nutrition, and Dietetics; Universitas Bakrie, Food Technology di Bari, Vincenzo; University of Nottingham School of Biosciences, Division of Food, Nutrition, and Dietetics Foster, Tim; University of Nottingham School of Biosciences, Division of Food, Nutrition, and Dietetics
Keywords:	soy protein, structural properties, insoluble particle, viscoelastic dispersion

Understanding structural differences of soy protein isolate dispersions at multiple length scales that contribute to viscoelastic behaviour

Kurnia Ramadhan [a,b,*] Vincenzo di Bari [a], and Tim J. Foster [a]

[a] *Division of Food, Nutrition, and Dietetics, School of Biosciences, University of Nottingham, Sutton Bonington Campus, Leicestershire LE12 5RD, United Kingdom*

[b] *Department of Food Technology, Universitas Bakrie, Jakarta 12920, Indonesia*

*Corresponding Author:

Email address: kurnia.ramadhan@nottingham.ac.uk or kurnia.ramadhan@bakrie.ac.id

ORCID iD: https://orcid.org/0000-0002-3991-3072

Abstract

This study aims to demonstrate the structural differences of several commercial and laboratory-prepared soy protein isolates (SPI) at multiple length scales, namely molecular level, mesoscopic, and macroscopic scales, that contribute to viscoelastic behaviour of their dispersions. Structural properties of SPI at the molecular level were elucidated by gel electrophoresis, micro-differential scanning calorimetry, and fourier transform infrared spectroscopy. The mesoscopic structural evaluation focused on quantification of soluble protein within SPI dispersions by means of bicinchoninic acid protein assay, and physical characterisation of their insoluble fraction, such as microscopic observation and particle size distribution. Rheological analyses were used to assess macroscopic structures of SPI dispersion. The evaluated SPI samples showed variations in polypeptide constituents and their conformations at the molecular level, that led to differences in the amount of soluble proteins. SPI insoluble fraction was characterised as particles with diverse range of shapes and size distributions. At the same SPI concentration, dispersion with the largest particle size exhibited the highest specific viscosity. Viscoelastic behaviour of dispersion containing particles with the largest mean diameter size required the lowest SPI concentration due to their high dispersed phase volume. The provided insight would enhance appropriate selection and utilisation of commercial SPI for the application and design of high protein foods with viscoelastic behaviour.

Keywords: soy protein, structural properties, insoluble particle, viscoelastic dispersion.

Introduction

Plant proteins are gaining positive reputation as a more sustainable protein source. Among the plant-based proteins, soybean is the most readily available and widely used as protein-rich food ingredients providing advantages on nutritional and functional properties. Among the greatest importance of soy protein functional properties is the ability to form viscoelastic gel network. Soy protein gel can be achieved by various means of gelation process as similar to other globular proteins which generally require unfolding of native protein structure to expose hydrophobic groups followed by different routes of protein aggregation [1]. At the molecular level, protein gel properties are influenced by both intrinsic and and extrinsic factor. The former consists of protein composition and conformation, whereas the latter includes pH, temperature, ionic strength, and pressure [2]. Soy protein gel is reported to be having shared characteristics of particle gel [3]. Similarly, gel formation from particle dispersion can be achieved by increasing inter-particle interactions through particle jamming [4]. The elastic network of particle dispersion is predominantly governed by mesoscopic structure rather than direct effect of molecular nature [5]. Therefore, it is important to encompass evaluation on structural properties in understanding protein functionalities. The structural properties are not limited to molecular level, but also include the larger length scales, namely mesoscopic, and macroscopic scales [6].

Soy protein isolate (SPI) is a highly purified soybean protein ingredient containing about 90% of protein. There are wide ranges of commercial SPI with tailored functionalities to fulfil various food applications. Commercial SPI tends to lose their native molecular conformation due to harsh processing conditions that leads to display limited solubility when suspended in water and forms protein particulate dispersion rather than protein solution [7–9]. Having limited solubility, flow properties of commercial SPI dispersion is mainly determined by physical characteristics of insoluble fraction at mesoscale structure, such as morphology, particle size, and their concentration [10]. Increasing SPI concentration leads to a viscoelastic gel behaviour due to particle jamming, yet the minimum concentration is varied [3,11–13]. Particle jamming within dispersion occurs when the phase volume of particles is above their random close packing [3,14]. Accordingly, characterisation of insoluble SPI fraction as particles combined with phase volume approach can be used as a different perspective to explain mesoscale structural properties that contribute to viscoelastic behaviour of SPI dispersion.

In food application, preserving native conformations of SPI is difficult hence the use of commercial SPI is more practical. Although many studies have reported on the viscoelastic properties of soy protein gels using commercial SPI, there are limited explanations on structural differences at various length scales [3,11-12,15]. This study aims to demonstrate the structural differences of several commercial and laboratory-prepared SPI at multiple length scales, namely molecular level, mesoscopic, and macroscopic scales, that contribute to viscoelastic behaviour of their dispersions. Structural differences at molecular scale were characterised by evaluating protein constituents and conformations, whereas mesoscale characterisation consisted of evaluation on soluble proteins, particle size and morphology of insoluble protein fraction. Rheological analysis was used to assess structural properties at macroscale. The provided insight would enhance appropriate selection and utilisation of commercial SPI for the application and design of high protein foods.

Materials and Methods

Materials

Three different commercial soy protein isolate (SPI) samples with minimum 90% (dry weight) protein content were kindly donated from Solae Belgium N.V (Ieper), namely SUPRO® 548, 670, and 760. For a comparison purpose, a laboratory prepared SPI was isolated from soybean flour (Fudco, London) that has been defatted with hexane. Protein isolation was conducted using a conventional alkaline extraction method at pH 9, followed by acid precipitation at pH 4.5, then subsequently washed, neutralised, and freeze-dried.

Preparation of dispersions

SPI powder was dispersed in deionised water at various concentrations (%wt) depending on the measurement types. The dispersions were magnetically stirred at 5 ^{o}C for at least 60 min until fully hydrated in a lidded vial using low speed to avoid foaming. Dispersions containing solid above 20% (wt) were vigorously hand mixed prior to magnetic stirring. All SPI sample dispersions at 5% (wt) concentration were within the neutral pH range at 7.08-7.36, hence the pH was less likely to affect the differences between samples.

Sodium dodecyl sulfate polyacrylamide gel electrophoresis (SDS-PAGE)

SDS PAGE was performed to compare protein molecular weight distribution of SPI samples according to procedure described by Bio-Rad [16]. SPI dispersions at 0.2% (wt) concentration were mixed with Laemli sample buffer (Sigma-Aldrich Co, MO, USA), at ratio 1:1 then boiled for 5 min and cooled back to ambient temperature. A precast 4–15% polyacrylamide gel (Bio-Rad Laboratories, CA, USA) was used and placed into Mini Trans-Blot® Cell (Bio-rad Laboratories Srl, Milan, Italy) filled with Tris Glycine SDS running buffer (Thermoscientific, IL, USA). Precision Plus Protein™ Standards All Blue (Bio-Rad Laboratories, CA, USA) was used as protein standard marker. An aliquot of 5 µl of samples and protein marker were pipetted into the gel and run at 100 V for 60 min. The gel was stained in solution containing Coomassie Brilliant Blue R-250 Dye (Fisher Scientific UK, Loughborough, UK) for 1 h and subsequently destained for 3 h. Electrophoresis was repeated three times to obtain consistent results. Gel image was captured using Bio-Rad Gel Doc XR System. Protein bands were identified as protein constituents of SPI according to a work by Sirison et al. [17].

Micro-differential scanning calorimetry (Micro-DSC)

Conformational states of soy proteins were resolved using measured heat flow of SPI dispersions in a Micro-Differential Scanning Calorimeter III (Setaram Instrumentation, France). About 800 mg of dispersions at the concentration of 10% (wt) was transferred into hermetically sealed sample vial made from hastelloy, while similar weight of deionized water was used as reference. Heating-cooling processes were performed in two cycles from 20 to 120 ^{o}C at a rate of 1 ^{o}C min^{-1}. Each measurement was run in duplicate.

Attenuated total reflectance – fourier transform infrared (ATR-FTIR) spectroscopy

All SPI samples were analysed using ATR-FTIR spectroscopy in both dry and dispersion forms. The FTIR spectra acquisition was conducted using a Bruker Tensor 27 System (Bruker Optik GmbH, Ettlingen, Germany) equipped with diamond ATR crystal and temperature controller (Graseby Specac Ltd., UK) and run on OPUS software version 7.2.139.1294. An open-air background test was run prior to the measurement of dry samples. Subsequently, a few mg of dry sample was placed into contact with the diamond ATR crystal and sample holder. All measurements, including dry and dispersion

samples, were run under 128 scans with 4 cm^{-1} resolutions. For the measurement of dispersion systems, SPI samples were dispersed in deuterium oxide (D_2O) at 10% (wt) concentration, to avoid band overlapping between protein and water. A single pipette drop of D_2O was run as background. A few drops of SPI dispersions were applied directly onto the diamond ATR crystal and sealed with a rubber gasket. Each measurement was run in duplicate. The acquired spectra were further processed, i.e. normalisation, baseline correction, derivatisation, and integration using Spectragryph optical spectroscopy software version 1.0.2 (https://www.effemm2.de/spectragryph/). Second derivative spectra were used to predict relative abundance of protein secondary structure, by taking the ratio of integration of each structure-assigned band to total corresponding secondary structures. Band assignment on protein conformation referred to a work by Bock and Damodaran [18].

Measurement of soluble protein

Soluble protein was quantified by measuring protein concentration from SPI soluble fraction. SPI dispersions at 0.1% (wt) concentration were transferred into 2 ml microtubes, then subsequently centrifuged at 10000 g and 5 ^{o}C for 15 min. The supernatant was then collected and filtered through a 0.45 µm nylon syringe filter. The filtered supernatant was used for protein measurement using bicinchoninic acid protein assay (Pierce Biotechnology, Rockford, Illinois, USA) as described in the protocol [19]. Protein solubility was calculated from the amount of soluble protein within the supernatant and expressed in g per 100 g SPI sample. Bovine serum albumin was used as standard. Each measurement was run in duplicate.

Light microscopy

An aliquot of 0.1% (wt) SPI dispersion was dropped onto the well of microscope slide (Marienfeld, Lauda-Königshofen, Germany) onto which the cover slip was carefully placed. Microscopic images were acquired using transmitted light under EVOS f1 microscope (AMG, Washington, USA) at the magnification of 40x.

Analysis of particle size distribution

SPI dispersions at the concentration of 1% (wt) were used to measure particle size distribution. The dispersions were kept stirred prior to measurement to prevent sedimentation. The measurement was based on the principles of light scattering using LS13320 Laser Diffraction Particle Size Analyzer (Beckman Coulter, High Wycombe, UK). The measurement was run for 60 s. Fraunhofer theory was used as optical model treating particles in spherical approximation. The value of dispersant (water) refractive index was set to 1.33. Each measurement was run in duplicate.

Evaluation of dispersion stability

Stability of SPI dispersions were evaluated by monitoring gravitational phase separation by using Turbiscan LAB (Formulaction, L'Union, France) based on multiple light scattering principles. Sample dispersion was transferred into a ~40 mm height flat bottom cylinder glass vial. The vial was placed into the measuring chamber and the temperature was set to 25 ^{o}C. Light backscattering (BS) intensity from 880 nm pulsed near-infrared light source was recorded across the height of vial every 30 s for 30 min. Each measurement was run in duplicate.

Estimation of dispersed phase volume

Dispersed phase volume of SPI insoluble fraction were measured from dispersions at 1, 4, 7, 10, and 13% (wt) concentrations in a centrifuge tube following the work described by Amani et al. [20] with some modifications. Dispersions were centrifuged at 1500 g for 5 min. Phase volumes were calculated by dividing volume of sediment by total volume of dispersion. Each measurement was run in duplicate. Linear regression was used to obtain extrapolated phase volume at higher concentration.

Rheological measurement

Viscosity of SPI dispersions at various concentrations were measured on a rheometer (Physica MCR 301, Anton Paar, Austria) using concentric cylinder geometry. The applied rotational shear was ramp-up from 0.1 to 100 s^{-1}. To compare concentration dependence of viscosity, the data are plotted as specific viscosity (ηsp) that given by:

$$\eta_{sp} = {}^{(\eta - \eta_s)}/_{\eta_s} \quad (1)$$

where η is viscosity of dispersion at Newtonian plateau and ηs is viscosity of solvent (i.e. water). Where Newtonian plateau is not apparent, the smallest measurable viscosity data points at low shear is used.

Viscoelastic behaviour of SPI dispersions was measured using the same apparatus. The serrated parallel plate geometry was used as measuring system at 1 mm gap. To obtain a correct measurement of stable dispersions, a fixed dispersed phase volume was used instead of concentration. The amplitude strain sweep tests were conducted at a fixed angular frequency of 10 rad s^{-1}. The angular frequency sweep tests were performed at a constant amplitude strain of 0.1%. Evaporation and large temperature gradients were prevented by using low-viscosity mineral oil and a peltier-controlled hood. Each test was run in duplicate.

Statistical analysis

IBM SPSS Statistics software version 26 (IBM Corp., Armonk, NY, USA) was used to conduct statistical data analysis. Data were analysed using one-way ANOVA followed by Tukey's posthoc test to determine significant differences ($p<0.05$).

Results and Discussion

Polypeptide constituents and predicted conformation

The resolved SDS PAGE bands represent various constituting polypeptides within SPI samples (Fig. 1). Lab SPI, Supro 548, and 760 showed a typical SDS PAGE pattern of individual subunits that belong to major soybean proteins, i.e. β-conglycinin and glycinin. Ratios between the two seems to be varied as indicated by band intensity differences, e.g. less intense β-conglycinin bands from the Lab SPI and strong intensities of glycinin subunits on all three samples, which might be attributed to varieties of soybean cultivars and different methods of protein extraction [17,21]. Variations in soy protein composition and its ratio have been reported to affect thermal aggregation kinetics, amount of soluble and insoluble fractions, and the properties of resulting protein gel structure [22,23]. In contrast, Supro 670 exhibited polypeptide constituents with lower molecular weight, approximately around 25, 15, and 10 kDa, and the absence of typical β-conglycinin and glycinin subunits. The most

possible reason for this is that the manufacturing of this sample involved hydrolysis of proteins that led to a reduced molecular weight, as previously reported [24].

In addition to protein composition, it is important to elaborate the conformation of SPI samples since it is closely related to protein solubility. Micro-DSC was used to resolve thermal properties of the proteins showing whether they are in native or denatured structural states. Despite sharing similar SDS PAGE profiles, commercial SPI samples showed different thermal properties from the Lab SPI (Fig. 2). The absence of thermal events within commercial SPI thermograms indicated the proteins are already in a denatured and aggregated form. This is unsurprising since manufacturing of commercial SPI commonly involves high temperature drying [7]. On the other hand, the thermogram of Lab SPI showed an endothermic peak at about 90 ^{o}C suggesting a structural transition taking place. The transition can be attributed to the unfolding of partially denatured proteins due to alkaline exposure upon preparation of Lab SPI. Denaturation temperature of SPI containing β-conglycinin and glycinin have been reported as two endothermic events in which glycinin is higher than β-conglycinin [8, 25]. The Lab SPI sample contains higher glycinin concentration, as shown by SDS-PAGE result, and hence the single thermal transition peak obtained in this study seems to be the denaturation of glycinin.

Structural differences of SPI samples were also evaluated using FTIR spectroscopy. FTIR spectra of dry SPI samples exhibited indistinguishable band positions and patterns between samples (Fig. 3). However, the spectra can be useful as reference for absorption bands of interest in resolving protein secondary structure, i.e. amide I and II. Sharp peaks of amide I bands appeared at ~1633-1636 cm^{-1} that predominantly arise from C=O stretching vibrations of the protein backbone. Less intense peak of amide II bands located at ~1520-1524 cm^{-1} results from C-N stretching and N-H bending vibrations [26].

FTIR spectra of SPI dispersions showed different peak positions compared to the spectra of dry sample (Fig. 3). It is important to note that the use of D_2O in FTIR spectroscopy study of protein will cause hydrogen-deuterium (H-D) exchanges between D_2O and protein, leading to conversions from N-H to N-D due to replacement of hydrogen by deuterium atom (Barth, 2007). Structural differences between remaining native and fully denatured SPI were observed in the amide II' peak at 1400-1500 cm^{-1}. The same peak position for amide II' were observed for all samples at ~1443 cm^{-1}

with the least intensity on Lab SPI spectra and showing residual peak of amide II at ~1561 cm^{-1} as a result of incomplete H-D exchanges. This clarified that H-D exchanges were prevented to take place inside the protein core due to native folded structure, whereas the other denatured SPI samples exhibit larger amount of N-deuteration due to an unfolded structure [27].

Differences in secondary structure composition between SPI samples were observed through Amide I peak position and can be further resolved using second derivative spectra (Fig. 3). The peak of Lab SPI located at the highest wavenumber among all samples, i.e. ~1635 cm^{-1}, whereas Supro 548, 670, and 760 were at ~1629, ~1624, and ~1632 cm^{-1} respectively. These peak positions may sufficiently indicate the predominant secondary structure of soy protein was β-sheet in agreement with other studies [28-31]. Further examination using second derivative spectra clearly separated major band position of Lab SPI to ~1634 cm^{-1} corresponding to intramolecular β-sheets structure, whereas the commercial SPIs' major band positions at ~1622-1624 cm^{-1} are responsible for intermolecular β-sheets of protein aggregates [32-33]. Table 1 showed the estimation on relative abundance of protein secondary structures. As expected from the amide I band position, β-sheet appeared as major secondary structure in all SPI samples including intramolecular parallel and intermolecular antiparallel β-sheet structures that mainly found in native and denatured protein respectively. Interestingly, proportion of β-turn was larger in commercial SPI samples, which has been reported as contributing structure to the insoluble aggregates [29].

Soluble protein concentration and physical characteristics of insoluble SPI fraction

Soluble protein concentration within SPI dispersions are presented in Table 2. Lab SPI exhibited the highest amount of soluble protein that might be due to the preserved folded structure retaining hydrophobic site inside the protein core. Commercial samples with the lowest soluble protein concentration were Supro 760 and 548 showing 18.94 and 28.34 g/ 100 g SPI, respectively. Higher degrees of denaturation are known to increase hydrophobicity of SPI and resulting in lower solubility [34]. Considering similar protein compositions and conformations between the two, the differences in soluble protein concentration might be due to different processing conditions. In contrast, protein solubility of Supro 670 were as high as 54.97 g 100 g^{-1} SPI that is most likely associated with soluble

aggregates of low molecular weight proteins, confirming the results from SDS-PAGE presented earlier.

Characterisation on SPI insoluble fractions were performed at dilute concentrations, hence considering swelling-ability of samples, the observed particles were in the swollen state. Microscopy images of insoluble particles within SPI dispersions showed variations in morphology and size (Fig. 4). Due to the lack of useful observation of specific patterns at available maximum magnification, the Lab SPI microscopy image is not displayed. Supro 548 and 760 appeared as transparent particles due to water penetration. The former was an irregular granular shape, while the latter was more spherical and larger in size due to swelling. Considering similar protein compositions and low solubility of both samples, a relatively high protein concentration occurs within the structure of insoluble particle. However, differences in water retention are attributed to morphological microstructure of SPI particles as suggested by Urbonaite et al. [35]. Conversely, Supro 670 was distinguished as spherical dark particles with a wide size range. The dark colour suggests a characteristic of densely packed small aggregates into spherical shape. This can be explained as manufacturing of SPI from low molecular weight proteins were unable to build morphological structures with water-retaining ability.

The size distribution of insoluble particles showed noticeable differences between Lab SPI and commercial samples (Fig. 5). Despite its preserved native conformation and high protein solubility, the Lab SPI dispersion contained small particles mainly distributed between 0.1-10 μm that might be attributed to the aggregates of denatured β-conglycinin. As confirmed from microscopy observation, Supro 548 and 760 mostly contained large insoluble particles distributed between 10-200 μm. Although morphological features between the two were clearly different, their mean diameter particle size were only slightly different due to sphericity assumption of laser diffraction particle sizing. This means the actual mean diameter size of irregular wrinkled-shape Supro 548 might be smaller than the calculated result. Supro 670 dispersion showed major distribution of large particles between between 10-100 μm with apparent distribution of small particles below 10 μm. Since the conformations of commercial samples are largely denatured, differences in size distribution can be associated with the different molecular weight of proteins involved within insoluble fraction.

Sedimentation of insoluble fraction were observed from SPI dispersions at 1% and 10% concentration after 30 min settling under normal gravity. All commercial samples showed sedimentation with different height of beds at 1% concentration (Fig. 6). The lowest sediment bed was observed on Supro 670 dispersion due to relatively high amounts of soluble fractions and smaller insoluble particle diameter size, followed by SPIs with larger particle size creating higher sediment bed. In contrast, Lab SPI did not show any sedimentation at the bottom of the vial due to high protein solubility. Light backscattering intensity of dispersion is dependent to the particle diameter size and their volume fraction, with decreasing particle size lead to an increase of backscattering intensity specifically when particles are larger than wavelength of incident light at 880 nm, and increasing volume fraction lead to an increase of backscattering intensity within the range of 0.1-10% volume fraction [36]. Variations in light backscattering intensity of sediment bed were also observed and can be attributed to the particle mean diameter size (Table 1). Supro 670 had nearly tripled the backscattering intensity of its corresponding commercial SPIs, followed by 548 and 760, respectively.

Increasing SPI concentration to 10% led to higher sediment beds of Supro 670 and nearly stable Supro 548 showing slightly separated phase at the top of the vial (Fig. 6). However, phase separation was no longer observed on 10% Supro 760 dispersion due to full volume occupancy of highly packed particles. Supro 760 particles were restricted to swell as indicated by higher light backscattering intensity compared to Supro 548, meaning that particle size of Supro 760 is smaller than Supro 548 due to volume packing at 10% concentration. Lab SPI showed a stable dispersion without sedimentation with high intensity of light backscattering due to very low volume fraction of small insoluble particles.

The measured height of sediment bed also provides information on dispersed phase volume fraction of insoluble particles under normal gravity. However, estimation on phase volume fraction in this study was using centrifugal forces at 1500 times of normal gravity to minimise the differences on swelling-ability between SPI insoluble particles. At the same concentration and considering particle de-swelling due to centrifugal forces, SPI particles with larger size resulted in a higher phase volume (Fig. 7). Phase volume of soft particle dispersions is known to highly affects their rheological properties which behave differently at below and above random close packing which often refers to

64% phase volume of monodisperse hard sphere particles [37]. Discussion on phase volume will be further used to explain rheological properties of dispersions.

Viscosity and viscoelastic properties of SPI dispersions

Increasing concentration of different SPI samples led to changes in specific viscosity and flow behaviour of dispersions at various extents (Fig. 8). At 10% concentration, Lab SPI and Supro 670 dispersions exhibited the lowest viscosity increases and remained showing Newtonian behaviour as shown by their Power Law indices around 1. Low viscosity of Lab SPI dispersion is mainly due to high solubility of high molecular weight globular proteins in native structure with unexposed hydrophobic groups, hence attribution to phase volume of particles may not be relevant. However, low viscosity of Supro 670 dispersion is attributed to small size insoluble particles made up of low molecular weight proteins occupying low phase volume even at 10% concentration. This is in agreement with other's work on non-colloidal soft particle dispersion in water following monodisperse hard sphere model behaviour as Newtonian at low phase volume [14]. It is expected that dispersions containing larger insoluble particle size exhibited higher viscosity due to higher dispersed phase volume fraction. Increasing concentration of Supro 548 and 760 within dispersion tremendously increased their specific viscosity. At 10% (wt) concentration, insoluble particles within Supro 548 dispersion occupied about 47% phase volume hence showing high viscosity and slightly shear thinning behaviour indicated by decreasing Power Law index. Supro 760 dispersions began to exhibit shear thinning behaviour as low as 4% (wt) concentration due to large particle size. Shear thinning behaviour of dispersions can be explained as spatial rearrangement of dispersed particles and anisotropic deformation [38]. Shear thinning behaviour of SPI dispersions at above 10% concentration were also confirmed by other studies [31,39].

Evaluation on viscoelastic properties of dispersions were conducted on commercial SPI samples emphasising the contribution of insoluble particles at a fixed estimated phase volume. A 65% phase volume was selected assuming SPI particles above random close packing based on the observation of Supro 760. Calculation of SPI concentration was extrapolated from linear regression of concentration-phase volume curve (Fig. 7), therefore at the same phase volume, Supro 670 contained the highest solid concentration while Supro 760 was the lowest. All concentrated SPI dispersions

exhibited viscoelastic behaviour as expected from high phase volume (Fig. 9). The highest modulus of Supro 670 dispersions was attributed to higher surface area of smaller rigid particles that deeply jammed and created the longest linear viscoelastic region (LVER) as confirmed by normalised storage modulus. Their non-LVER showed strain-thinning behaviour as the strain increased, and continuously break the structure of jammed particles at high amplitude strain. Slightly different behaviour was observed on Supro 548 and 760 showing the shorter LVER, then continued by weak and strong strain overshoots respectively at non-LVER prior to crossover point when amplitude strain closer to 100%. The strain overshoots within non-linear viscoelastic region were attributed to large size and deformability of both SPI particles that led to some extent of structural rearrangement at high amplitude strain prior to breakage, i.e. increasing modulus as the strain increase then continuously decreasing.

Viscoelastic gel behaviour of concentrated SPI dispersions were confirmed by predominant elastic component throughout the frequency ranges up to 200 $rad.s^{-1}$ without appearance of crossover point due to high interparticle physical interactions of jammed system (Fig. 10). Frequency dependence of storage and loss modulus appeared at varying degree demonstrating higher modulus with increasing frequency. Supro 670 showed the most frequency-dependent on storage modulus indicating weaker structure with a slope of 0.14 that is attributed to smaller particle radius, whereas concentrated dispersion containing larger particles of Supro 548 and 760 showed less dependency with the slope of 0.10 and 0.07 respectively.

Conclusions

This study confirms structural differences of several commercial SPIs at multiple length scales. The evaluation on polypeptide constituents reveals that low viscosity commercial SPI consisted of only low molecular weight proteins, whereas the rest of SPIs indicated the presence of glycinin β-conglycinin as major protein constituents. All commercial SPIs showed a fully denatured structure, in contrast to the highly soluble laboratory-prepared SPI. Viscosity of dispersions at the same SPI concentration were highly influenced by physical factors, such as insoluble particle shape and size distribution. Furthermore, the use of estimated insoluble particle phase volume, instead of concentration, was able

to explain the differences in viscosity and viscoelastic behaviour. The provided insight is expected to contribute on the utilisation of commercial protein materials for development of high protein foods.

Acknowledgments

Financial support from the Ministry of Research, Technology, and Higher Education of the Republic of Indonesia is acknowledged.

Compliance with Ethical Standards

Conflict of Interest: The authors declare that they have no conflict of interest.

References

1. K. Nishinari, Y. Fang, S. Guo, G. O. Phillips, Food Hydrocoll. **39**, 301 (2014).
2. A. Totosaus, J.G. Montejano, J.A. Salazar, I. Guerrero, Int. J. Food Sci. Technol. **37**, 589 (2002).
3. J. A. M. Berghout, R. M. Boom, A. J. van der Goot, Food Hydrocoll. **43**, 465 (2015).
4. R. G. M. van der Sman, A. J. van der Goot, Soft Matter **5**, 501 (2009).
5. L. E. van Riemsdijk, J. H. B. Sprakel, A. J. van der Goot, R. J. Hamer, Food Biophys. **5**, 41 (2010).
6. E. A. Foegeding, J. Food Sci. **80**, C2670 (2015).
7. P. Singh, R. Kumar, S. N. Sabapathy, A. S. Bawa, Compr. Rev. Food Sci. Food Saf. **7**, 14 (2008).
8. M. Keerati-U-Rai, Z. Wang, M. Corredig, J. Am. Oil Chem. Soc. **88**, 1593 (2011).
9. F. Liu, C. H. Tang, J. Agric. Food Chem. **61**, 8888 (2013).
10. M. C. Añón, D. A. Sorgentini, J. R. Wagner, J. Agric. Food Chem. **49**, 4852 (2001).
11. J. Ahmed, H. S. Ramaswamy, I. Alli, J. Food Sci. **71**, E158 (2006).
12. H. Hu, J. Wu, E.C. Li-Chan, L. Zhu, F. Zhang, X. Xu, G. Fan, L. Wang, X. Huang, S. Pan, Food Hydrocoll. **30**, 647 (2013).
13. C. H. Tang, X. Y. Wang, X. Q. Yang, L. Li, J. Food Eng. **92**, 432 (2009).
14. H. M. Shewan, J. R. Stokes, J. Colloid Interface Sci. **442**, 75 (2015).

15. B. L. Dekkers, R. M. Boom, A. J. van der Goot, Food Res. Int. **107**, 281 (2018).
16. Bio-Rad Laboratories, Mini-PROTEAN® Precast Gels: Instruction manual and application guide (2011), https://www.bio-rad.com/webroot/web/pdf/lsr/literature/Bulletin_1658100.pdf. Accessed 15 October 2017.
17. J. Sirison, K. Matsumiya, M. Samoto, H. Hidaka, M. Kouno, Y. Matsumura, Biosci. Biotechnol. Biochem. **81**, 790 (2017).
18. J. E. Bock, S. Damodaran, Food Hydrocoll. **31**, 146 (2013).
19. Pierce Biotechnology, Pierce™ BCA Protein Assay Kit (2011), http://tools.thermofisher.com/content/sfs/manuals/MAN0011430_Pierce_BCA_Protein_Asy_UG.pdf. Accessed 22 October 2017.
20. N. G. Amani, A. Buléon, A. Kamenan, P. Colonna, J. Sci. Food Agric. **84**, 2085 (2004).
21. S. Wu, P.A. Murphy, L.A. Johnson, M.A. Reuber, A. R. Fratzke, J. Agric. Food Chem. **48**, 2702 (2000).
22. J. M. S. Renkema, J. H. M. Knabben, T. van Vliet, Food Hydrocoll. **15**, 407 (2001).
23. J. Guo, X. Q. Yang, X. T. He, N. N. Wu, J. M. Wang, W. Gu, Y. Y. Zhang, J. Agric. Food Chem. **60**, 3782 (2012).
24. S. M. Rutherfurd, C. A. Montoya, M. L. Zou, P. J. Moughan, L. N. Drummond, M. J. Boland, Food Chem. **129**, 1681 (2011).
25. J. M. . Renkema, C. M. . Lakemond, H. H. . de Jongh, H. Gruppen, T. van Vliet, J. Biotechnol. **79**, 223 (2000).
26. K. Wang, D.W. Sun, H. Pu, Q. Wei, Trends Food Sci. Technol. **67**, 207 (2017).
27. J. Kong, S. Yu, Acta Biochim. Biophys. Sin. **39**, 549 (2007).
28. P. Guerrero, J. P. Kerry, K. de la Caba, Carbohydr. Polym. **111**, 598 (2014).
29. C.H. Tang, C.Y. Ma, LWT Food Sci. Technol. **42**, 606 (2009).
30. J. Zhang, L. Liang, Z. Tian, L. Chen, M. Subirade, Food Chem. **133**, 390 (2012).
31. H. Hu, J. Wu, E. C. Y. Li-Chan, L. Zhu, F. Zhang, X. Xu, G. Fan, L. Wang, X. Huang, S. Pan, Food Hydrocoll. **30**, 647 (2013).
32. C. Schmitt, C. Bovay, A.-M. Vuilliomenet, M. Rouvet, L. Bovetto, R. Barbar, C. Sanchez, Langmuir **25**, 7899 (2009).

33. B. Shivu, S. Seshadri, J. Li, K. A. Oberg, V. N. Uversky, A. L. Fink, Biochemistry **52**, 5176 (2013).

34. M.B. Barac, M.B. Pesic, S.P. Stanojevic, A.Z. Kostic, ,V. Bivolarevic, J. Food Sci. Technol. **52**, 2779 (2015).

35. V. Urbonaite, H. H. J. De Jongh, E. Van Der Linden, L. Pouvreau, J. Agric. Food Chem. **62**, 7550 (2014).

36. Formulaction SAS, Turbiscan® LAB user guide (2007).

37. H. M. Shewan, J. R. Stokes, in Gums Stabilisers Food Ind. **16** (2012), pp. 165–174.

38. R. G. Utrilla-Coello, M. E. Rodríguez-Huezo, H. Carrillo-Navas, C. Hernández-Jaimes, E. J. Vernon-Carter, J. Alvarez-Ramirez, Carbohydr. Polym. **101**, 154 (2014).

39. A. R. Jambrak, V. Lelas, T. J. Mason, G. Krešić, M. Badanjak, J. Food Eng. **93**, 386 (2009).

Figure captions

Fig. 1. SDS PAGE of SPI samples. Lane (1) standard protein marker; (2) Lab SPI; (3) Supro 548; (4) Supro 670; (5) Supro 760. This gel image represents triplicate experiments

Fig. 2 Thermogram of different SPI dispersions at 10% (wt) concentration and heating rate at 1 ^{o}C min^{-1}. Lab SPI (dotted line); Supro 548 (dashed line); Supro 670 (dashed and dotted line); Supro 760 (solid line). The results are representative of duplicate experiments

Fig. 3 FTIR spectra of SPI samples in dry powder and dispersion forms (a); second derivative spectra of SPI dispersions at amide I band (b). Lab SPI (dotted line); Supro 548 (dashed line); Supro 670 (dashed and dotted line); Supro 760 (solid line). The results are means of duplicate experiments

Fig. 4 Light micrograph of insoluble particles of SPI dispersions from Supro 548 (a), 670 (b), and 760 (c). Scale bar shows 100 μm. The results are representative of duplicate experiments

Fig. 5 Particle size distribution of insoluble SPI particles. Lab SPI (dotted line); Supro 548 (dashed line); Supro 670 (dashed and dotted line); Supro 760 (solid line). The results are means of duplicate experiments

Fig. 6 Light backscattering intensity of SPI dispersions at 1% (a) and 10% (b) concentration across the height of vial measured after settling for 30 min. Lab SPI (dotted line); Supro 548 (dashed line); Supro 670 (dashed and dotted line); Supro 760 (solid line). The results are representative of duplicate experiments

Fig. 7 Dispersed phase volume of commercial SPI dispersions at various concentration. Supro 548: measured (filled triangle) and extrapolated (open triangle); Supro 670: measured (filled square) and extrapolated (open square); Supro 760: measured (filled circle). The results are means of duplicate experiments

Fig. 8 Logarithmic plot of specific viscosity (a) and Power Law index (b) of SPI dispersion at various concentrations. Lab SPI (diamond); Supro 548 (triangle); Supro 670 (square); Supro 760 (circle). The results are means of duplicate experiments

Fig. 9 Storage (filled symbols) and loss modulus (open symbols) of SPI dispersions as a function of amplitude strain (a); Normalised storage modulus (open symbols) as a function of amplitude strain. Supro 548 (triangle); Supro 670 (square); Supro 760 (circle). The results are representative of duplicate experiments

Fig. 10 Frequency dependence of storage (filled symbols) and loss modulus (open symbols) of commercial SPI dispersions at 65% phase volume. Supro 548 (triangle); Supro 670 (square); Supro 760 (circle). The results are representative of duplicate experiments

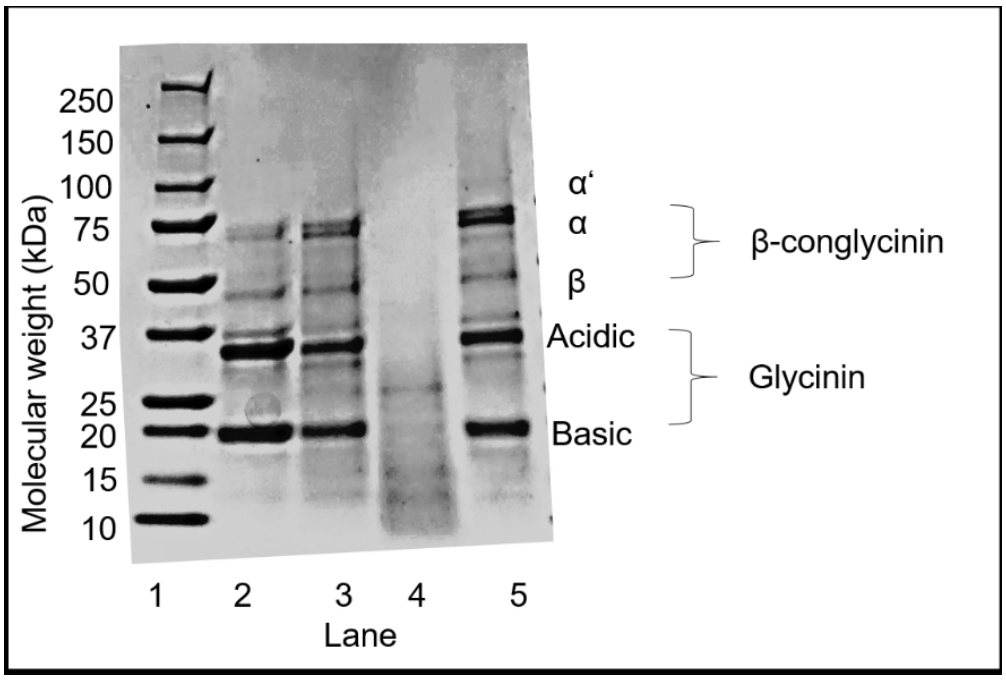

SDS PAGE of SPI samples. Lane (1) standard protein marker; (2) Lab SPI; (3) Supro 548; (4) Supro 670; (5) Supro 760. This gel image represents triplicate experiments

101x68mm (220 x 220 DPI)

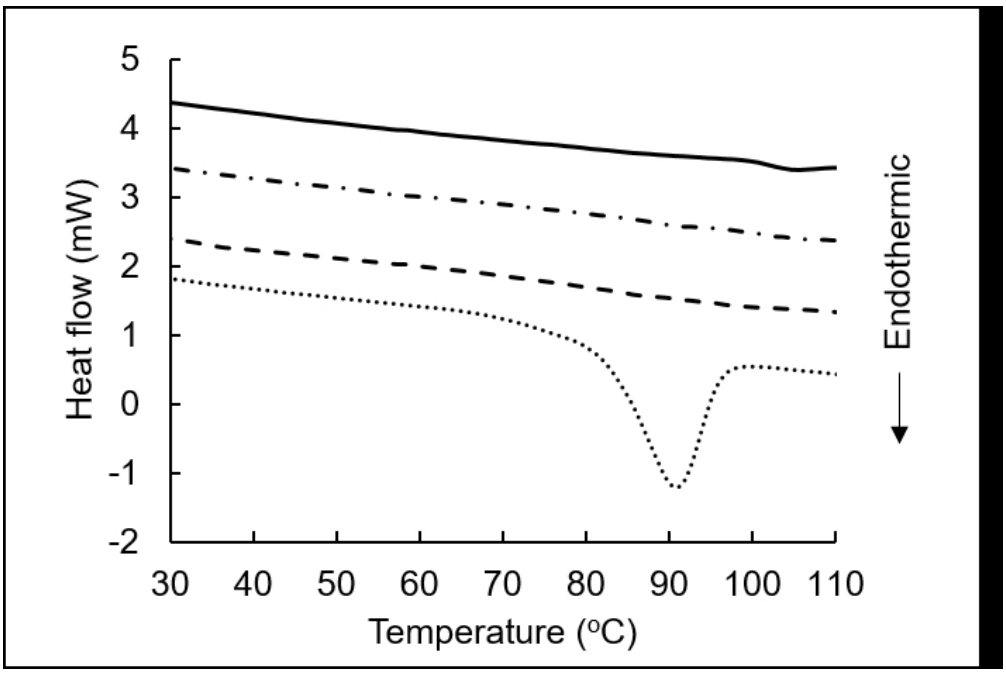

Thermogram of different SPI dispersions at 10% (wt) concentration and heating rate at 1 $^{o}C\ min^{-1}$. Lab SPI (dotted line); Supro 548 (dashed line); Supro 670 (dashed and dotted line); Supro 760 (solid line). The results are representative of duplicate experiments

120x79mm (150 x 150 DPI)

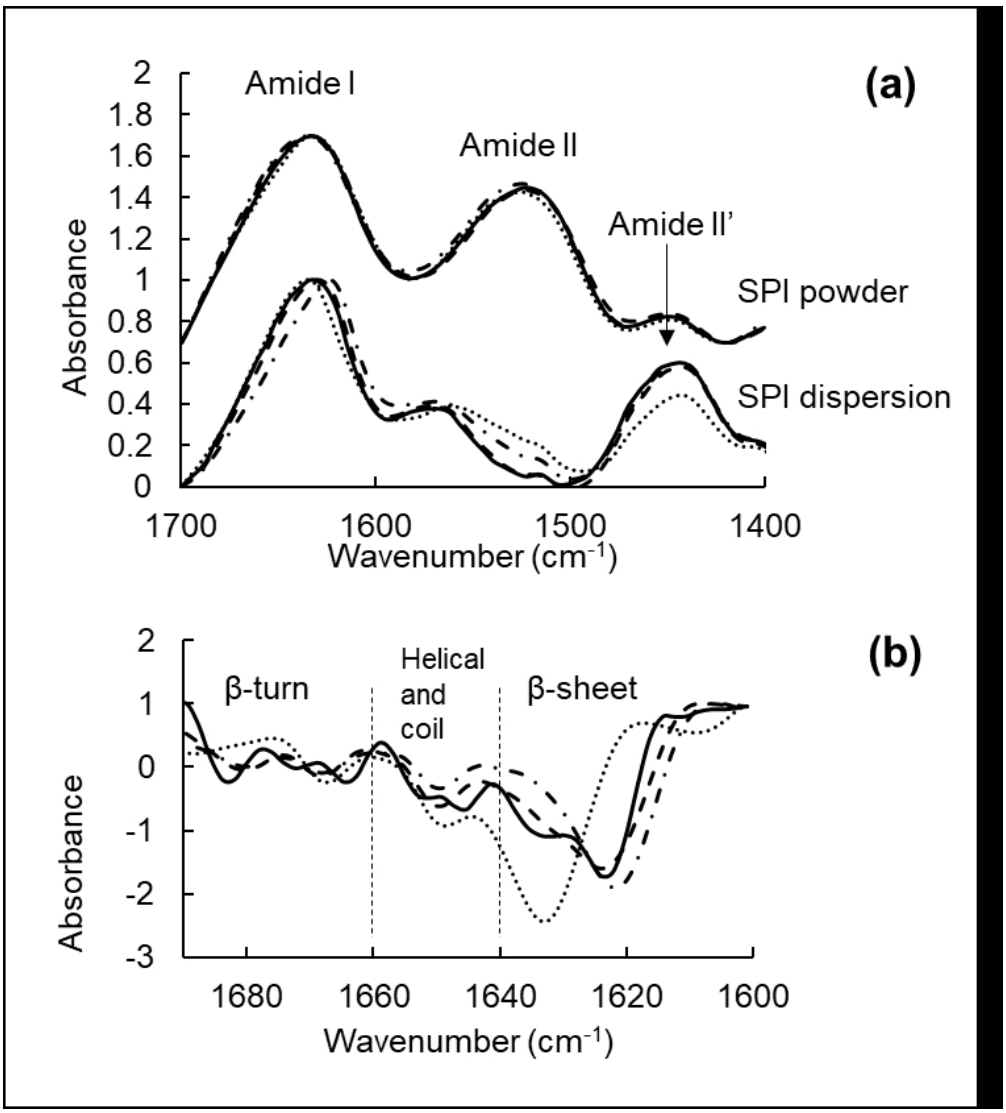

FTIR spectra of SPI samples in dry powder and dispersion forms (a); second derivative spectra of SPI dispersions at amide I band (b). Lab SPI (dotted line); Supro 548 (dashed line); Supro 670 (dashed and dotted line); Supro 760 (solid line). The results are means of duplicate experiments

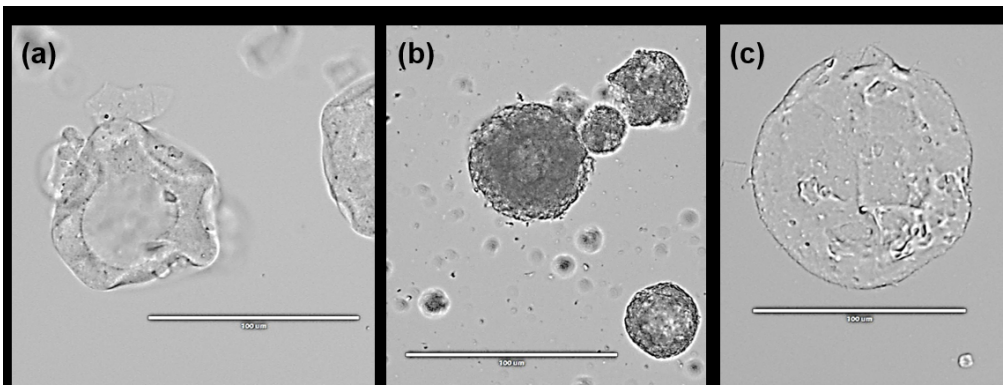

Light micrograph of insoluble particles of SPI dispersions from Supro 548 (a), 670 (b), and 760 (c). Scale bar shows 100 μm. The results are representative of duplicate experiments

192x72mm (150 x 150 DPI)

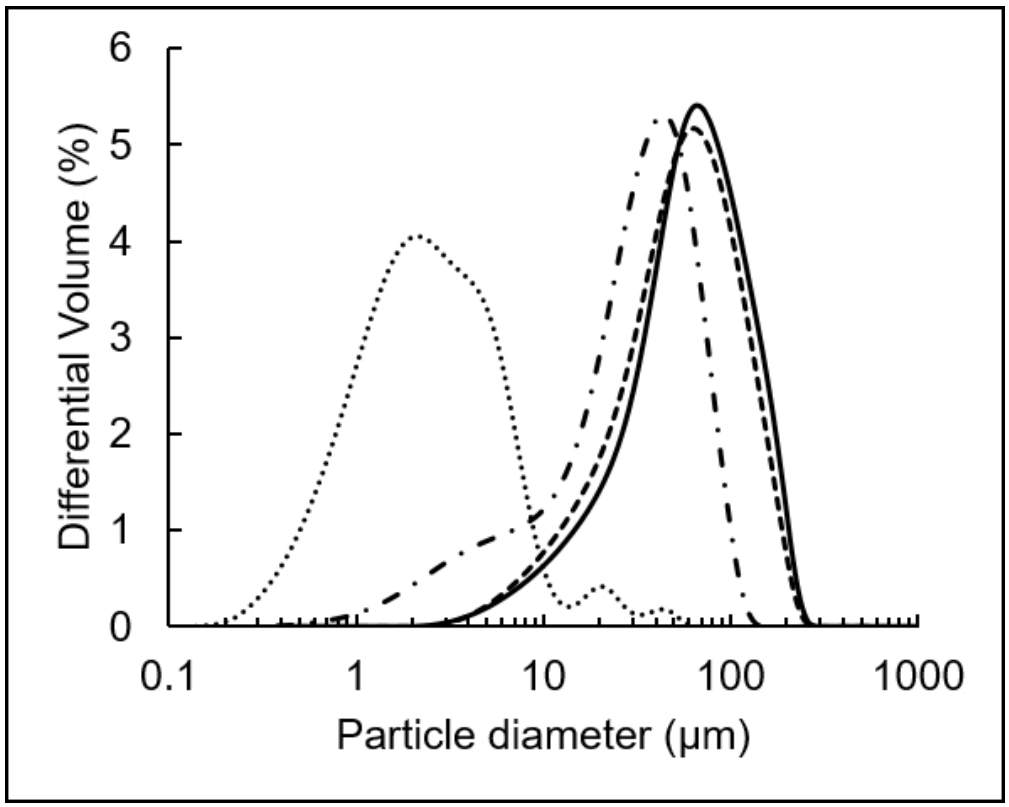

Particle size distribution of insoluble SPI particles. Lab SPI (dotted line); Supro 548 (dashed line); Supro 670 (dashed and dotted line); Supro 760 (solid line). The results are means of duplicate experiments

100x80mm (150 x 150 DPI)

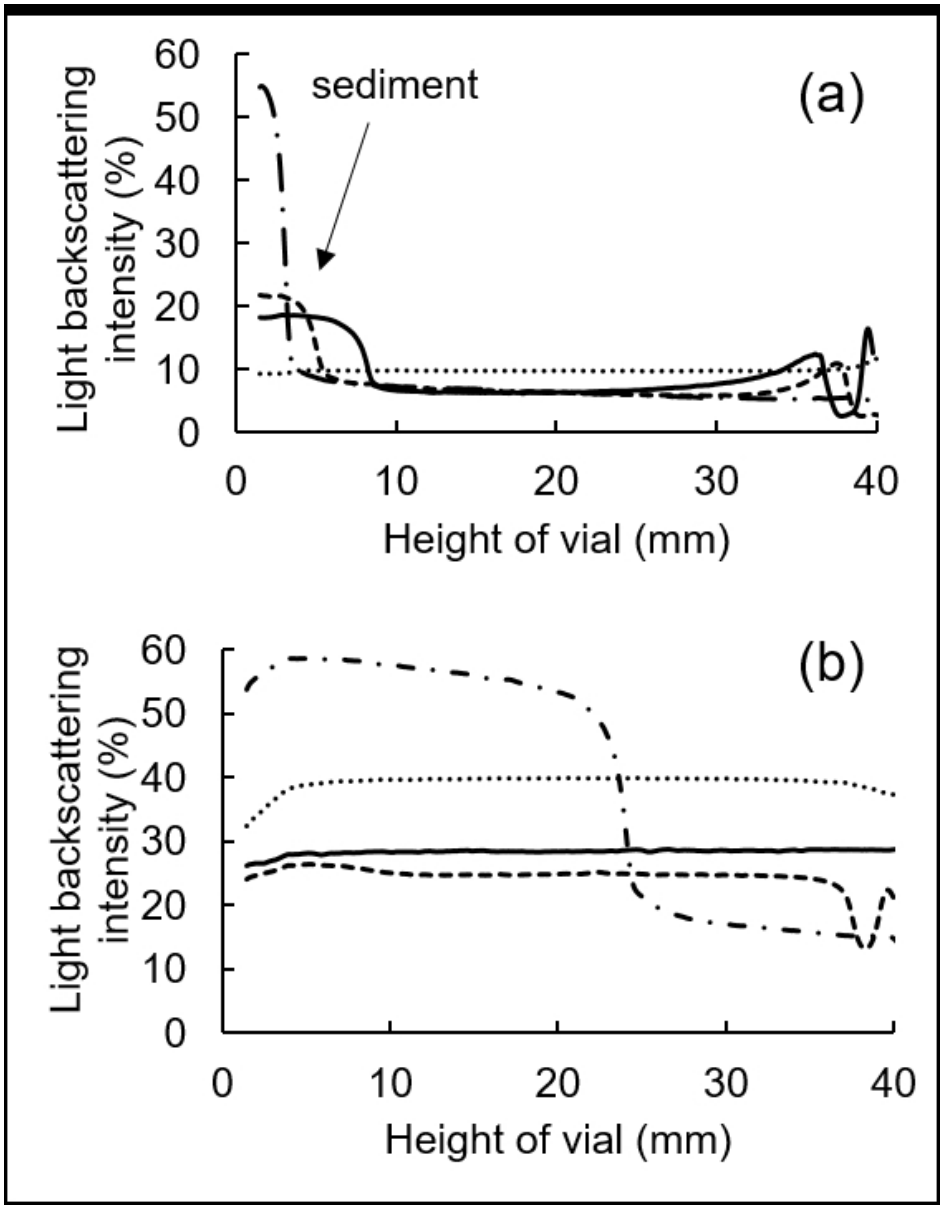

Light backscattering intensity of SPI dispersions at 1% (a) and 10% (b) concentration across the height of vial measured after settling for 30 min. Lab SPI (dotted line); Supro 548 (dashed line); Supro 670 (dashed and dotted line); Supro 760 (solid line). The results are representative of duplicate experiments

95x122mm (150 x 150 DPI)

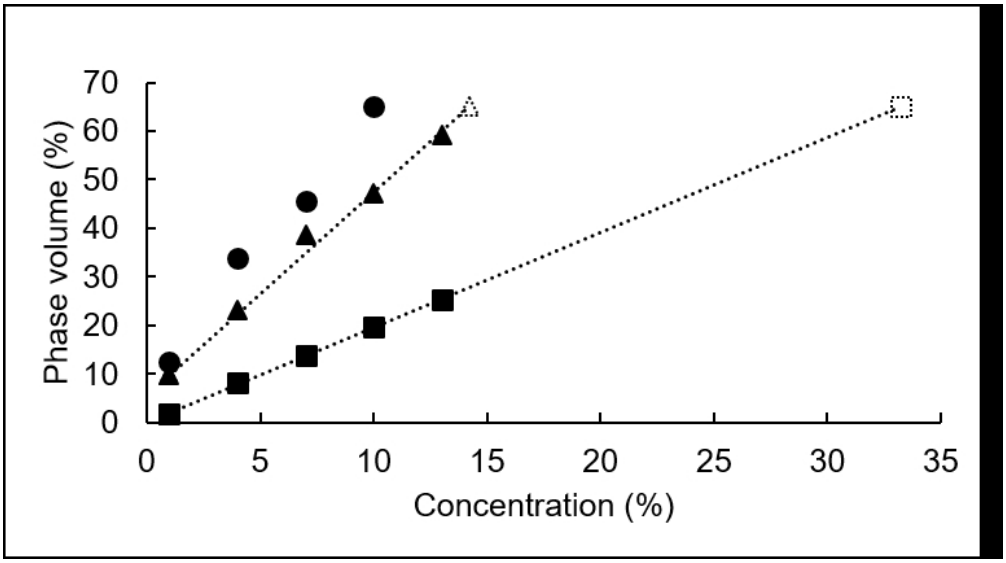

Dispersed phase volume of commercial SPI dispersions at various concentration. Supro 548: measured (filled triangle) and extrapolated (open triangle); Supro 670: measured (filled square) and extrapolated (open square); Supro 760: measured (filled circle). The results are means of duplicate experiments

130x72mm (150 x 150 DPI)

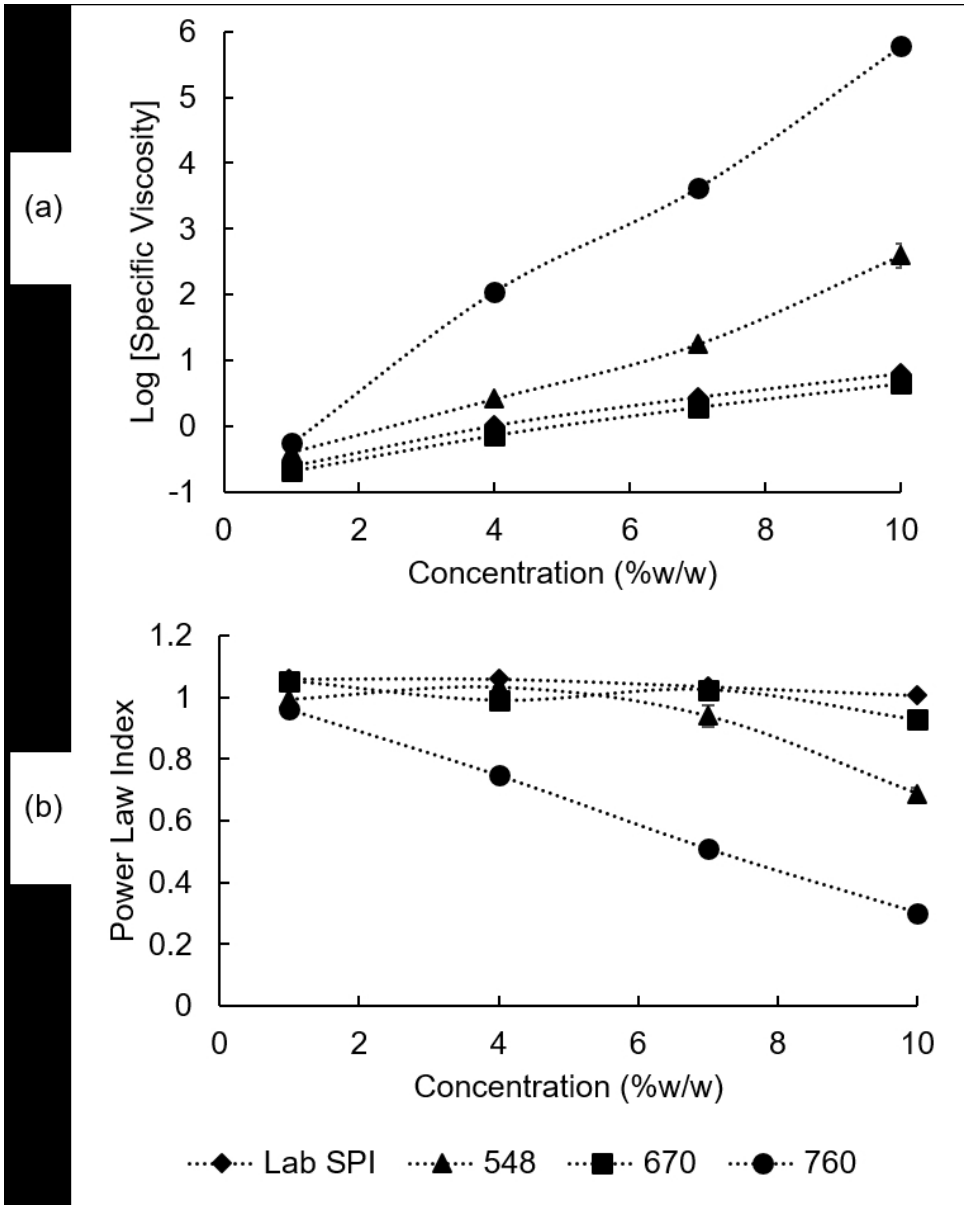

Logarithmic plot of specific viscosity (a) and Power Law index (b) of SPI dispersion at various concentrations. Lab SPI (diamond); Supro 548 (triangle); Supro 670 (square); Supro 760 (circle). The results are means of duplicate experiments

128x160mm (150 x 150 DPI)

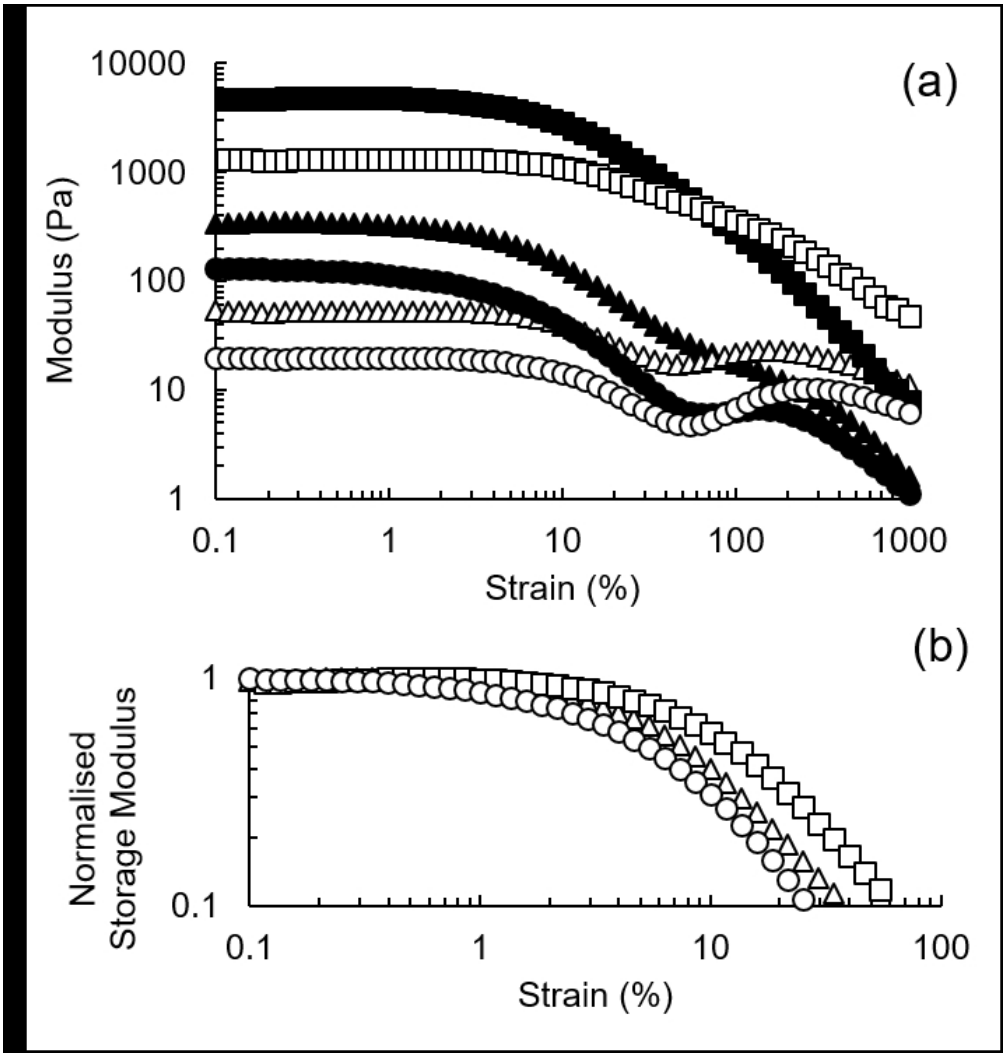

Storage (filled symbols) and loss modulus (open symbols) of SPI dispersions as a function of amplitude strain (a); Normalised storage modulus (open symbols) as a function of amplitude strain. Supro 548 (triangle); Supro 670 (square); Supro 760 (circle). The results are representative of duplicate experiments

121x127mm (150 x 150 DPI)

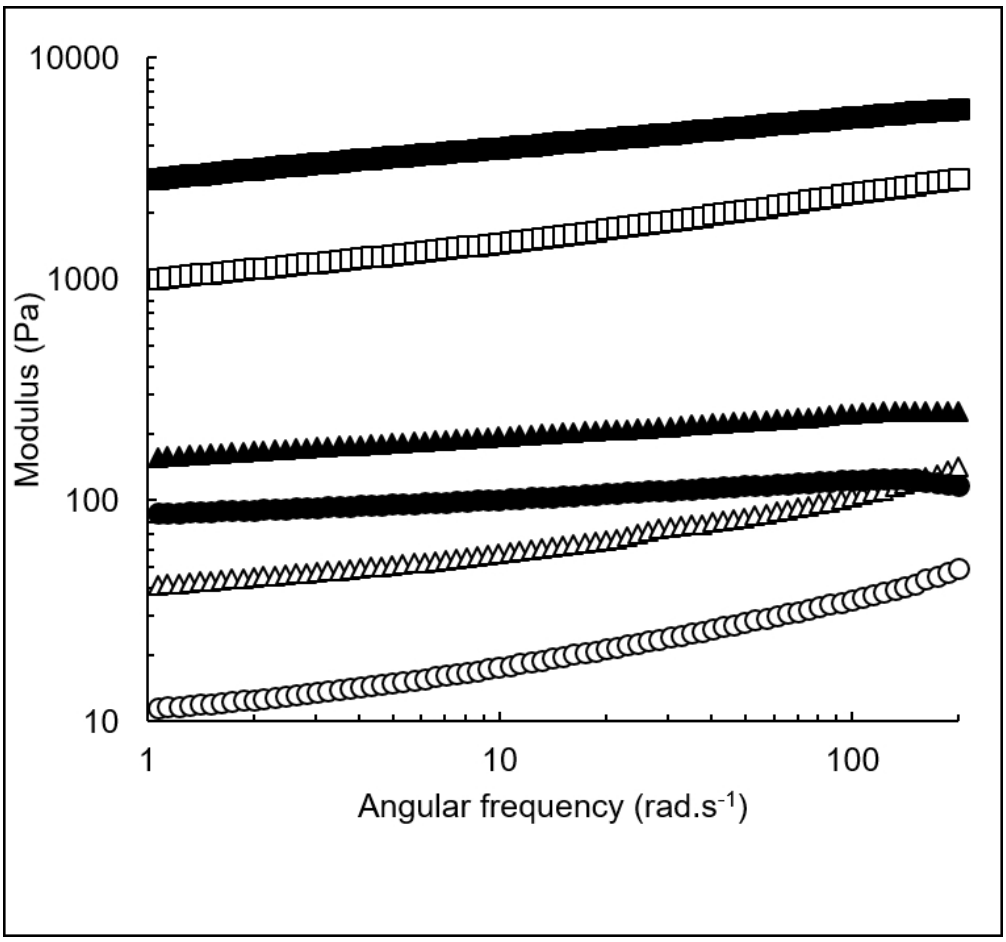

Frequency dependence of storage (filled symbols) and loss modulus (open symbols) of commercial SPI dispersions at 65% phase volume. Supro 548 (triangle); Supro 670 (square); Supro 760 (circle). The results are representative of duplicate experiments

128x119mm (150 x 150 DPI)

Table 1. Relative abundance of protein secondary structures of different SPI samples

SPI samples	Relative abundance of protein secondary structures (%)		
	β-sheet	Helical and coils	β-turn
Lab SPI	56.0 ± 3.6^{ab}	20.6 ± 0.4^{c}	22.1 ± 1.1^{a}
Supro 548	48.8 ± 2.6^{a}	17.2 ± 0.3^{b}	34.0 ± 2.3^{b}
Supro 670	59.8 ± 0.2^{b}	13.8 ± 0.3^{a}	26.5 ± 0.1^{a}
Supro 760	53.4 ± 0.6^{ab}	14.5 ± 0.3^{a}	32.1 ± 0.3^{b}

Different letters in the same column indicate significant differences ($p<0.05$)

Table 2. Soluble protein concentration and insoluble particle mean diameter of different SPI samples

SPI samples	Soluble protein concentration (g 100 g^{-1} SPI)*	Insoluble particle mean diameter (μm)**
Lab SPI	76.3 ± 0.6[a]	3.9 ± 0.1[a]
Supro 548	28.3 ± 2.4[c]	69.0 ± 2.2[c]
Supro 670	55.0 ± 2.0[b]	36.8 ± 2.1[b]
Supro 760	19.0 ± 1.0[d]	71.4 ± 4.3[c]

Different letters in the same column indicate significant differences ($p<0.05$)